universität wien

MASTERARBEIT / MASTER'S THESIS

Titel der Masterarbeit / Title of the Master's Thesis

„Propagation of Magnetostatic Spin Waves in YIG Nano-Structures“

verfasst von / submitted by

Elisabeth Maria Weiß, BSc

angestrebter akademischer Grad / in partial fulfilment of the requirements for the degree of

Master of Science (MSc)

Wien, 2021 / Vienna, 2021

Studienkennzahl lt. Studienblatt / degree programme code as it appears on the student record sheet:	A 066 876
Studienrichtung lt. Studienblatt / degree programme as it appears on the student record sheet:	Master Physik
Betreut von / Supervisor:	Univ.-Prof. Dr. habil. Andrii Chumak
Mitbetreut von / Co-Supervisor:	

Abstract

Modern magnetism aims to investigate waves and magnetism which is combined in the study of spin waves. These waves depict the re-arrangement of the magnetization through a material which is represented by a quasiparticle, the magnon. The fundamental collective excitations in a spin system propagate through the material in such a way that three distinct characteristic behaviors depending on the direction of the externally applied magnetic field can be studied: magnetostatic backward volume spin waves where the magnetic field is applied along the propagation direction; magnetostatic forward volume spin waves where the applied magnetic field is perpendicular to the wavevector of the spin wave; and magnetostatic surface spin waves, or Damon-Eshbach spin waves, where the magnetic field vector is perpendicular but in plane of the spin wave propagation direction. This thesis investigates the behavior of the Damon-Eshbach spin wave.

The excitation frequencies of these spin waves lie in the range of a few GHz, whereas their wavelengths have a magnitude of micrometers. The used material Yttrium-Iron-Garnet (YIG) has uniquely low damping features for spin-wave propagation among other materials used in magneto-electrical appliances, which needs to be studied in nanostructures due to the current miniaturization of technologies before an implementation in devices. This makes the study of nanostructured YIG a relatively recent endeavor. B. Heinz et al. studied spin-wave propagation in backward volume geometry in a nanosized YIG waveguide in his paper “Propagation of Spin-Wave Packets in Individual Nanosized Yttrium Iron Garnet Magnonic Conduits” in Reference [1]. Spin waves generally propagate faster if the waveguide is magnetized perpendicularly. However, due to the highly inhomogeneous internal magnetic field in nanostructured YIG waveguides it is not clear how and if Damon-Eshbach spin waves propagate.

This thesis focuses on the study of the behavior of magnetostatic surface spin waves in a nanostructured YIG waveguide using micromagnetic simulations, existing analytical models for magnetic microstructures and a Brillouin-Light-Scattering (BLS) spectroscopy for experimental measurements of the Damon-Eshbach spin-wave behavior. The results show that Damon-Eshbach spin waves do propagate in nanostructured YIG waveguides and can travel over relatively large distances up to 22 µm [2]. It also compares different dispersion curves for waveguides with different widths as a result of the micromagnetic simulations. The results of the micromagnetic simulations and the existing analytics further show after a comparison of the dispersion curve that the preexisting analytics are not sufficient and an extension is needed to

include nanostructures. The experimental studies of Damon-Eshbach spin waves demonstrate lower intensity of their propagation in nanostructured compared to microstructured YIG, as well as a smaller frequency difference of the photons scattered by magnons compared to the non-interacting laser photons. These theoretical and experimental findings make a significant step towards the realization of nano-scaled magnonic circuits.

Kurzfassung

Spinwellen werden im modernen Magnetismus beschrieben, wo sie eine Vereinigung der Untersuchungsgebiete von Wellen und Magnetismus bilden. Diese Spinwellen stellen eine Neuanordnung der Magnetisierung dar, welche sich durch ein Material ausbreiten. Der kollektive Anregungszustand wird durch ein Quasiteilchen, dem Magnon, beschrieben. Die fundamentalen Anregungen des Spinsystems können in drei unterschiedlich ausgeprägte Spinwellencharakteristiken unterteilt werden, welche durch die Richtung des angelegten magnetischen Feldes unterschieden werden: „magnetostatic backward volume spin waves“ – Spinwellen, die sich ausbreiten können, wenn das magnetische Feld parallel zur Ausbreitungsrichtung angelegt wird; „magnetostatic forward volume spin waves“ – Spinwellen, die sich durch die Anregung eines externen magnetischen Feldes, das senkrecht dazu liegt, ausbreiten; und „magnetostatic surface spin waves“ – oder auch Damon-Eshbach Spinwellen, welche durch ein senkrecht zur, aber in der gleichen Ebene wie die Ausbreitungsrichtung der Spinwellen liegendes Magnetfeld angeregt werden.. Diese Arbeit untersucht die zuletzt genannten Damon-Eshbach Spinwellen.

Anregungsfrequenzen dieser Spinwellen liegen im Gigahertzbereich, welche mit einer Mikrometer-großen Wellenlänge einhergehen. Die einzigartig geringe Spinwellendämpfung in Yttrium-Eisen-Granat (Yttrium-Iron-Garnet, YIG) erlaubt einen breiten Einsatz in magnetoelektrischen Geräten. Nanostrukturen müssen dabei aber vorher untersucht werden, damit diese zukünftig vermehrt in Geräten eingebaut werden können. B. Heinz et al. untersuchten in ihrer wissenschaftlichen Arbeit („Propagation of Spin-Wave Packets in Individual Nanosized Yttrium Iron Garnet Magnonic Conduits”) die Spinwellenpropagation in einer backward volume (Rückwärts-Volumen) Geometrie in einem nanostrukturierten YIG Wellenleiter, welche in Referenz [1] nachgelesen werden kann. Spinwellen breiten sich im Generellen schneller aus, wenn der Wellenleiter senkrecht dazu magnetisiert wird. Aufgrund eines stark inhomogenen inneren Magnetfeldes in YIG-Nanostrukturen ist noch nicht bekannt, ob und wie diese Spinwellen dort propagieren.

Diese Arbeit untersucht das Verhalten von Spinwellen in Damon-Eshbach-Geometrie in einer Nanostrukturierung von YIG mithilfe von numerischen Simulationen und von existierenden analytischen Verfahren, die für Mikrostrukturen entwickelt wurden. Des Weiteren wird eine experimentelle Untersuchung durch ein Brillouin-Light-Scattering (BLS) -Mikroskop durchgeführt. Die Ergebnisse zeigen, dass Damon-Eshbach Spinwellen in YIG-Nanostrukturen existieren und auch über relativ große Distanzen, bis etwas über 22 µm, propagieren [2]. Die

Dispersionskurven der mikromagnetischen Simulation zeigen unterschiedliche Muster aufgrund der untersuchten verschiedenen Breiten der Wellenleiter. Ein Vergleich zu existierenden analytischen Methoden präsentiert, dass die existierenden analytischen Methoden nicht ausreichend sind, um auch Nanostrukturen genügend zu beschreiben. Die experimentellen Resultate zeigen, dass Damon-Eshbach Spinwellen in Nano- und Mikrostrukturen weniger intensiv sind, als auch eine niedrigere Frequenzdifferenz der an den Magnonen gestreuten Photonen und der ursprünglichen Photonen des Lasers zeigen. Die theoretischen und experimentellen Ergebnisse bringen magnonische Schaltungen im Nanometer-Bereich ein Stück näher zur Umsetzung.

Table of Contents

1. Introduction

In the presence of a magnetic field, magnetic moments in a solid align themselves along the field vector, with a certain phase shift compared to the local disturbances of neighboring magnetic moments. These collective excitations propagate through the material in the form of a spin wave, or its corresponding quasi-particle: a magnon. This offers a rich area of research due to their novel properties. Magnonics, as a field of physics, grew into its own scientific domain at the end of the 20th century. The evolution of the magnetization through a material is described by the spin dynamics, or commonly referred to as magnetization dynamics [3]. Three distinct spin wave modes can be described by their characteristic behavior depending on the applied magnetic field: backward volume magnetostatic spin waves, forward volume magnetostatic spin waves and magnetostatic surface spin waves.

The characteristics of spin waves can not only be influenced by the orientation of the externally applied magnetic field, but also by the choice of magnetic material, as well as the orientation of the magnetization therein and the shape of the sample [4,5]. These traits have been studied extensively in the past in existing microstructures of different magnetic materials to show the properties of implemented microwave devices used in magnetoelectrical as well as optical signal processing applications. Among the studied materials, Yttrium-Iron-Garnet (YIG) has an unparalleled low damping factor for spin waves. Combined with a high saturation magnetization, the propagation of spin waves in YIG is facilitated which makes it a great medium for potential future spin-wave technologies.

Investigations of nanostructured materials in magnonics are a recent research direction. Due to the constant downsizing in the industry, microwave devices need to be investigated further at smaller dimensions. Additionally, spin waves offer a loss channel to appliances which work at high frequencies. Different nanostructured materials have been studied, whereas spin waves in nanostructured YIG were only investigated in the backward volume geometry [5]. Further studies show that charge and heat currents can interact with magnons, which offers new information processing concepts. Such computing systems can be based solely on spin waves instead of voltages or electronic charges and may be potentially used in future magnonic devices. These systems offer transfer and processing of information with low losses [6,7]. However, to achieve such a new computing system spin-wave transport needs to be realized in two-dimensional structures and demonstrators need to be scaled down to micro- or nanostructures. Microstructures which have been studied to a large extent are sufficient for

today's technology, but future applications will need to be smaller. As the used devices are ever downscaled, these smaller appliances need to be researched to understand the behavior of the material at smaller scales first.

This thesis brings light upon the propagation dynamics of Damon-Eshbach spin waves (also known as Magnetostatic Surface Spin Waves (MSSW)) in a nanostructured YIG waveguide, where the external magnetic field is applied in such a way that the magnetic field vector is perpendicular to, but in plane of the spin-wave propagation direction. Due to the small width of the waveguide, the internal magnetic field of the YIG waveguide is strongly non-uniform which influences the spin-wave propagation strongly. Therefore, this thesis is focused on the investigation of the dispersion curve as well as other characteristics of the behavior of spin waves when the externally applied magnetic field vector is in the same plane of, but perpendicular to their propagation direction with the help of micromagnetic simulations as well as experimental studies using a micro-focused Brillouin Light Scattering (µBLS) microscope. Using micromagnetic simulations in the MuMax³ micromagnetic simulation program as well as preexisting analytics for microstructures, the spin-wave dispersion curve in a nanostructured YIG is examined and compared to demonstrate a different behavior of micro- and nanostructures at low wavenumbers. An experimental study of Damon-Eshbach spin waves in a nanostructured YIG waveguide is done using a µBLS microscope setup, as well as a measurement on microstructured YIG to show a difference in the behavior of magnetostatic surface spin waves depending on the size of the waveguide. The spin waves will be excited through a micro-strip antenna with a signal in GHz frequency range. The photons of the µBLS-laser will be scattered inelastically by the excited magnons in a nanoscaled YIG waveguide which are then examined with the help of a Tandem-Fabry-Pérot interferometer to get the frequency difference of the unaffected and the scattered photons. The BLS-spectrum of the magnetostatic surface spin waves in the nanostructured waveguide is expected to look similar to the already investigated microstructures but differ in intensity of the counts.

In this thesis, the chapters are structured as follows: After the introductory Chapter 1, Chapter 2 offers fundamental knowledge to understand the basics of magnetism and magnetic moments. The used magnetic material YIG for the waveguide in which the spin-wave propagation is investigated is introduced followed by a brief discussion of different factors which can influence the internal magnetic field of a waveguide. As a guidance to the main topic of this thesis – spin waves – the magnetization dynamics as well as the magnetic equation of motion, the Landau-Lifshitz equation as well as a more realistic version the Landau-Lifshitz-Gilbert equation, are discussed. This leads to an introduction of spin waves and their origin as well as

their behavior. The three distinct characteristic modes depending on the external applied magnetic field with a special focus on the topic of this thesis, magnetostatic surface spin waves or Damon-Eshbach spin waves, are discussed with regards to their dispersion behavior in a magnetic material.

In the following Chapter 3, the used simulation technique and the experimental investigation tool are described. Numerical simulation methods are divided into the Finite Element Method and the Finite Difference Method. The latter is used in this thesis for a numerical simulation of Damon-Eshbach spin waves in an idealistic nanostructured YIG waveguide as well as a depiction of the highly non-uniform magnetic field therein. The experimental investigation is based on the scattering of photons by magnons, which is called the Brillouin light scattering. A description thereof leads to the introduction of the micro-focused Brillouin-light scattering microscope (μBLS) which was used in this thesis to investigate Damon-Eshbach spin waves in a nanostructured YIG waveguide.

The theoretical investigations of the internal magnetic field and the spin-wave dispersion of YIG nanostructures are presented in Chapter 4. Using the micromagnetic simulation program MuMax³, spin waves in a Damon-Eshbach geometry are simulated in a nanostructured YIG waveguide. The propagation dynamics of such spin waves are examined and displayed in a dispersion curve. A comparison thereof is given for YIG waveguides with higher thicknesses. Using preexisting analytics, the dispersion curve is plotted and compared to the obtained results of the numerical simulation.

Chapter 5 states the obtained results using the μBLS microscope. A measurement on a 1 μm wide waveguide was performed to then show the differences to the spectrum of a nanostructured waveguide. Spin waves in a nanostructured YIG waveguide are studied to show their propagation behavior in MSSW geometry. Different spectra were obtained using continuous excitation and pulsed excitation of the spin waves in the nanostructure depending on the frequency of the applied microwave signal. Moreover, with the results of a decay measurement with continuous excitation the decay length of a magnetostatic surface spin wave concludes the experimental part of this thesis.

The last chapter, Chapter 6, gives a short summary of the results in this thesis and an outlook for future research.

2. Fundamental theory

This thesis focuses on the propagation dynamics of spin waves in Damon-Eshbach geometry in a nano-scaled YIG waveguide. Therefore, this chapter shall provide an introduction to the basics in micromagnetism and magnonics, which are needed for an understanding of the spin dynamics. A basic construction of magnetism, starting at the description of magnetic moments, which are inherent to every material and the interactions in a system of coupled magnetic moments, shall be clarified. Different influences on the experienced magnetic field of a sample, such as the demagnetizing field and anisotropy of the sample structure, will be introduced. The second subchapter establishes the equation of motion, the Landau-Lifshitz equation, and a realistic version thereof which includes the Gilbert damping term. Further, the equation will be altered to accommodate for an applied dynamic magnetic field using the Polder tensor. The chapter will end with the description of spin waves alongside their quasi-particle as the excitation of the electron's spin structure in the whole lattice, the magnon. Different properties of the spin waves are discussed such as the ferromagnetic resonance, the behavior of spin waves in a thin magnetic field and their dispersion relation, and distinct magnetostatic volume and surface spin waves. At last, the spin-wave excitation and propagation loss will be examined.

2.1. Basics of magnetism

Magnetism is included in everyday life. Magnets are needed in generators to transform mechanical energy into electricity, they remove small metal bits from grains and other food, and they even help discern illnesses in the soft tissues of the human body. However, the discussed magnetic phenomena in this thesis all happen at a very small scale. As a magnetic dynamic field is applied to a magnetic material to excite spin waves in a YIG material in this thesis, this chapter brings knowledge about the used material as well as the fundamentals of magnetism. Later on, the origins as well as the interactions between magnetic moments will be discussed.

This chapter introduces different terms and their definitions to provide a solid basis of knowledge in magnetism, as well as different interactions in magnetic systems. There are two fundamental sources which allow magnetism to form: electric current and magnetic moments of elementary particles.

2.1.1. Classical magnetism

The first discovery of magnetism was many thousand years ago. Probably before recorded history began, many diverse stories came from different origins around the world. What connects them all is the attraction of lodestone to iron, a simple magnetic phenomenon. Many years later, it was found that natural magnets always align themselves in the same direction, if properly stored with little friction. William Gilbert was the first to understand and show that even the earth itself was a giant magnet [8].

Later, Hans Christian Ørsted discovered that a compass needle was deflected by the presence of a wire with current running through, and thereby confirmed a direct correlation of electricity and magnetism. A non-moving charge only generates an electric field **E**, whereas a moving charge also produces a magnetic field **H** [9,10].

The generated magnetic field of the moving charges can be calculated by using the electric current density **j** and the electric displacement field **D**.

$$\nabla \times \mathbf{H} = \mathbf{j} + \frac{\partial \mathbf{D}}{\partial \mathrm{t}}. \tag{1}$$

In the case of constant **D**, the equation describing the magnetic field **H**(**r**) for arbitrary distance **r** generated by a current described by the current density in a volume V' can be found. This equation, called the Biot-Savart-law, is essential in magnetostatics.

$$\mathbf{H}(\mathbf{r}) = \frac{1}{4\pi}\int_{V'} \nabla \times \frac{\mathbf{j}(\mathbf{r}')}{|\mathbf{r}-\mathbf{r}'|}\,\mathrm{d}\mathbf{r}'. \tag{2}$$

2.1.2. Magnetic moment

Every magnet or object that generates a magnetic field has a magnetic moment **m**. To calculate this moment in a magnet, a magnetic field is applied to it. The external magnetic field **H** forces the magnetic moment **m** to align itself to the field vector, which generates a torque **τ** in relation to the applied field.

$$\boldsymbol{\tau} = \mathbf{m} \times \mathbf{H}. \tag{3}$$

The interaction of a solid with a magnetic field is due to interaction of the field with inherent or induced magnetic moments in the object. The force **F** acting on a magnetic moment is given by

$$\mathbf{F} = \mathbf{m}\nabla \cdot \mathbf{B}. \tag{4}$$

The classical Bohr model of the atom is essential to finding the first understanding of how magnetism works on a smaller scale. A current I passes through a closed, circularly looped circuit with radius R and a resulting area of $\mathbf{A} = \mathrm{A}\hat{\mathbf{n}} = \pi \mathrm{R}^2 \hat{\mathbf{n}}$. This system generates a magnetic field and therefore possesses a magnetic moment [9,11,12]

$$\mathbf{m} = \mathrm{I} \cdot \mathbf{A}. \tag{5}$$

To get the magnetic moment of an atom, a comparison is drawn to such a wire with current running through. For the atomic magnetic moment, replacement of the wire with the orbiting electron and the cross section of the wire with the area enclosed by the orbiting electron gives for the circular current

$$\mathrm{I} = -\mathrm{e}\frac{\omega}{2\pi}. \tag{6}$$

The electrons, which carry an electric charge of $-e$, are orbiting the nucleus at a distance R with an angular velocity ω. This circular movement is part of the origin of the atomic magnetic moment **m**.

$$\mathbf{m} = -\frac{\mu_0 \mathrm{e}\omega \mathrm{R}^2}{2}\hat{\mathbf{n}}. \tag{7}$$

Using the angular momentum $\mathbf{L} = \mathrm{m_e}\omega \mathrm{R}^2 \hat{\mathbf{n}}$ and the mass of the electron m_e leads to another version to calculate the magnetic moment of an atom:

$$\mathbf{m} = -\frac{\mu_0 \mathrm{e}}{2\mathrm{m_e}}\mathbf{L}. \tag{8}$$

The atomic Bohr model uses the quantized angular momentum. Walther Ritz and Pierre Weiss had the idea of elementary magnets, which needed the magneton to include Planck's constant. Bohr's magneton μ_B is a physical constant and describes the magnetic moment of a singular

electron due to its orbital or spin angular momentum. It is the smallest, no more separable magnetic dipole moment of an electron.

To relate the observed magnetic moment of a particle (here: electron) to its angular momentum quantum number and Bohr's magneton, keeping the quantity dimensionless, a g-value is needed for an electron with both spin and orbital angular momentum. For orbital angular motion, the g-factor depends on the relative distribution of mass and charge, for example yielding $1/2$ for a cyclotron motion in a magnetic field. In the case of a mechanical angular momentum, this is the Landé g-factor $g_l = 1$.

After including $\mu_B = {e\hbar}/{2m_e} = 9.2740 \cdot 10^{-24}\ {J}/{T}$ and g_l for the electron, formula (8) for the magnetic moment due to the orbital motion can be rewritten as

$$\boldsymbol{\mu_l} = -g_l \mu_B \frac{\mathbf{L}}{\hbar}, \tag{9}$$

where the magnitude of angular momentum of an electron for values $l = 0, \ldots, n-1$ of the orbital angular momentum quantum number *l* is given by

$$|\mathbf{L}|^2 = l\,(l+1)\hbar^2. \tag{10}$$

Analogous to the orbital angular momentum, the same can be done with the spin, which exists as another part of the angular momentum for electrons and other particles. The spin quantum number can only have two values, $s = \pm\frac{1}{2}$, as seen in the experiments of Otto Stern and Walther Gerlach [13]. In 1922, they demonstrated the spatial separation of silver atoms with vanishing angular momentum in a highly inhomogeneous magnetic field. Due to the non-zero magnetic moment, the atoms were deflected and spatially separated in a non-continuous distribution, giving those discrete points values of $+{1}/{2}$ and $-{1}/{2}$. This experiment determined the quantization of the spatial orientation of angular momentum.

The magnitude of the spin angular momentum **s**, given by $|\mathbf{s}|^2 = s\,(s+1)\hbar^2$, is used to describe the spin magnetic moment $\boldsymbol{\mu_s}$ via spin angular momentum.

$$\boldsymbol{\mu_s} = -g_s \mu_B \frac{\mathbf{s}}{\hbar}. \tag{11}$$

This equation uses the anomalous Landé g-factor for spin angular momentum of an electron $g_s = 2.003193$.

The total angular momentum **J** of a particle equals $\mathbf{J} = \mathbf{L} + \mathbf{S}$. Using the ratio of the magnetic moment to the angular momentum of a particle, called the gyromagnetic ratio $\gamma = g\,{}^{\mu_B}/_{\hbar}$, another more general version to compute the total magnetic moment can be introduced, where a magneton of the carrier particle for the total angular momentum with mass m_j is used.

$$\mathbf{m} = \boldsymbol{\mu}_\mathbf{l} + \boldsymbol{\mu}_\mathbf{s} = g_j \frac{q\,\hbar}{2\,m_j} \frac{\mathbf{J}}{\hbar} = \gamma\,\mathbf{J}. \tag{12}$$

Magnetic moments and externally applied field

Applying an external static magnetic field leads to a coupling of the electron in a molecule with said field. This Zeeman coupling can be described with a spin Hamiltonian, using the value of angular momentum S_z in the direction of the magnetic field, the magnetic moment of an electron in the molecule μ_e and the strength of the applied laboratory field H_0.

$$\mathcal{H}_Z = g\,\mu_e\,H_0 \cdot S_{z.} \tag{13}$$

2.1.3. Interaction of magnetic moments

To describe the behavior of magnetic moments in general, it is of importance to acknowledge the interactions among magnetic moments. The direct interaction between two magnetic dipoles at a far-range is called dipole-dipole interaction, or dipolar coupling. To classify the coupling of an electron spin with other magnetic moments, quantum mechanics uses a spin Hamiltonian. This operator contains all magnetic couplings which influence the energy and precessional frequency of the electron spin.

Each magnetic moment represents a magnetic dipole. This means that each magnetic moment is origin to a magnetic field which affects another magnetic moment. In a short-range distance, the affecting interaction is the exchange interaction. Described by quantum mechanics, this interaction only occurs between identical particles [14,15].

Exchange interaction

In quantum mechanics, a singular electron can be described by a wave function $\Phi(\mathbf{r}, \mathrm{s})$ as a combination of a space wave function $\Psi(\boldsymbol{r})$ and a spin wave function $\chi(s_z)$.

$$\Phi(\mathbf{r}, \mathrm{s}) = \Psi(\mathbf{r})\chi(\mathrm{s_z}). \tag{14}$$

In a system with a spin-independent Hamilton-operator the wave function of two electrons is given by a combination of the singular electron wave functions. The orientation of the spin can be parallel for $s_{z1} = s_{z2} = \pm\frac{1}{2}$ or antiparallel for $s_{z1} = \pm\frac{1}{2}$ and $s_{z2} = \mp\frac{1}{2}$.

$$\Phi(\mathbf{r_1}, \mathbf{s}_1;\ \mathbf{r_2}, \mathbf{s}_2) = \Psi(\mathbf{r_1}, \mathbf{r_1})\chi(\mathrm{s_{z1}}, \mathrm{s_{z2}}). \tag{15}$$

The effect of the exchange interaction is due to two particles being affected by exchange symmetry. This forces electrons to either change their sign or other particles to leave it unchanged. Due to two electrons being indistinguishable from each other and their fermionic nature the sign of the wave function is switched after a swapping of both electrons due to the Pauli exclusion principle [5]. A simple implementation of this behavior can be made using either a symmetric spin wave function and a symmetric space wave function, or vice versa. This gives for the total wave function in a system of two electrons:

$$\Phi(\mathbf{r_1}, \mathbf{s}_1;\ \mathbf{r_2}, \mathbf{s}_2) = -\Phi(\mathbf{r_2}, \mathbf{s}_2;\ \mathbf{r_1}, \mathbf{s}_1). \tag{16}$$

Exchange of electrons results in a splitting of singlet and triplet states due to non-classical effects.

$$\mathcal{H}_{\mathrm{ex}} = -2\mathrm{J}\, S_1 \cdot S_2. \tag{17}$$

The Hamilton operator $\mathcal{H}_{ex}$ of the exchange interaction is given by the spin operators of the two electrons and the exchange integral J.

The exchange integral is given by half of the difference in energy of the singlet and the triplet state and can be approximated as an exponential function.

This interaction is a Coulombic effect and not a magnetic one, but it still influences magnetic coupling: 1) The singlet and triplet states are different in energy. If the exchange integral J is positive, the triplet state has the smallest energy, as it is in a ferromagnet. If $J < 0$, the singlet

state has the smallest energy, which is the case in an antiferromagnetic material. 2) The two electrons are electrostatically coupled together.

The difference in energy ΔE of these two states is given by the singlet state $\Phi_S(\boldsymbol{r}_1, \boldsymbol{r}_2)$ and the triplet state $\Phi_T(\boldsymbol{r}_1, \boldsymbol{r}_2)$ of the total wave function. This difference exists due to distinct symmetries of the singlet and triplet state space wave function and a subsequent different probability density.

$$\Delta \mathrm{E} \;=\; \mathrm{E_S} \;-\mathrm{E_T} \;=\; \int \Phi_{\mathrm{S}}^{*}\; \mathrm{H}\; \Phi_{\mathrm{S}}\; \mathrm{d}\mathbf{r}_1 \mathrm{d}\mathbf{r}_2 \;-\; \int \Phi_{\mathrm{T}}^{*}\; \mathrm{H}\; \Phi_{\mathrm{T}}\; \mathrm{d}\mathbf{r}_1 \mathrm{d}\mathbf{r}_2 \;=\; 2\,\mathrm{J}. \tag{18}$$

This coupling is significantly stronger than the dipole-dipole interaction leading to a general alignment of the magnetic moments in a ferromagnet at room temperature.

Dipole-dipole interaction

This interaction considers all forms of interaction between two dipoles: electric dipoles (two electric dipoles or an electric and a nuclear dipole) or magnetic dipoles, such as the electron spin, the nuclear spin, a magnetic field or an orbital magnetic dipole. The energy of the dipolar interaction depends on the orientation of the magnetic moments to each other. Each magnetic moment $\mathbf{m}$ generates a magnetic field $\mathbf{H}_{\mathrm{Dip}}(\mathbf{r})$, which is given by the following formula at a distance $\mathbf{r}$ between two dipoles:

$$\mathbf{H}_{\mathrm{Dip}}(\mathbf{r}) = \left(\frac{3\,(\mathbf{m}\cdot\mathbf{r})\mathbf{r}}{\mathbf{r}^5} \;-\; \frac{\mathbf{m}}{\mathbf{r}^3}\right). \tag{19}$$

The strength of the interaction of many dipoles can be drawn from the observation of the energy of two magnetic moments $\mathbf{m}_1$ and $\mathbf{m}_2$ at respective locations $\mathbf{r}_1$ and $\mathbf{r}_2$ (with a distance $\mathbf{r} \;=\; \mathbf{r_1} - \mathbf{r_2}$ between the magnetic moments) , where μ_r is the magnetic permeability of the material (for vacuum $\mu_\mathrm{r} = 1$) and $\mu_0 = 4\pi \cdot 10^{-7}\ \mathrm{N/A^2}$ is the magnetic constant. With the magnetic field at the magnetic dipole $\mathbf{m}_2$ caused by the dipole $\mathbf{m}_1$, the energy of the dipole - dipole interaction is given by Formula 20. This dipolar interaction between two magnetic dipoles is depending on 1) the magnitudes of the interacting dipoles, 2) the distance between them, 3) the orientation relative to each other and 4) the intersection of resonances which conserve angular momentum and energy [11].

$$E_{Dip} = -\mu_r\mu_0 \mathbf{m}_2 \cdot \mathbf{H}_{\mathbf{m}_1}(\mathbf{r}_2 - \mathbf{r}_1) = \mu_r\mu_0 \left(\frac{\mathbf{m}_1 \cdot \mathbf{m}_2}{\mathbf{r}^3} - 3\frac{(\mathbf{m}_1 \cdot \mathbf{r})(\mathbf{m}_2 \cdot \mathbf{r})}{\mathbf{r}^5} \right). \quad (20)$$

Although this interaction is weak compared to the exchange interaction and the field strength is falling off with $1/\mathbf{r}^3$, it has a significant long-range impact for the magnetization.

2.1.4. Magnetic properties of materials

Spin waves can only exist and propagate in magnetic materials. As there are different magnetic properties for different materials, an overview shall be provided in this section of the thesis of the used ferrimagnetic material, Yttrium-Iron-Garnet or short YIG, as well as the different magnetic behaviors of other materials for completeness.

In magnetic materials, the atomic magnetic moments can be in magnetic disorder, which means that magnetic moments are oriented in random directions, or in magnetic order. In this following part, these different arrangements of magnetic moments shall be discussed. The value of the magnetic susceptibility χ gives an indication of how much a magnetic material can be magnetized by an externally applied magnetic field. It can be calculated as the ratio of the magnetization *M*, the sum of all magnetic moments in a specific volume, of a material to the applied field intensity *H* [8,16].

$$\chi = \frac{\mathbf{M}}{\mathbf{H}}. \quad (21)$$

Diamagnetism

Diamagnetism appears in all magnetic materials, but when it is the only phenomenon contributing to the magnetism of the material, this material is labeled as a diamagnetic. The magnetic susceptibility of such a material is relatively small, usually at a value of $\chi \sim -10^{-5}$. Magnetization is induced opposite to the magnetic field due to acceleration of the orbital electrons by the infiltration of the external magnetic field into the electron's orbit. In accordance with Lenz's law, the induced magnetic flux is always opposite to the change in magnetic field.

Superconductors have no electrical resistivity starting at a specific low temperature, termed the critical temperature T_c. This means in theory that a perfect superconductor transfers electrical energy between two points without losing energy by a means of heat. Another important

characteristic of a perfect superconductor is perfect diamagnetism with a magnetic susceptibility $\chi = -1$.

Paramagnetism

A phenomenon observed in materials which are weakly attracted by an externally applied magnetic field is called paramagnetism. It is found in materials with magnetic atoms or widely separated ions such that they show no signs of interaction among them. They do not retain any magnetization after a loss of the external magnetic field due to randomization of the spin orientations by thermal motion. The magnetic susceptibility of such a material is relatively low, but positive: $\chi \sim 10^{-5} - 10^{-2}$.

Ferromagnetism

Strong magnetic behavior, such as a strong attraction to magnets or forming a permanent magnet, is characterized by ferromagnetism. The source of this strong magnetism is a spontaneous magnetization due to an alignment of all molecular magnetic dipoles in the same direction, even in the absence of an external magnetic field, leading to the creation of magnets. The magnetic susceptibility has a large positive value, sometimes exceeding 1000. A first proposal to clarify this behavior was made by Pierre Weiss in 1907. He stated that in every ferromagnetic material exists an effective, molecular field which aligns adjacent spins parallel to one another. Non-interacting spins can be magnetized by application of a high magnetic field. This phenomenon only exists in a few elements, like nickel, cobalt, iron and rare earth elements, and their alloys depending on the crystalline structure.

Ferrimagnetism

Similar to ferromagnetism, this is a strong magnetism. In 1948, Louis Néel showed that there are two different alignment possibilities inside a material for it to show spontaneous magnetization. Ferrimagnetism has many parallel aligned magnetic moments, but some point in the opposite direction which form different sublattices. Those A- and B-sublattices are often inhabited by different magnetic atoms or different numbers of atoms.

Antiferromagnetism

Neighboring spins spontaneously align themselves in such a way that their magnetic moments cancel each other. An antiferromagnetic material therefore produces no spontaneous magnetization and exhibits almost no external magnetism. The magnetic susceptibility can lie

in the same range as the one for paramagnetism, the only difference being the presence of an ordered spin structure.

When an external magnetic field is applied, the spins keep their antiparallel arrangement, making the susceptibility smaller than that of a paramagnet. If the temperature is increased, the spin alignment structure is destroyed which leads to an increase of the magnetic susceptibility in contrast to the paramagnetic material.

YIG – a non-metallic magnetic material used in magnonics

Monocrystalline Yttrium iron garnet (YIG) $Y_3Fe_5O_{12}$ is a low-damping magnetic material with a very narrow ferromagnetic resonance width line smaller than $0.05\,\mathrm{mT}$, allowing in some instances spin-wave propagation over few centimeters. This material is used often in microwave devices due to the low-damping and strongly pronounced non-linear dynamic effects. It also has a high magneto-optical efficiency [17].

High-quality thin YIG-films can be produced by growing high-temperature liquid-phase epitaxy on a substrate of Gallium Gadolinium Garnet (GGG) which has a similar lattice constant as YIG (with a lattice mismatch of $\Delta a{\sim}0.7\mathrm{pm}$). This leads to nearly defect-free unstressed films, which can only be improved by slightly doping the YIG with Lanthanum or Gallium. The typical saturation magnetization of YIG is $4\pi M_0 = 175\,\mathrm{mT}$ and a typical exchange constant lies in the range of $\alpha = 3.5 - 4.5 \cdot 10^{-12}\ {}^{\mathrm{J}}/_{\mathrm{m}}$.

2.1.5. Anisotropy

Magnetic anisotropy describes a dependence of the magnetic state on the direction of the magnetization. Even without an externally applied magnetic field, a magnetic solid has a distinct favored orientation of its magnetization which minimizes the energy of the system. Due to spin-orbit coupling or the dipolar interaction different axes are preferred for the magnetization along the geometric structures of the crystal or the geometric structure of the magnet, respectively. Moreover, surfaces, an elastic deformation (magnetoelastic anisotropy) of the sample or an interaction of antiferromagnetic and ferromagnetic materials can affect the energy of the system. If an applied magnetic field does not correspond to the preferential direction of the magnetization, the field must exert work on the system to shift the magnetization. The two predominant factors for anisotropy in a material, magnetocrystalline anisotropy and shape anisotropy shall be discussed in more detail in the following part [10,16,18].

The key issue of this thesis is to bring light on the propagation dynamics of the spin waves in a nanostructured YIG waveguide. Shape anisotropy plays an important role for the properties of spin waves therein. The used YIG waveguide has an extremely small magnetocrystalline anisotropy. Therefore, the following thesis does not focus on these anisotropies, but merely tries to show the propagation dynamics of spin waves in a waveguide below 100 nm in a perpendicularly applied magnetic field.

Magnetocrystalline anisotropy

This anisotropy is an intrinsic property of the material depending on its geometry. The atomic structure also introduces a favorable direction of the magnetization, which is mediated by the spin-orbit coupling (SOC).

$$\mathbf{H}_{\mathrm{soc}} = \xi(\mathbf{r})\mathbf{S} \cdot \mathbf{L}. \tag{22}$$

The magnetic field of the magnetocrystalline anisotropy H_{soc} is given by the coupling constant of the spin-orbit coupling ξ depending on the location in the material, the spin S and the orbital angular momentum L.

Shape anisotropy

The shape anisotropy strongly depends on the demagnetizing field and the coupled stray fields, which reduce the magnetic field inside a sample. If a ferromagnetic solid is asymmetrical, the demagnetization differs with the direction of the magnetization which varies the magnetizing force inside the material throughout the body. Homogeneous bodies with an ellipsoidal shape, e.g. a sphere or in approximation a thin film, are mostly used in precise investigation of magnetic materials due to a uniform demagnetizing field throughout the body [19]. Then, the demagnetizing field $\mathbf{H}_{\mathrm{dem}}$ for simple geometric shapes of the solid can be given depending on the magnetization **M**.

$$\mathbf{H}_{\mathrm{dem}} = -N \cdot \mathbf{M}. \tag{23}$$

The demagnetization tensor N, with tr(N) = 1, combines the different acting demagnetizing fields along the different axes. For an infinitely expansive thin film the diagonal of the tensor is given by the properties given in Formula 24, whereas the calculation of each component of the demagnetization tensor for a different shape of the sample gets more challenging.

$$N_{xx} = N_{yy} = 0 \text{ and } N_{zz} = 1. \quad (24)$$

Without an external magnetic field, the magnetization always lies in-plane, where no stray fields are created. An external magnetic field totally compensating the demagnetizing field is needed for a full magnetization of the film parallel to the surface normal. From this system, one can extract the value of the saturation magnetization $H_{dem} = -M_s$.

The internal magnetic field of a material is only homogeneous for a precessional ellipsoid or an infinitely expansive body, where the dipolar fields of each magnetic moment is compensated throughout the material. Generally, a finite or an inhomogeneous magnetic sample has magnetic moments which are not compensated. These magnetic parts are summarized in an effective magnetic field which is called demagnetizing field inside the sample $\mathbf{H}_{dem}$, and outside stray field $\mathbf{H}_s$. They can be described via the magnetostatic Maxwell equations for the case of no current [5,16,20]:

$$\nabla \times \mathbf{H}_{dem} = 0, \quad (25)$$

$$\nabla \cdot \mathbf{B} = \mu_0 \nabla \cdot (\mathbf{H}_{dem} + \mathbf{M}) = 0. \quad (26)$$

A potential can be introduced due to rotational freedom of the demagnetization $\mathbf{H}_{dem} = -\nabla \cdot \Phi$ to describe the source of the demagnetizing field, the magnetic charge density λ_m, in the magnetostatic Poisson equation.

$$\Delta\Phi = -\lambda_m. \quad (27)$$

The magnetic charge density can be divided into a part considering the charge density in the volume and a magnetic charge density term of the surface. The volume term describes the inhomogeneous magnetization in the sample, whereas the surface term is non-zero when the magnetization is not exactly aligned parallel to the surface.

The demagnetizing field is always antiparallel to the magnetization, decreasing the effects of the externally applied magnetic field.

2.1.6. Effective magnetic field

The internal magnetic field is a composite of the external magnetic field (consisting of a static $\mathbf{H}_0$ and a time-dependent varying component $\mathbf{h}(t)$) [21], the demagnetizing field $\mathbf{H}_{dem}$,

the magnetic field due to the exchange interaction $\mathbf{H}_{\mathrm{exc}}$ and different magnetic fields accounting for different anisotropies inside the material $\mathbf{H}_{\mathrm{ani}}$.

$$\mathbf{H}_{\mathrm{eff}} = \mathbf{H}_0 + \mathbf{h}(\mathrm{t}) + \mathbf{H}_{\mathrm{dem}} + \mathbf{H}_{\mathrm{exc}} + \mathbf{H}_{\mathrm{ani}}. \tag{28}$$

2.2. Magnetization dynamics

Magnetization dynamics describe the evolution of the magnetization of a material. This chapter introduces the general behavior of the magnetization in an effective magnetic field described by the equation of motion in magnonics, the Landau-Lifshitz equation. Moreover, the damping of a precessional magnetization shall be clarified.

2.2.1. Larmor precession

As stated in (2.1.2) a magnetic moment in an external magnetic field experiences a torque proportional to the misalignment which wants to adjust the moment and field vectors into the same direction, which is explained graphically in Figure 1. An electron realizes this torque as a precession around the direction of the external magnetic field due to the magnetic moment of an electron orbiting around the nucleus being proportional to its angular momentum **J** and effective internal electric current.

$$\boldsymbol{\tau} = \gamma\, \mathbf{J} \times \mathbf{H}. \tag{29}$$

The angular momentum precesses around the external magnetic field with an angular frequency, called the Larmor frequency.

2.2.2. Landau-Lifshitz equation

The angular momentum can be rewritten in terms of the magnetic moment and the gyromagnetic ratio $\mathbf{J} = -\frac{1}{|\gamma|}\,\mathbf{m}$. The torque onto a magnetic moment in an external magnetic field equates to the time derivative of the angular momentum [3,22,23], which gives

$$-\frac{1}{|\gamma|}\frac{\mathrm{d}\mathbf{m}}{\mathrm{dt}} = \mathbf{m} \times \mu_0 \mathbf{H}. \tag{30}$$

Coming from a singular magnetic moment to a whole material with a multitude of magnetic moments, the magnetization **M** is defined by a uniform distribution of spin in the material.

$$\mathbf{M} = -\frac{g\mu_B}{\hbar}\mathbf{S}. \tag{31}$$

Along with an effective magnetic field which considers the interaction among the different magnetic moments, the magnetization leads to another version, the so-called Landau-Lifshitz equation:

$$\frac{d\mathbf{M}}{dt} = -|\gamma|\mathbf{M} \times \mu_0\mathbf{H}_{eff}. \tag{32}$$

This formula describes the precession of the magnetization around the effective magnetic field axis, where the magnetization and the field axis are orthogonal to the torque. If the Landau-Lifshitz-equation is multiplied by the magnetization or a constant in a time effective magnetic field, an important feature of the equation can be found:

$$\frac{d\mathbf{M}}{dt} \cdot \mathbf{M} = \frac{d|\mathbf{M}^2|}{dt} = -\gamma\mathbf{M} \times \mathbf{H}_{eff} \cdot \mathbf{M} = 0, \tag{33}$$

$$\frac{d}{dt}(\mathbf{M}(t) \cdot \mathbf{H}_{eff}) = 0. \tag{34}$$

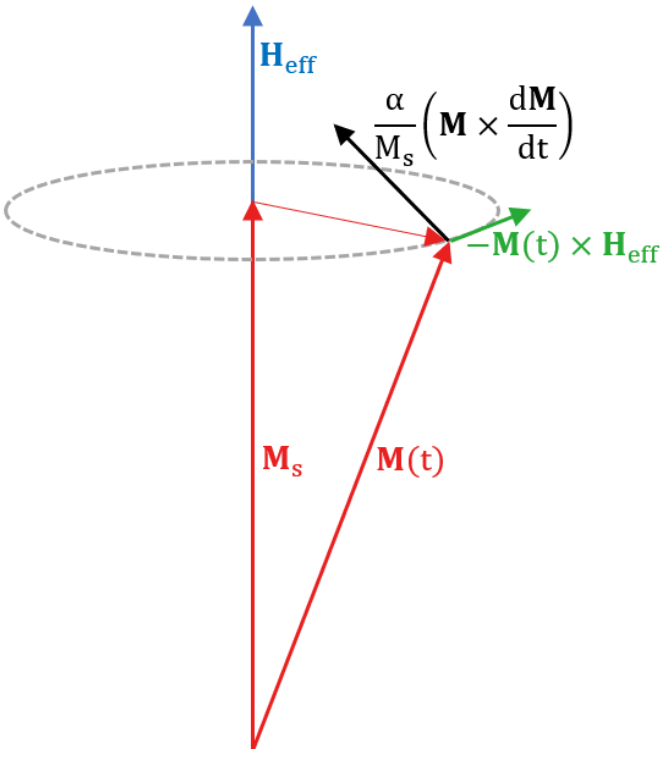

Figure 1: **Schematic depiction of the magnetization dynamics.**
The magnetization *M* feels a torque when an external magnetic field is applied, which results in a precession of the magnetization around the field vector of the effective magnetic field. Damping leads to a relaxation of the system in direction of the magnetic field. Modeled after [10].

These two equations state that the value of the magnetization as well as the angle between the magnetization and the effective magnetic field are constant in time. Furthermore, the direction of the precession is constant, and counterclockwise for an electron if the magnetic field vector is coming out of the plane.

2.2.3. Damping factors of the Landau-Lifshitz equation

According to the Landau-Lifshitz equation which considers no damping of the system, if a magnetization is misaligned, it will precess forever around the effective magnetic field vector. The magnetization needs to be parallel to the direction of the external magnetic field to be in its lowest energy state [3,12].

In reality, some dissipation mechanisms exist which relax the precession towards the direction of the applied magnetic field. Although Landau and Lifshitz included damping in another version of their equation, Thomas Gilbert added a term which depends on the time derivative of the magnetization in 1955. This involves a loss of energy which results in a torque $\mathbf{D}_\alpha$ pulling the magnetization in the direction of the effective magnetic field vector.

$$\mathbf{D}_\alpha = -\frac{\alpha}{M_s}\mathbf{M} \times \frac{d\mathbf{M}}{dt}. \tag{35}$$

Using the saturation magnetization M_s and a newly introduced parameter α, called the Gilbert damping parameter, this viscous damping leads to the Landau-Lifshitz-Gilbert damping in Formula 36.

$$\frac{d\mathbf{M}}{dt} = -|\gamma|\mathbf{M} \times \mu_0\mathbf{H}_{\text{eff}} - \frac{\alpha}{M_s}\mathbf{M} \times \frac{d\mathbf{M}}{dt}. \tag{36}$$

This equation describes a system in which the magnetization is spiraling back to the direction of the effective magnetic field.

Similar to the Landau-Lifshitz-Gilbert equation, there exist different forms to describe the damping of the system, e.g. a version of Lev Landau and Evgeny Lifshitz themselves, as well as a version of Felix Bloch and Nicolaas Bloembergen.

2.2.4. Polder tensor

The Landau-Lifshitz equation describes the dynamics of the magnetization, as seen in the chapters before. After noticing that a ferrimagnetic material becomes anisotropic in the presence of an external magnetic field, Dirk Polder introduced a tensor to describe the magnetic permeability. In this thesis, a varying external magnetic field is used to excite the spin waves in the material.

The effective magnetic field $\mathbf{H}_{\text{eff}}$, as well as the magnetization are now compositions of a time-dependent component and a static term as shown in Formula 37 and Formula 38.

$$\mathbf{H}_{\text{eff}}(\text{t}) = \mathbf{H}_0 + \mathbf{h}(\text{t}). \tag{37}$$

$$\mathbf{M}(\text{t}) = \mathbf{M}_0 + \mathbf{m}(\text{t}). \tag{38}$$

Introducing the varying magnetic field and magnetization [5] into the Landau-Lifshitz equation without using the damping term, for simplicity reasons, gives the following formula:

$$\frac{\text{d}\mathbf{m}(\text{t})}{\text{dt}} = -|\gamma|\mu_0\big(\mathbf{M}_0 \times \mathbf{H}_0 + \mathbf{M}_0 \times \mathbf{h}(\text{t}) + \mathbf{m}(\text{t}) \times \mathbf{H}_0 + \mathbf{m}(\text{t}) \times \mathbf{h}(\text{t})\big). \tag{39}$$

The material shall be homogeneously magnetized along the direction parallel to the applied magnetic field, $\mathbf{H}_0 \parallel \mathbf{M}_0$, rendering the cross-product term between those two zero. Furthermore, the time-dependent terms ($|\mathbf{M}_0| \gg |\mathbf{m}(\text{t})|$ and $|\mathbf{H}_0| \gg |\mathbf{h}(\text{t})|$) shall be small compared to the non-varying terms which makes the cross-product term of the time-dependent magnetization and magnetic field neglectable.

Using the following ansatz for the varying terms

$$\mathbf{m}(\text{t}) = \mathbf{m}_0 \exp(-\text{i}\omega\text{t}), \tag{40}$$

$$\mathbf{h}(\text{t}) = \mathbf{h}_0 \exp(-\text{i}\omega\text{t}), \tag{41}$$

and putting them into the Landau-Lifshitz equation of the dynamic field and magnetization leads to the so-called linearized version of the Landau-Lifshitz equation, where $\hat{e}_z$ is the unit vector along the direction of the magnetic field.

The linearized version of the Landau-Lifshitz equation can be seen in formula (42):

$$i\omega\mathbf{m}(t) = \hat{e}_z \times (-\omega_M\mathbf{h}(t) + \omega_H m(t)), \tag{42}$$

with $\omega_M = |\gamma|\mu_0 M_s$ and $\omega_H = |\gamma|\mu_0 H_0$.

Due to the assumption of only small dynamic deviations, the component of the magnetization along the z-axis differs only slightly from the state of equilibrium, making the static component approximately the same as the saturation magnetization $M_0 \approx M_s$.

The solution to the linearized version of the Landau-Lifshitz equation connects the varying magnetization to the dynamic magnetic field, which can be written as

$$\mathbf{m}(t) = \bar{\chi}\mathbf{h}(t), \tag{43}$$

with $\bar{\chi}$ being the Polder tensor for the susceptibility

$$\bar{\chi} = \begin{bmatrix} \chi & -i\kappa \\ i\kappa & \chi \end{bmatrix}, \tag{44}$$

where $\chi = \frac{\omega_H\omega_M}{\omega_H^2-\omega^2}$ and $\kappa = \frac{\omega\,\omega_M}{\omega_H^2-\omega^2}$.

This Polder tensor can describe a magnetization system with an externally applied dynamic magnetic field $\mathbf{h}(t)$. If the system is excited by a frequency ω_H, the elements of the tensor diverge and show a behavior where the damping is neglected, following the approximations made earlier. This frequency is called the ferromagnetic resonance frequency, which is described later. The damping term can be put back into the Polder tensor after a substitution of $\omega_H \rightarrow \omega_H - i\omega\alpha$, where α is the Gilbert-damping parameter.

2.2.5. Ferromagnetic resonance

The ferromagnetic resonance describes an accumulation of phase in form of a wave. As a special case of spin wave where all magnetic moments precess at the same phase around the effective magnetic field vector, the ferromagnetic resonance can be described by a spin wave that has an infinite wavelength and a vanishing wavevector $|\mathbf{k}_{sw}| = 0$. The exchange interaction has no effect on this wave because the magnetic moments are always aligned parallel to each other [5,24,25].

A solution to the Landau-Lifshitz equation is given with an ansatz that includes a dynamic magnetization over time,

$$\mathbf{M}(\mathrm{t}) = \mathbf{M}_0 + \mathbf{m}(\mathrm{t}), \tag{45}$$

with $\mathbf{m}(\mathrm{t}) = \mathbf{m} \cdot \mathrm{e}^{\mathrm{i}2\pi\mathrm{ft}}$. This approach gives rise to a dynamic demagnetizing field. The precession is greatly influenced by shape anisotropy and crystal anisotropy.

Linearizing the Landau-Lifshitz equation with time-dependent magnetization and effective field results in a formula which gives the ferromagnetic resonance frequency $\mathrm{f_{FMR}}$ dependent on the demagnetizing tensor N of an ellipsoid and the effective magnetic field $H_{\mathrm{eff}} = H_{\mathrm{ext}} + H_{\mathrm{ani}}$. This formula is the so-called Kittel-equation:

$$\mathrm{f_{FMR}}(\mathrm{H_{eff}}) = \frac{|\gamma|\mu_0}{2\pi}\sqrt{(\mathrm{H_{eff}} + (N_\mathrm{x} - N_\mathrm{z})\mathrm{M_s}) \cdot \left(\mathrm{H_{eff}} + \left(N_\mathrm{y} - N_\mathrm{z}\right)\mathrm{M_s}\right)}. \tag{46}$$

For a thin and infinitely expansive film, magnetized in the direction of the x-axis and no magnetic crystal anisotropy, this leads to a simpler version of the Kittel formula for a thin film:

$$\mathrm{f_{FMR}}(\mathrm{H_{eff}}) = \frac{|\gamma|\mu_0}{2\pi}\sqrt{\mathrm{H_{eff}} \cdot (\mathrm{H_{eff}} + \mathrm{M_s})}. \tag{47}$$

2.3. Spin waves

The combined excitation of magnetic moments in a spin system of a magnetic solid is called a spin wave. The precession of neighboring magnetizations is shifted in phase, similar to the lattice vibrations in a solid where the atoms are shifted in space around the equilibrium position. Whereas the amplitude-modulated elementary vibrational motion is called a phonon, the excitation and phase shift of the magnetization precession is represented by a magnon. The value of the magnetization stays constant over time at the excitation of spin waves, which propagate the phase state of the precession of the magnetic moments around the direction of the magnetic field. The wavelength of the spinwave is given by the distance between two magnetic moments with the same phase state. A schematic representation of a spin wave and its wavelength can be seen in Figure 2. The frequencies of spin waves are in a range of a few GHz up to THz, corresponding to wavelengths of micrometers to nanometers, respectively [5,26,27,28].

A spin wave is bound to the same interactions as a single magnetic moment. For large wavelengths, where neighboring atoms are only slightly shifted in phase, the dipolar interaction dominates the propagation, and the exchange interaction can nearly be neglected. These waves are typically called dipolar dominated or magneto-static spin waves.

In an intermediate regime the waves are called dipolar-exchange spin waves. Due to the large shift in phase for close magnetic moments for small wavelengths, the exchange interaction is important in exchange-dominated spin waves.

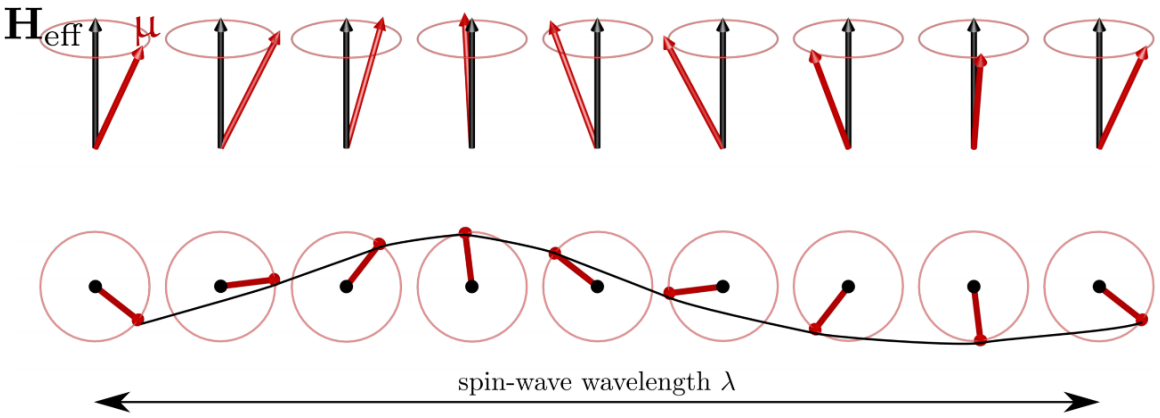

Figure 2: **Schematic representation of a one-dimensional chain of spins with a wavelength λ.** The periodic pattern of the spin wave is formed due to the coupling of the magnetic moments m which are precessing around the direction of the effective magnetic field, which is represented by the black arrow.
Retrieved from [10].

2.3.1. Spin waves in a thin film - magnetostatic dispersion relations

In a more general case, spin waves with a non-zero wavevector have magnetic moments which are not parallel aligned, unlike for the ferromagnetic resonance. This means the dynamic magnetization is now also dependent on the location and generates an equally location-dependent magnetic field.

The boundary conditions of the magnetostatic Maxwell-equations need to be satisfied at the boundary layers of a magnet, where a pinning effect takes place:

$$\nabla \times \mathbf{h} = 0. \tag{48}$$

$$\nabla \cdot \mathbf{b} = \nabla \cdot (\mathbf{h} + \mathbf{m}) = 0. \tag{49}$$

The definition of the magnetostatic potential $\Delta\phi = \nabla \cdot \mathbf{m}$, as well as the Maxwell equations lead to the introduction of a new formula, the Walker equation [5,27,29],

$$(1 + \chi)\left(\frac{\partial^2 \phi}{\partial x^2} + \frac{\partial^2 \phi}{\partial y^2}\right) + \frac{\partial^2 \phi}{\partial z^2} = 0, \tag{50}$$

with $\chi = \frac{\omega_H \omega_M}{\omega_H^2 - \omega^2}$, $\omega_M = |\gamma|\mu_0 M_S$ and $\omega_H = |\gamma|\mu_0 H_0$.

A solution of the Landau-Lifshitz equation under this condition was first found by R. W. Damon and J. R. Eshbach for a thin ferromagnetic slab. They found distinct characteristic dipolar spin waves, each behaving different in their dispersion characteristics: magnetostatic volume modes (backward volume (BVMSW) and forward volume (FVMSW) magnetostatic spin waves) and a magnetostatic surface mode (MSSW) also known as Damon-Eshbach (DE) spin-wave mode [30,31,32].

A thin film with thickness d lies in the x-z-plane, with the surface normal pointing along the y-axis. If the film is sufficiently thin, meaning it satisfies $|k_\parallel| d < 1$, the wavevector is quantized along the layer thickness with a quantum number of the quantization along the film thickness $p = 0,1,2,3,..$, where $k_\parallel$ is the component of the wavevector in the film layer. This thesis focuses on the fundamental mode of the Damon-Eshbach spin waves (i.e.: $p = 0$) as the higher thickness modes are separated by a few GHz in their frequency due to the strong exchange interaction in the thin film.

$$\mathbf{k} = \mathbf{k}_\parallel + \left(\frac{p\pi}{d}\right)\hat{\mathbf{e}}_y. \tag{51}$$

Waves which are standing along the film thickness are called perpendicular standing spin waves (PSSW). They have a small wavelength along the thickness, leading to the dominance of the exchange interaction.

Relating the wavevector k to the energy of the wave, the dispersion relation can be described by the following equation under the assumption of totally unpinned magnetic moments on the surface of the film [30]:

$$\omega(\mathbf{k}) = \sqrt{(\omega_H + \omega_A) \cdot \left(\omega_H + \omega_A + \omega_M F_{PP}(|\mathbf{k}|, \Theta)\right)}. \tag{52}$$

where $\omega_A = |\gamma| \frac{2A_{ex}}{\mu_0 M_S} |\mathbf{k}|^2$ with the exchange constant A_{ex} and F_{PP}, the dipolar matrix element, is given by the quantization P_{PP}, which is given for $p = 0$ in equation 54:

$$F_{PP}(|\mathbf{k}|, \Theta) = 1 - P_{pp}\cos^2(\Theta) + \omega_M \frac{P_{pp}(1 - P_{PP})\sin^2(\Theta)}{(\omega_H + \omega_A)}, \tag{53}$$

$$P_{00}(\mathbf{k}_\parallel) = 1 - \frac{1 - e^{-|\mathbf{k}_\parallel| d}}{|\mathbf{k}_\parallel| d}. \tag{54}$$

Magnetostatic volume modes have a real component of the wavevector along the thickness of the film. This wavevector is quantized and builds a standing wave. Magnetostatic surface modes on the other hand have an imaginary component of the wavevector along the thickness of the film. The amplitude of the surface spin wave has its maximum at one surface of the layer and decreases exponentially relative to the surface. The wavelengths of magnetostatic spin waves are much smaller than the wavelengths of electromagnetic waves. Due to strong distinct characteristics in the behavior of the dispersion, the different dipolar magnetostatic spin waves shall be discussed in more detail. Figure 3 shows the different described spin waves as well as the characteristic dispersion relations for the three magnetostatic surface and volume spin waves in a permalloy.

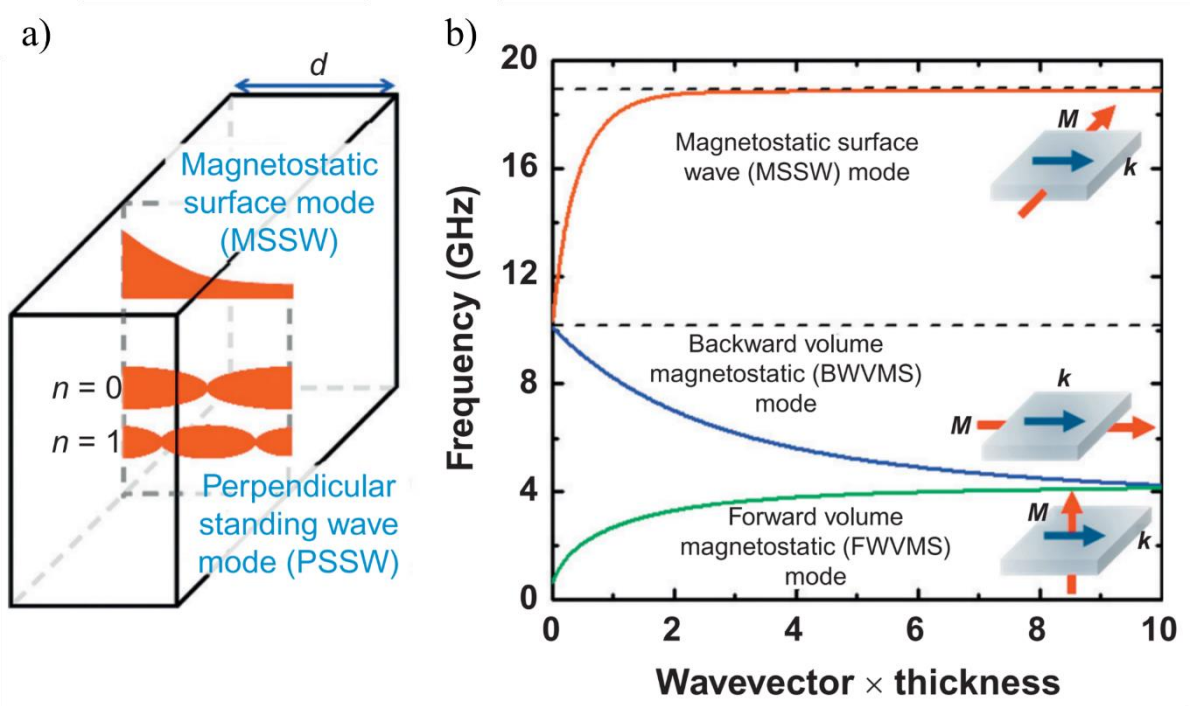

Figure 3: a) **Schematic of the modes of a perpendicular standing wave and a magnetostatic surface spin wave for a ferromagnetic thin film**. b) **Dispersion relation for the distinct magnetostatic surface and volume spin waves.** The spin-wave frequency is drawn in a schematic against the spin-wave wavevector for the MSSW, the BVMSW and the FVMSW modes in a permalloy ($Ni_{80}Fe_{20}$). This graph also includes a visual description of the directions of magnetization and propagation of the spin waves relative to each other.
Retrieved from [27].

2.3.2. Backward volume magnetostatic spin wave

If the direction of the applied magnetic field, and therefore also the magnetization direction, and the wavevector of the spin wave are parallel (**k ∥ M),** or the angle between them is $\Theta = 0$, then this spin wave is called a backward volume magnetostatic spin wave . The dispersion relation for such a spin wave is given by the following formula using the film thickness d:

$$\omega_{\mathrm{BVMSW}} = \sqrt{\omega_{\mathrm{H}}\left[\omega_{\mathrm{H}} + \omega_{\mathrm{M}}\left(\frac{1 - \mathrm{e}^{-|\mathbf{k}_{\parallel}|\mathrm{d}}}{|\mathbf{k}_{\parallel}|\mathrm{d}}\right)\right]}. \tag{55}$$

For a vanishing wavevector **k**, the dispersion relation results in:

$$\omega_{\mathrm{FMR}} = \sqrt{\omega_{\mathrm{H}}(\omega_{\mathrm{H}} + \omega_{\mathrm{M}})}. \tag{56}$$

The demagnetizing field has no effect in this geometry. Due to the wavevector being parallel to the magnetization, such spin waves have a negative dispersion. Their group velocity, defined by $\mathbf{v}_{\mathrm{g}} = \partial\omega/\partial\mathbf{k}$, is antiparallel to the phase velocity, which means their group velocity is negative. This thesis has direct relations to former studies [1,10] where the investigated nano-scaled YIG samples were put in a magnetic field along the propagation direction of the spin waves. In this work, the magnetic field was applied perpendicular but still in plane of the propagation direction.

2.3.3. Forward volume magnetostatic spin wave

The bias magnetic field is applied in such a way that its direction points out of the film's plane. An approximation of the dispersion of a forward volume magnetostatic spin wave is given by:

$$\omega_{\mathrm{FVMSW}} = \sqrt{\omega_{\mathrm{H}}\left(\omega_{\mathrm{H}} + \omega_{\mathrm{M}}\left(1 - \frac{1 - \mathrm{e}^{-\mathbf{k}\mathrm{d}}}{\mathbf{k}\mathrm{d}}\right)\right)}. \tag{57}$$

The ferromagnetic resonance for the forward volume magnetostatic spin wave can be determined by taking the limit of $|\mathbf{k}| \to 0$, which results in $\omega_{\mathrm{FMR}} = |\gamma|\mu_0 H_0$.

The frequency of a FVMSW is lower due to the magnetization being perpendicular to the surface, which leads to a demagnetizing field.

2.3.4. Magnetostatic surface spin waves

This type of spin wave is investigated in this thesis to show the propagation dynamics in a YIG waveguide with a thickness below 100 nm. If the magnetic field is applied in such a way that the magnetization, which points in the direction of the magnetic bias field, and the propagation of the spin wave are orthogonal to each other, meaning $\mathbf{k} \perp \mathbf{M}$, then these spin waves are called magnetostatic surface spin waves, or Damon-Eshbach spin waves, named after R. W. Damon and J. R. Eshbach, who first described them theoretically.

MSSWs have the fastest group velocity and the highest excitation efficiency [33] among the discussed spin waves. The dispersion relation of Damon-Eshbach spin waves is given by the following formula:

$$\omega = \sqrt{\left(\omega_H + \frac{\omega_M}{2}\right)^2 - \left(\frac{\omega_M}{2}\right)^2 e^{-2|\mathbf{k}|d}}. \quad (58)$$

In the limit of a vanishing wavevector, the ferromagnetic resonance can be obtained:

$$\omega_{FMR} = \sqrt{\omega_H(\omega_H + \omega_M)}. \quad (59)$$

As stated before, a magnetostatic surface spin wave has the maximum of its amplitude at the surface of the thin film. As its amplitude is exponentially decaying up to the middle of the layer, the spin wave is localized to one surface of the film depending on the magnetization and the direction of the propagation of the wave. The maximum of the amplitude can only switch the corresponding surface when the direction of the applied magnetic field or the direction of the propagating spin waves is rotated by 180°. However, the amplitude of the spin wave is almost constant across the thickness for a thin film.

The Damon-Eshbach spin waves show characteristics of non-reciprocity in the propagation direction. One direction of the propagation is interfered constructively by the applied magnetic field component pointing out of the plane H_z, which is generated by an antenna, whereas the other direction shows destructive interference.

2.3.5. Spin-wave excitation and detection

Depending on the involved mechanisms, the magnetization dynamics can range from microseconds to femtoseconds in their time scale. There exist many different techniques to investigate the fundamental properties of the spin waves and their usage in the magnetic recording industry [23,34,35].

A micrometer-sized antenna on the waveguide with an alternating current running through produces a varying Oersted field. When this field is perpendicular to the direction of propagation, it creates a torque on the precessional magnetization of the spins and therefore induces a Damon-Eshbach spin wave. Another way to excite spin waves is to use the spin-

transfer-torque, which modifies a spin-polarization current in a non-magnetic layer by torque with the orientation of a magnetic one. Furthermore, there exists a magnetoelectric cell which is connected in between the waveguide. Due to the application of an electric field, the piezoelectric layer in the magnetoelectric cell produces stress. Therefore, this layer changes the magnetization in another layer and exerts a torque on the waveguide, inducing a spin wave.

The excitation of the spin wave in this thesis is done by an antenna because magnetostatic spin waves have the highest excitation efficiency. This efficiency depends on the geometry of the external magnetic field, and the magnetization, where it has the largest value when the generated excitation field of the antenna is perpendicular to the magnetization in the sample. Furthermore, the excitation efficiency is depending on the width of the antenna. This means a bigger antenna has a smaller efficiency in exciting bigger wavevectors. In this thesis, the investigated wavevectors are in a small range around $|\mathbf{k}| \approx 0$ such that the width of the antenna does not matter. Lastly, the efficiency is also dependent on the quantization of the wavevector, where the excitation efficiency decreases for uneven modes with $1/n$. The YIG sample is placed on top of the CPW antenna, which conveys a magnetic Oersted field with a microwave-frequency and excites therein the precession of the magnetization.

2.3.6. Propagation loss

An ideal spin wave would propagate forever without attenuation. However, the Landau-Lifshitz-Gilbert equation states a damping of the Larmor precession depending on the time derivative of the magnetization. This leads to an eventual alignment of the magnetization direction and the effective magnetic field in the whole system.

The damping of the magnetization precession usually has components of viscous and non-viscous nature. The attenuation of a metal is greatly influenced by the spin-orbit coupling, whereas the interaction of the magnons and phonons is dominating in insulators. The non-viscous part of the damping is caused by inhomogeneities in the lattice structure, such as impurities, shifts and distortions, but also by a non-intrinsic process called two-magnon scattering [3,5,36]. This scattering process describes the interaction of the uniform mode and spin waves over the range of several wavevectors.

In a system, where the damping is purely viscous, the relaxation time T_0 of a mode is given by the Gilbert damping parameter α and the resonant frequency of the uniform precession mode ω_{FMR}.

$$\frac{1}{T_0} = \omega\alpha. \tag{60}$$

This gives the time where the amplitude of the magnetization decays to a factor of $1/e$ of the maximum. Generally, the relaxation time for a particular mode and geometry T_k, where the amplitude of the magnetization drops matching an exponential decay with $M(t) = M_{max}(0)\exp\left(-t/T_k\right)$ defines a loss per unit time

$$L = \frac{8.686}{T_k} \cdot 10^{-6}(dB/\mu s). \tag{61}$$

This description using the linearization of the Landau-Lifshitz equation does not hold for large amplitudes of the spin wave. Then, multi-magnon-scattering decreases the lifetime of spin waves additionally.

The relaxation time is strongly dependent on the type of material and the present interactions therein. Metallic materials typically have a relaxation time in the range of nanoseconds, where electric insulators, like YIG, can reach up to several hundred nanoseconds.

3. Methodology

Following the description of the theoretical background of the magnetization dynamics this chapter shall provide an overview of the methods which have been used in this thesis. Different methods can be used to analyze the magnetization dynamics of spin waves.

The first section of this chapter describes the basics of micromagnetic simulations which have been used to shine light on the dynamics of the magnetization in magnetic nanostructures.

Detection of a spin wave can be done by time-resolved magneto-optical Kerr effect (TR-MOKE) measurements, the ferromagnetic resonance technique (FMR) and Brillouin-Light-scattering- (BLS) measurements, where the latter will be discussed in detail in the following chapter. Although it involves expensive instruments and has an extremely sensitive alignment, the TR-MOKE technique has a highly localized probe area ($\sim 1 \mu m^2$) and gives a high resolution in time. The BLS is a powerful technique to detect small magnetic excitations in the investigated material and has a high sensitivity for the wavevector. It measures the dispersion of the wavevector in thin ferromagnetic films, multilayers, and patterned nanostructures depending on the frequency of the spin wave. It allows the research of spin waves in the time-, space- and phase-domain. This investigation method is used in this thesis to detect and analyze the magnetization dynamics of the Damon-Eshbach geometry and shall be explained in the second part of this chapter.

3.1. Numerical simulations

Magnetic materials can now be investigated at very small scales due to advances in fabrication and analytic technology, as well as the modelling and simulation thereof [37]. These numerical simulations use the magnetization dynamics of magnetic structures described by the ordinary time-differential LLG. Methods solving this type of equation include the Finite Element Method (FEM) and the Finite Difference Method (FDM).

The former method solves the differential LLG equation numerically without being bound by the geometry of the studied sample as it operates on the minimization of energy in the system. This simulation method is often used in problems including heat transfer, fluid flow, structural analysis, or electromagnetic potential. The discretization of the sample, also called finite elements, create a mesh in which a set of algebraic equations is solved for different boundary values by approximating an unknown function [38]. As the name of the Finite Difference Method suggests, this numerical technique solves differential equations by estimating

derivatives with finite differences at discrete points, dividing the simulated structure into cuboidal cells. Opposed to curved samples, prism-like ones are easy to be calculated and give a better representation of the demagnetization field of the sample. This problem can be reduced via an implementation in the code of the micromagnetic simulations.

The Finite Element Method gives the solution as a set of functions defined on a small subsection of the sample which lets the result be known in every point of the domain. Although the FEM has a higher order of approximation in its simulations compared to the FDM, it is often rejected due to the lower computational power needed by the Finite Difference Method. Moreover, in more complex problems, such as the computation of the flow dynamics of a sample, the FDM will provide faster results. A GPU-based micromagnetic simulation program, called MuMax^3 was developed at the DyNaMat group at Ghent University [39]. This program based on the Finite Difference Method has a speed-up of the order of 100x compared to traditional CPU-based simulators. The micromagnetic simulations in this thesis were performed using this MuMax³ solver.

3.1.1. Basics of micromagnetic simulations and MuMax³

The micromagnetic simulation program MuMax³ calculates the space- and time-dependent magnetization dynamics in magnetic materials ranging from nano- to micro-sizes via the discretization of the sample and a finite difference method-based solver, similar to the technique used in OOMF, Micro-Magnum or GpMagnet.

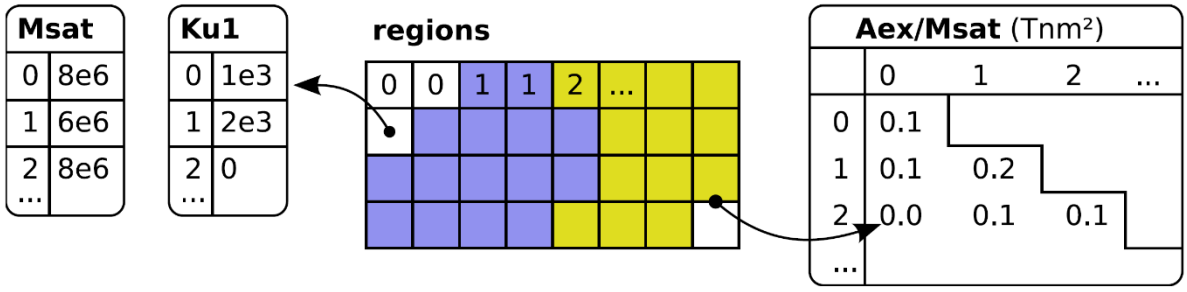

Figure 4: **Representation of the storing of different quantities.** The simulated cells are given a region index according to their nature of the material. The quantities relating to the volume of the cells are stored in a vector indexed by the cell's region index, such as the saturation magnetization and anisotropy constants. The exchange strength, and other quantities showing the interaction between neighboring cells are stored in a lower triangular matrix.
Retrieved from [40].

This program allows even relatively inexpensive gaming GPUs to perform the simulations. It includes the Landau-Lifshitz micromagnetic formalism, a calculation for the magnetostatic field and the Heisenberg exchange amongst other useful features [37,40,41].

MuMax³ delegates a region index between 0 and 256 to each cell of the sample, where a different region index implies a different material. Quantities relating to the volume of each different discretization of space are treated in the center thereof, whereas coupling quantities, such as the exchange strength, are considered on the faces between cells which allows arbitrary coupling between cells with different materials. According to their region index, the volumetric and the coupling quantities are stored in a vector and a triangular matrix, respectively, which can be seen in Figure 4.

Adding to these space-dependences, the parameters which are changing over time, like the externally applied field or an electric current density, can be added via an introduction of any function of time f(t) and a continuously varying spatial profile $g(\mathrm{x},\mathrm{y},\mathrm{z})$ which are multiplied in order to get the changing behavior $f(\mathrm{t}) \times g(\mathrm{x},\mathrm{y},\mathrm{z})$.

For the simulations performed in this thesis, the sizes of the grid cells are of the order of 10 nm, where the thickness of the sample gives the thickness of the cells. This estimate holds true for the case of a thin film, where the profile along the thickness is uniform.

3.1.2. Spin-wave excitation in micro-structures via micro-strip antenna

The spin waves in this simulation are excited by a micro-strip antenna which is patterned across the magnetic spin-wave waveguide. The excitation pulse is given in the form of a sinc function to excite an as wide as possible range of spin waves in the waveguide, with a cut-off frequency $f_\mathrm{c} = 10$ GHz and the excitation field $h(\mathrm{t})$.

$$\mathrm{h}(\mathrm{t}) = \mathrm{sinc}(2\pi \mathrm{f_c t}). \tag{62}$$

A Fast Fourier Transformation turns this sinc function into the corresponding energy spectrum, which gives a rectangle function in the frequency domain. Spin waves with a frequency greater than the cut-off frequency will not be excited due to the FFT intensity dropping to zero.

Due to a limited simulation time, some non-uniform signals can be found below f_c. To avoid influences, a cut-off frequency much higher than the frequencies in the region of interest is chosen.

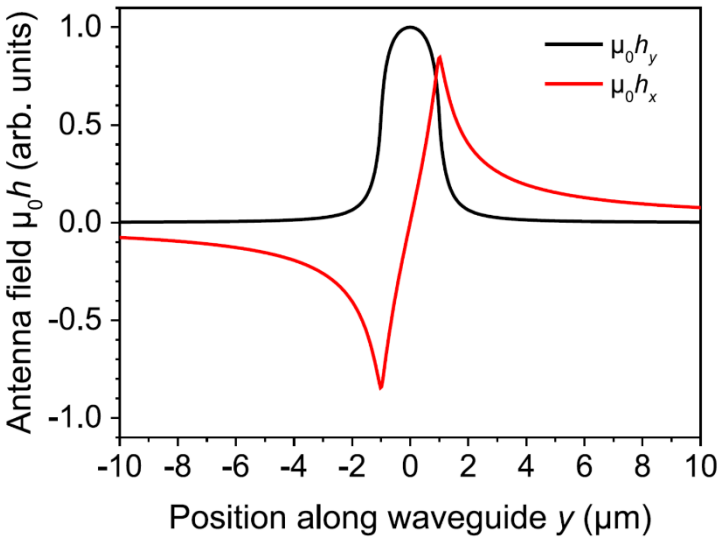

Figure 5: **Components of the antenna field.** The schematic of the components of the antenna field generated by a micro-strip antenna <with width $w_a = 2a = 2\,\mu m$ and thickness $d_a = 2b = 500\,nm$. The out-of-plane component $\mu_0 h_y$ is confined under the area of the antenna, with its maximum in the center thereof. The in-plane component depicted in red has its maxima at the edges of the antenna and a sign change at the center thereof. This component shows non-reciprocal behavior.
Retrieved from [42].

The frequency resolution Δf is defined by the total simulation time T [4].

$$\Delta f = \frac{1}{T} \tag{63}$$

In the performed simulations the spin wave only has a dependency on the x-position of the antenna field which simplifies the antenna field to only one dimension. The excitation efficiency of any waveguide mode falls by $1/n$, with the efficiency of even modes dropping to zero. The mode profile is independent of the spin-wave wavevector k_y, which is fixed by the waveguide width w_{eff} and the mode number n.

To calculate the antenna field components which can be seen in Figure 5, the field distributions in-plane $\mu_0 h_y(y, x)$ and out-of-plane $\mu_0 h_x(x, y)$ defined by Formula 65 and Formula 66 are needed which are given by the total current I running through the antenna and the antenna's width $2a$ and thickness $2b$. It shall be noted that the formulas were derived for a DC-current but proven to give a good approximation of the time-average of the components in a dynamic Oersted field generated by an AC current running through the antenna [42]. By adjusting the

function with help functions HF_i and the prefactor $pf = \frac{I\mu_0}{8\pi ab}$, the formulas for the field distributions can be simplified.

$$HF_1 = a - y;\ HF_2 = a + y;\ HF_3 = b - x;\ HF_4 = b + x. \tag{64}$$

$$\begin{aligned}\mu_0 h_y(y,x) = \ pf\Bigg[&\frac{HF_1}{2}\ln\left(\frac{{HF_1}^2 + {HF_3}^2}{{HF_2}^2 + {HF_4}^2}\right) + HF_2\ln\left(\frac{{HF_2}^2 + {HF_3}^2}{{HF_2}^2 + {HF_4}^2}\right)\\ &+ HF_3\,\mathrm{atan}\left(\frac{HF_1}{HF_3}\right) + HF_4\,\mathrm{atan}\left(\frac{-HF_1}{HF_4}\right) - HF_3\,\mathrm{atan}\left(\frac{-HF_2}{HF_3}\right)\\ &- HF_4\,\mathrm{atan}\left(\frac{HF_2}{HF_4}\right)\Bigg].\end{aligned} \tag{65}$$

$$\begin{aligned}\mu_0 h_x(x,y) = \ pf\Bigg[&\frac{HF_3}{2}\ln\left(\frac{{HF_1}^2 + {HF_3}^2}{{HF_2}^2 + {HF_3}^2}\right) + HF_4\ln\left(\frac{{HF_1}^2 + {HF_4}^2}{{HF_2}^2 + {HF_4}^2}\right)\\ &+ HF_1\,\mathrm{atan}\left(\frac{HF_3}{HF_1}\right) + HF_2\,\mathrm{atan}\left(\frac{-HF_3}{HF_2}\right) - HF_1\,\mathrm{atan}\left(\frac{-HF_4}{HF_1}\right)\\ &- HF_2\,\mathrm{atan}\left(\frac{HF_4}{HF_2}\right)\Bigg].\end{aligned} \tag{66}$$

In the Damon-Eshbach geometry, the in-plane component of the antenna field is mainly confined under the area of the antenna, which acts as an efficient local spin-wave excitation source due to the torque perpendicular to the static magnetization. The out-of-plane component of the antenna field, which has its maxima at the edges of the antenna, changes its sign in the center and extends significantly longer along the y-direction. The resulting excitation gives rise to the non-reciprocity in the spin-wave excitation in the MSSW-geometry.

3.2. Brillouin light scattering microscopy

BLS is an important tool to investigate spin waves in addition to ferromagnetic resonance, neutron scattering, methods based on the magneto-optic Kerr effect, such as TR-MOKE measurements, or FMR measurements. Although it involves expensive instruments and has an extremely sensitive alignment, the TR-MOKE technique has a highly localized probe area and gives a high resolution in time, whereas the BLS has a high sensitivity for the wavevector. It

measures the dispersion of the wavevector in thin ferromagnetic films, multilayers, and patterned nanostructures depending on the frequency of the spin wave.

Brillouin light scattering is built on the interaction of a monochromatic light with a sample. This sample's optical density is changing over time due to acoustic modes (phonons), magnetic modes (magnons) or temperature gradients therein. These variations interact with the light via inelastic scattering such that its energy, therefore also its frequency, and the path of the light are altered. This optical technique allows to investigate not only microstructures, but also cells and biological tissues and their properties non-destructively with focused light [43].

In the subsections of this chapter, the physical background of BLS, the micro-BLS, as well as the experimental setup and its components shall be discussed in greater detail, as this is the used method to obtain experimental results in this thesis.

3.2.1. Magnon-photon scattering – Brillouin Light scattering

The Brillouin light scattering process describes the inelastic scattering of photons, as the elementary quanta of light, in the visible range of the light spectrum by magnons, as the quasi-particle of spin waves, which is depicted in Figure 6. The energy and the momentum are conserved within the photon-magnon scattering process when the system is totally time-invariant and invariant to translations. For an incident photon with frequency ω_i and wavevector $\mathbf{k}_i$ scattered inelastically by a magnon with frequency ω_{sw} and wavevector $\mathbf{k}_{sw}$ the following equations hold true in an infinite medium:

$$\begin{aligned} \hbar\omega_s &= \hbar\omega_i \pm \hbar\omega_{sw}, \qquad \text{(energy conservation)} \\ \hbar\mathbf{k}_s &= \hbar\mathbf{k}_i \pm \hbar\mathbf{k}_{sw} \quad \text{(momentum conservation).} \end{aligned} \tag{67}$$

For spin waves propagating in thin films, the existence of interfaces leads to a breaking of the invariance considering translations in the direction perpendicular to the surface. Then conservation of the momentum is only fulfilled for the projection of the spin-wave wavevector in the plane. The transferred wavevector $\mathbf{k}_\parallel$to the magnons is given by the incidence angle θ relative to the surface normal of the incoming photon and its wavelength.

$$k_\parallel = k_i \sin(\theta) \tag{68}$$

The maximum transfer of the wavevector at an incidence angle of $\theta \sim 90°$ in backward scattering geometry is two times the momentum of the incident photon. In this case, the perpendicular

component of the wavevector can be neglected, if the film thickness, the light penetration depth, or the size of the region of the mode are sufficiently big.

In the context of quasi-particles interactions, the energy of the scattered photon, given by $\hbar\omega_s$, can be larger or smaller than the energy of the incident photon. This corresponds to different scattering mechanisms where a magnon can be generated (decrease in energy) or annihilated (increase in energy). These inelastic light-scattering processes involve a magnetic excitation (one magnon process) [44] and are called the Stokes process or the anti-Stokes process, respectively. The probability for the process of generation and annihilation of magnons at a finite temperature ($T \gg \hbar\omega/k_b \sim 5K$) are nearly the same.

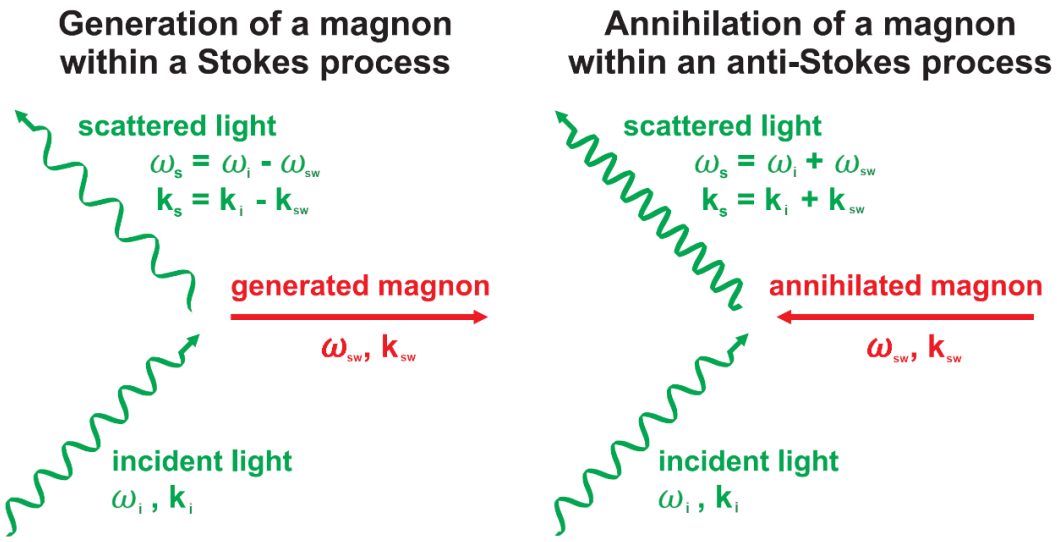

Figure 6: **Schematic representation of the inelastic scattering processes between photon and magnon.** The left process shows the generation of a magnon, also called the Stokes process. Energy and momentum of the incoming light are passed onto the created spin wave. The right part shows the annihilation of a magnon in an inelastic scattering process, which is called the anti-Stokes process. Due to destroying the spin wave the scattered light has a higher frequency and wavevector than the incoming light.
Retrieved from and modelled after [44].

Contrary to this assumption, experiments show that there exists an asymmetry in the intensities of the Stokes and the anti-Stokes peaks in the BLS spectrum, originating from different causes, e.g. a quadratic term of the spin density in the dielectric permittivity, the presence of thermally excited spin waves, strong optical absorption due to non-diagonal components of the spin-spin

correlation function or the non-reciprocity in the propagation direction for the surface spin waves.

The latter attribution can be described by the exponential decay of the surface waves into the material, where a different number of scattered photons is accumulated for each propagation direction due to the finite penetration depth of light [45].

As seen in light scattering experiments in different magnetic materials, the full theory of light scattered by magnetic excitations must include both the dipole-dipole interaction and the exchange interaction in the materials, as well as surface anisotropies at the surfaces of the film [46].

Classically, the interaction between the spin waves and light can be thought as a modulation of the dielectric tensor of the magnetic medium. As the spin-orbit coupling is periodic in time and space and corresponds to the frequency and wavelength of the spin waves, the precessing magnetic moments affect the modulation of the electronic properties and add a time-dependent component to the electric polarization. This can be visualized as a moving phase grating, which moves with the phase velocity of the spin waves along the direction of the wavevector. A planar wave of the incident light is scattered on this grating and experiences a Doppler shift. The frequency of the scattered light is given by

$$\omega_s = \omega_i - k_{sw} \cdot v_{sw}, \tag{69}$$

where the velocity of propagation of the spin wave v_{sw} is given by

$$v_{sw} = \frac{\omega_{sw}}{k_{sw}^2} k_{sw}. \tag{70}$$

The angle under which the scattered light is detected enables a detection of the wavevector transfer in the layer. Two scattering geometries can be distinguished: forward scattering and backward scattering geometry. The forward scattering geometry is defined as the process where light passes through a transparent sample under a distinct angle and is detected at a defined angle. If the sample is opaque, the backward scattering geometry provides results. Here, the reflected light can be detected by the same lens under the same angle θ.

Another cause for the modulation of the dielectric tensor can be phonons. Therefore, it is important to distinguish the photons scattered by magnons or phonons. The measurement of the

frequency shift is performed by a Tandem-Fabry-Pérot interferometer, whereas the transmitted wavevector is determined by the angle between incoming and outgoing photons.

3.2.2. Micro-focus Brillouin-light scattering microscopy (μBLS)

A combination of sub-micrometer spatial resolution and sub-nanosecond temporal resolution for the investigation of non-uniform spin-wave modes is found in the Brillouin-light scattering microscope. This technique allows measurements of the frequency as well as measurements of the wavevector of spin waves [47]. To get a good selectivity of the wavevector the light must therefore be focused onto a relatively small solid angle which can be done by installing lenses with a long focal length. The minimal size of the focus d_{min} onto the sample is determined by the wavelength of the installed laser λ_{laser}, the numerical aperture $NA = n \sin(\theta)$ of the lens where the angle θ is the half of the aperture angle and n is the refractive index of the surrounding medium (for air: $n \approx 1$).

$$\mathrm{d_{min}} = 0.61 \frac{\lambda_{\mathrm{laser}}}{\mathrm{NA}}. \tag{71}$$

A low value of the numerical aperture guarantees a high wavevector resolution, which results in a large size for the laser focus on the sample. Such a setup reaches a typical value of the diameter of $d_{\mathrm{min}} \approx 50$ μm which limits the size of the investigated samples to films and macro-structures. On the other hand, a higher numerical aperture equals a higher possible value of the incidence angle of the laser beam, which increases the largest measurable wavevector $\mathrm{k_{max}}$. For the used setup, this yields a maximum wavevector of $k_{\mathrm{max}} = 0.023\ \mathrm{nm^{-1}}$.

$$\mathrm{k_{max}} = \frac{4\pi}{\lambda_{\mathrm{laser}}} \cdot \mathrm{NA}. \tag{72}$$

Moreover, the response of the system should be recorded with a temporal resolution below 50ps to detect spin-wave frequencies of 10 GHz, and delay times of above 10 ns lead to frequency resolutions of 0.1 GHz [47,48].

To measure micro-structures, different focusing optics and a better realization of the sample positioning system compared to a conventional BLS microscope are needed. Moreover, metallic layers are not transparent for visible light which requires the backward scattering geometry. This scattering geometry is accompanied by a decreasing detection efficiency for rising values of the wavevector. The whole light scattered by a spin wave with wavevector close

to zero is detected by the objective. For a larger wavevector, only the light from the outermost edges of the lens can be detected after being scattering on the sample, whereas the rest of the inelastically scattered light misses the objective and therefore cannot be detected. Research on microstructure is achieved by installing a micro-focusing objective with a higher numerical aperture. Following an increase in the solid angle of the, the range of the wavevectors expands. However, the resolution of the wavevectors is reduced. This enhanced setup is called micro-focused BLS or Brillouin-light scattering microscopy (μBLS).

3.2.3. μBLS - experimental setup

This subsection describes the experimental setup used in this thesis to show the magnetization dynamics of YIG in the Damon-Eshbach geometry. The laser beam in a μBLS microscope can ideally be focused down to the theoretical diffraction limit of 200 – 250 nm onto the sample, and the scattered light can effectively be collected from this little area. The magnetization dynamics of samples in sub-micrometer sizes can be accessed now.

A diode-pumped single-mode solid state laser with a wavelength of $\lambda_{\mathrm{laser}} = 457\,\mathrm{nm}$ and maximum power of $P_{\mathrm{laser}} = 100\,\mathrm{mW}$ serves as a light source for this setup. Due to the high contrast of the interferometer, the longitudinal secondary modes need to be repressed further by installation of an additional modefilter for the laser in the beam path. Via a transmission of part of the beam to a nearby photodiode, the chosen lasermode can be stabilized. In the main beam path, the linearly polarized beam can be turned into a desired polarization with a rotatable $\frac{\lambda}{2}$ plate, which allows the following polarizing beam splitter to set the beam to a decoupled laser power. The polarizing beam splitter then divides the laser light into two parts, one of which is deflected and used as a reference in the interferometer. This reference has a low intensity, approximately 2% of the initial beam, so that the beam does not damage the photodetector. A telescope widens the transmitted part and guides the beam through an aperture which cuts it in such a way that only the homogeneous center of the beam is sent forward. The aperture is limited in diameter to illuminate the microscope objective fully for a maximum spatial resolution. A second $\frac{\lambda}{2}$ plate is inserted to allow a variable rotation of the polarization which fixes the laser power before hitting the sample.

By guiding the beam to the objective or to the beam blocker, depending on the polarization of the beam. The polarized beam is then focused by the microscope objective onto the sample [49]. The used compensating microscope objective has a numerical aperture of NA = 0.85, a working distance of 0.7 mm and a magnification factor of 100. This results in a minimal focus diameter of $d_{\min} \approx 400\,\text{nm}$ following formula 71. The maximum incidence angle of the objective which limits the largest detectable spin-wave wavevector is defined by the numerical aperture (NA).

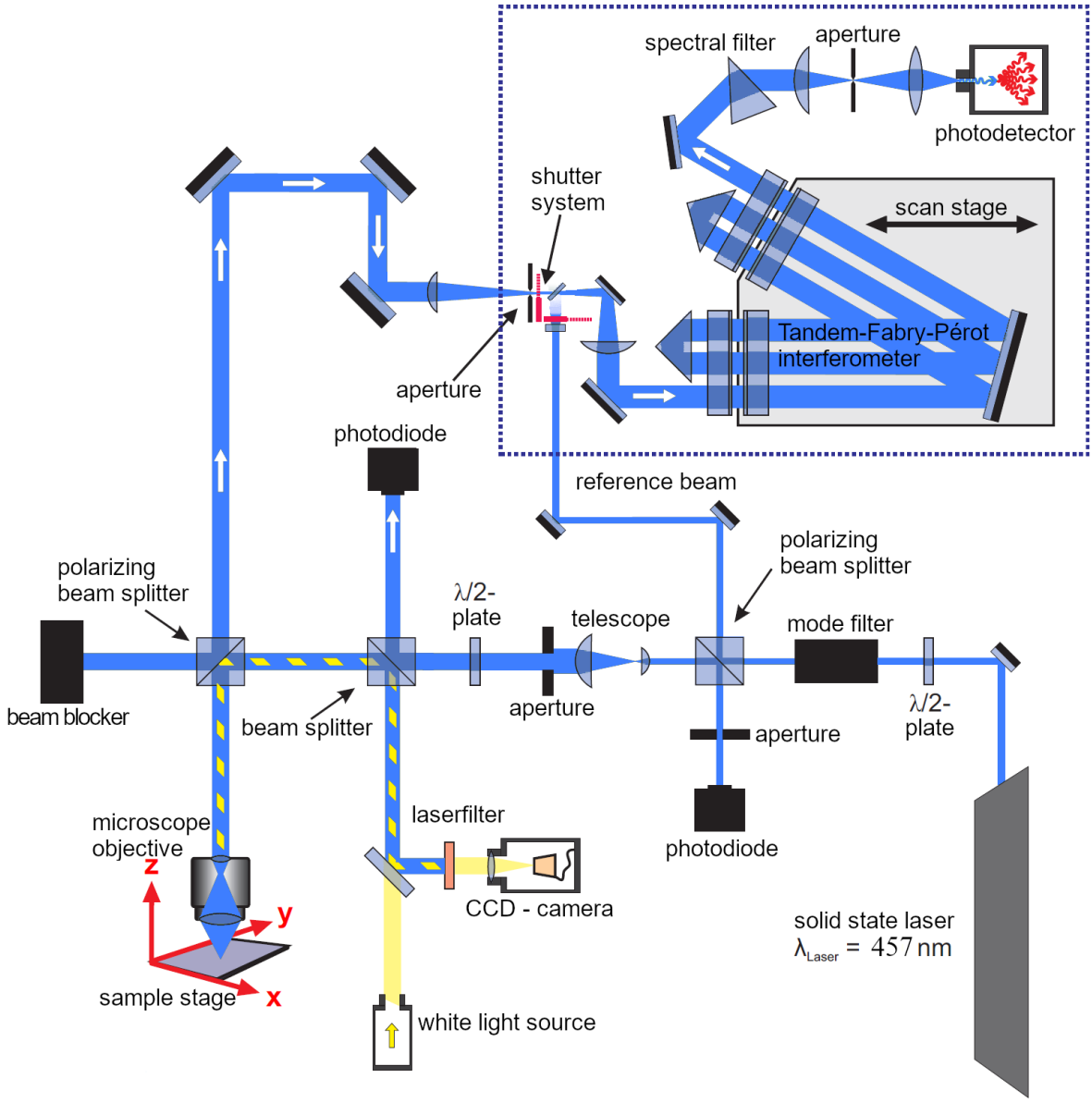

Figure 7: **Schematic representation of an experimental setup of a micro-focused BLS.** The upper part in the encased box represents the interferometer which is used in the frequency analysis.

Retrieved from and modeled after [10].

For the objective in this thesis, the maximal incidence angle is $\theta_{max} = 48.59°$.

$$\theta_{max} = \arcsin\left(\frac{NA}{n}\right). \tag{73}$$

The largest value of the spin-wave wavevector in backward scattering geometry, where the values of the incoming and outgoing wavevector are equal, is given by

$$k_{sw} = k_s \sin(\theta) - k_i \sin(\theta) = 2k_i \sin(\theta). \tag{74}$$

Due to the backward scattering geometry, the objective not only focuses the light onto the sample, but also collects the scattered light. It is important to note that the polarization direction of the light scattered by spin waves is rotated by 90°, whereas elastically scattered light remains unaffected. The backscattered light is guided through the second beam splitter to the interferometer where the frequency of the light is analyzed. The beam splitter is set perpendicular to the initial polarization. As the elastically scattered light remains unchanged, its intensity is strongly suppressed, while the inelastically scattered light can easily pass through due to the change in polarization. This significantly increases the signal-to-noise ratio, even though the intensity of the elastically scattered light is much higher than the intensity of the transmitted magnon signal.

The photodetector which is used to collect the photons is extremely sensitive to the intensity of the invading light. Therefore, the light is guided into a black box, which is shown in Figure 7 by an outline around the interferometer. Moreover, a shutter system blocks the sample beam when the Fabry-Pérot interferometers (FPIs) are in resonance with the frequency of the laser light, which is the case for the elastically scattered photons. The sample beam is then guided through a set of prisms which only transmit a selected frequency range of the inelastically scattered light before entering the photodetector. A computer operated program controls the data acquisition and its visualization [45].

A stable position of the sample is needed to investigate the magnetic excitations in micro-structures. A piezoelectric stage is used to always keep the sample in focus in the z-direction. This piezoelectric stage is automatically adjusted by using the returning beam of the elastically scattered light. To realize also an exact lateral positioning of the laser focus onto the sample the sample stage is adjustable with micrometer screws. In addition to the laser beam, a second beam coming from a white light source, in a different wavelength so that the used light sources do not interfere with each other, and a CCD camera are placed into the beam path. This camera

captures the surface of the sample. The CCD camera has a built-in laser filter for protection from the intensity of the laser. After a calibration of the invisible (to the camera) laser spot along a path with changing reflection with the camera and the first photodiode, the camera offers another way for exact positioning of the laser onto the sample. This setup gives a good spatial resolution. The frequency measurements are performed by the Tandem-Fabry-Pérot interferometers which are discussed in the following subsection.

3.2.4. Tandem-Fabry-Pérot interferometer

The detection of the spin-wave excitations needs a high spectral resolution and a high dynamic contrast. This can be achieved by a Tandem-Fabry-Pérot (TFP) interferometer which is formed by two single Fabry-Pérot interferometers connected in series.

A FPI, named after Charles Fabry and Alfred Pérot who created the device in 1899, is built on a technique which is extremely sensitive to detecting the frequency of light [50]. Two coplanar plates with a highly reflective coating on the surfaces facing each other and an anti-reflex coating on the outer sides build the basis of such an interferometer.

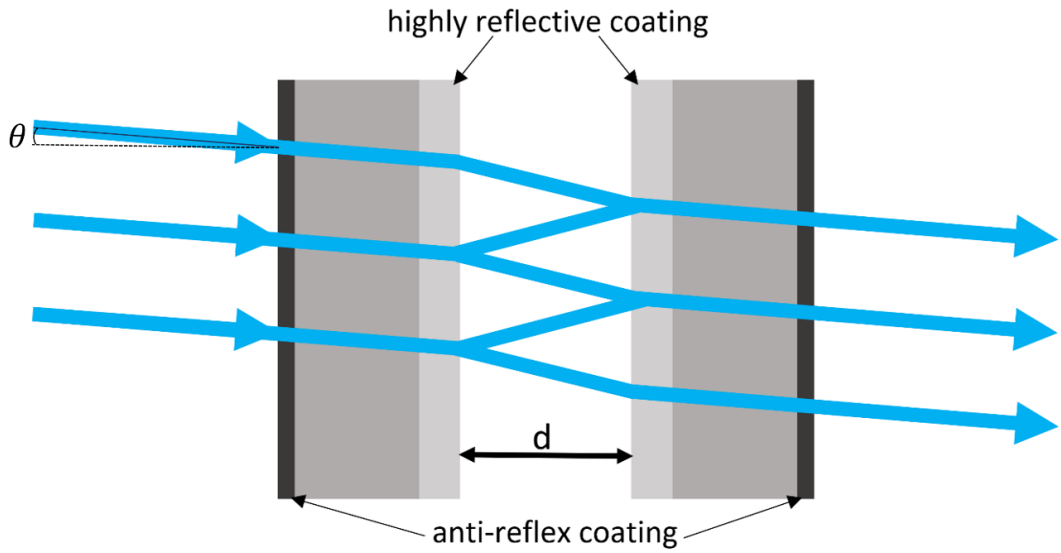

Figure 8: **Schematic of a Fabry-Pérot interferometer.** Two coplanar mirrors are facing each other at a distance d. The plates are coated with a highly reflective layer and an anti-reflex layer to ensure light is coming into the interferometer with minimal losses. Due to the multiple beam interference inside the interferometer the transmitted light has a specific value of the wavelength.
Modelled after [51].

The plates are installed at a distance d, which can be seen in Figure 8. The dielectric coating on the inner sides of the plates is not perfectly reflective. Typically, the values for reflection lie between 92 and 96% of the light intensity, which means that for each reflection a small part of the beam gets transmitted through the plates of the FPI. The intensity of the transmitted light of a particular wavelength is determined by the reflection coefficient R of the plates and the phase difference $\Delta\varphi$ of two beams interfering with each other. For light with wavelength λ coming into the interferometer with a refractive index n under an angle θ relative to the surface normal the multiple-beam interference is determined by the difference in phase of the single beams.

$$\Delta\varphi = \frac{2\pi\Delta s}{\lambda} = \frac{4\pi n d}{\lambda \cos(\theta)}. \tag{75}$$

For a maximum of transmittance through the interferometer, therefore having constructive interference, the phase difference of two beams must be an integer multiple of 2π which gives the following relation after being put in the last equation:

$$2d = m\lambda \qquad \text{with } m \in \mathbb{N}. \tag{76}$$

The change in the optical path length Δs of two consecutive reflections or transmissions of the light is given by the double of the distance of the plates d times the refractive index n. This index can be neglected for the TFPI due to $n = 1$ for air which fills the space between the plates. The intensity of the transmitted light of a FPI is given by the Airy function for light incoming parallel to the surface normal ($\theta = 0°$) [52].

$$I_t = I_0 \frac{1}{1 + F \sin^2\left(\frac{\Delta\varphi}{2}\right)}. \tag{77}$$

where the I_0 is the intensity of the incoming light and F is the technical finesse of the interferometer, which gives the resolution of the FPI. The finesse can be obtained via the relation of two neighboring orders of transmission, called the free spectral range (FSR), and their corresponding half-width (FWHM). It can also be calculated by the reflection coefficient R of the mirrors.

$$F = \frac{4R}{(1-R)^2} = \frac{\Delta\lambda}{FWHM}. \tag{78}$$

For a higher finesse and therefore a sharper resolution, the reflection of the mirrors must be increased. The equation of the intensity of the transmitted light predicts periodic peaks of the frequency in the Fabry-Pérot interferometer as a function of the phase difference, and it therefore is indirectly dependent on the distance between the mirrors. Moreover, a higher finesse concentrates the transmission maxima further around a certain frequency, or wavelength and integer multiples of the phase difference in the FPI. For a fixed mirror distance only light with a wavelength of $\lambda = 2d/m$ can pass through the filter, where m is an integer. For a variable mirror spacing, the investigated frequency range increases. However, a larger distance between the plates is accompanied by a decrease in the frequency resolution.

To measure the difference in frequency of two different beams, e.g. the reference beam and the light beam scattered by the magnons, a specific mirror spacing is used to maximize the transmission intensity of the second beam. The wavelength of the reference beam λ_r must be known to calculate the corresponding second wavelength at a certain difference in the distance of the plates $\Delta d = d_s - d_r$. The unknown wavelength λ_s can then be determined by computing the following equation.

$$\lambda_s = \lambda_r \left(1 + \frac{\Delta d}{d_r}\right). \tag{79}$$

The difference in frequency Δf is given using the speed of light c and the difference in the mirror spacing of the corresponding two beams.

$$\Delta f = f_s - f_r = \frac{c}{\lambda_r}\left(\frac{1}{1+\frac{\Delta d}{d_r}} - 1\right) = -\frac{c}{\lambda_r}\frac{\Delta d}{d_r + \Delta d} \approx -\frac{c}{\lambda_r}\frac{\Delta d}{d_r}. \tag{80}$$

The approximation $d + \Delta d \approx d$ in the last part is given due to the fact that the difference in the mirror spacings between the reference beam and the second beam lie in the order of the wavelength of the used laser light, whereas the mirror spacing of the reference beam is significantly larger, with values lying in the millimeter range. The changing of the mirror spacing in the experiment is realized via a piezoelectric control system of the distance.

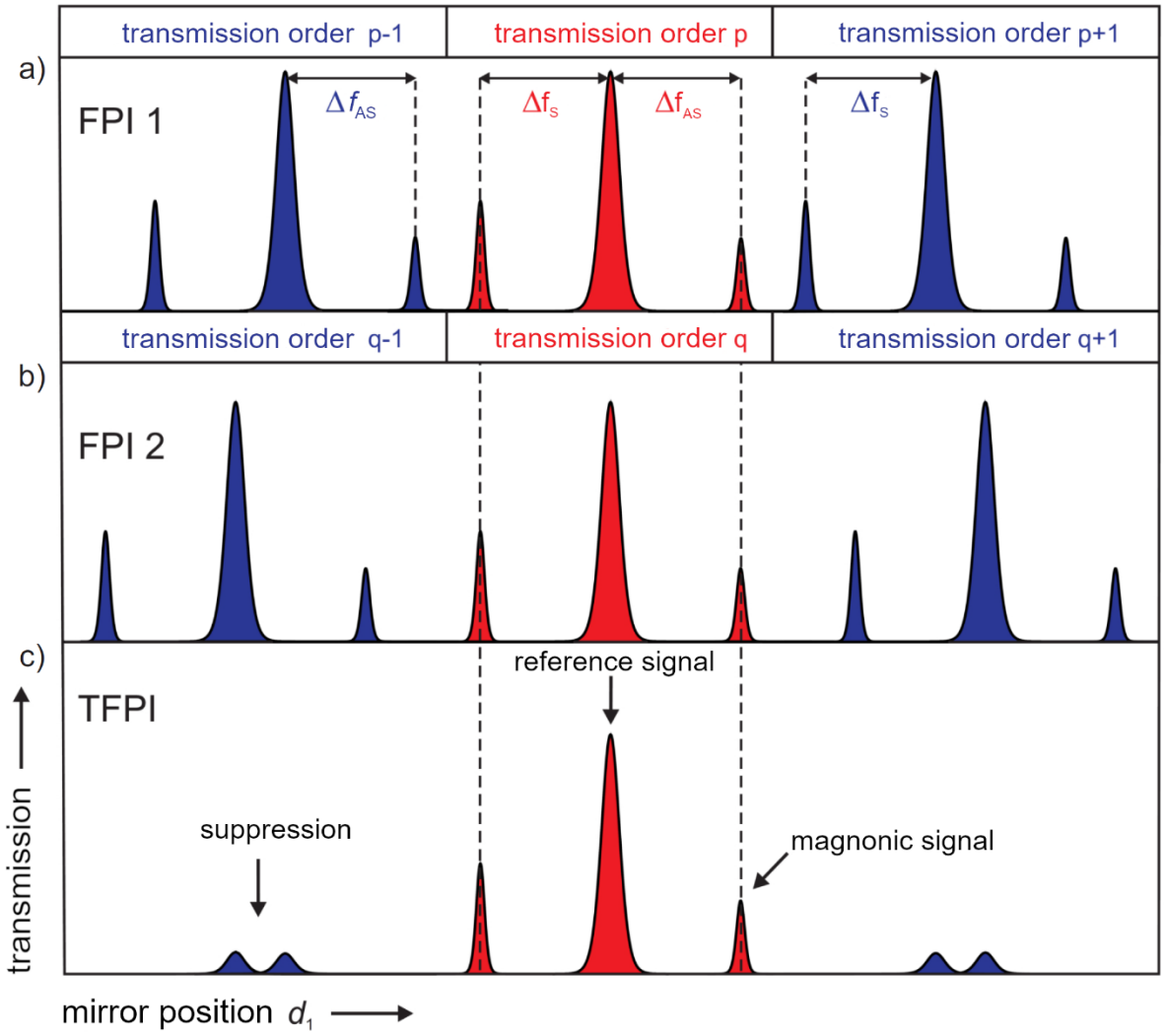

Figure 9: a) **and** b) **Transmission characteristics of the single FPIs and** c) **the Tandem-Fabry-Pérot interferometer.** The Stokes and the Anti-Stokes signals of the inelastically scattered beam are depicted for the main order of transmission of the reference beam and the second orders. c) The TFPI can distinguish between the signals from the different processes. Retrieved from [15].

According to the relation of the change in the mirror spacing and the frequency shift, the free spectral range of the transmission is passed once when Δd is exactly half of the laser wavelength.

$$\mathrm{FSR\ [GHz]} = \Delta \mathrm{f}\left(\frac{\lambda_\mathrm{r}}{2}\right) \approx \frac{\mathrm{c}}{2\mathrm{d}} \approx \frac{150}{\mathrm{d[mm]}}. \tag{81}$$

The equation for the frequency difference shows that the measured frequency shift of the inelastically scattered photons is linearly dependent on the difference in the mirror spacing. This technique provides for the frequency analysis in the BLS setup. The light scattered by the magnonics excitations can be shifted towards higher or lower values relative to the frequency of the reference beam due to the Stokes- or Anti-Stokes process, which can be seen in Figure 9. A singular Fabry-Pérot interferometer is neither capable of distinguishing between the two mechanisms nor able to assign the signal due to the periodic transmission function: The interferometer sees the Stokes-signal of a specific wavelength and the Anti-Stokes signal of a lower transmission order to be the same. This problem is removed when instead of a singular Fabry-Pérot interferometer two FPIs in series are used.

A clear classification of the signal shifted in frequency is achievable with the TFPI, developed by Dr. John R. Sandercock [53]. The two interferometers are mounted in a specific angle α to each other, as depicted in Figure 10.

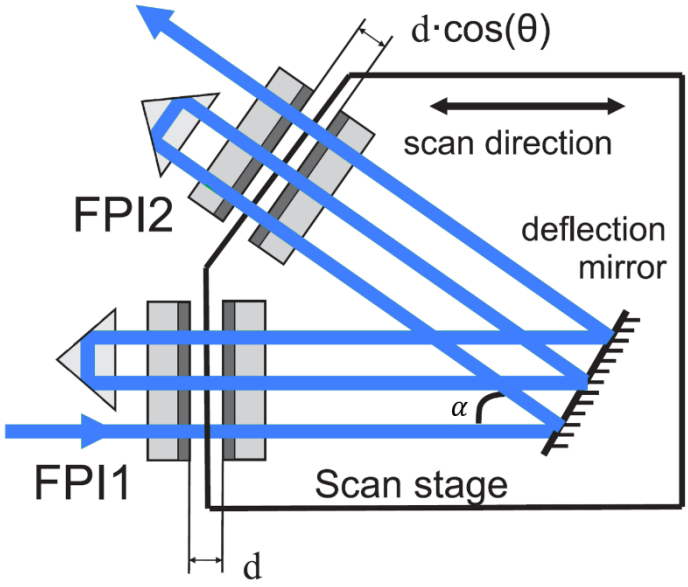

Figure 10: **Schematic of the Tandem-Fabry-Pérot interferometer.** Both interferometers are arranged in such a way that the beams are aligned under an angle α. The light scattered inelastically by the sample is guided by a deflection mirror through each interferometer three times. Only the main order is transmitted fully, whereas the second orders of the transmission are suppressed. At last, the beam enters the photodetector, where its intensity is measured. Retrieved from [45].

The left sides of both Fabry-Pérot interferometers are permanently mounted, whereas their right sides are mounted onto the same translational stage to allow a synchronized change of the mirror spacings in both interferometers. The beam is guided via a deflection mirror through two prisms which allows the light to pass each interferometer three times. Hence, it is also called Tandem-(3+3)-Fabry-Pérot interferometer. Due to the arrangement of the interferometers in an angle, the transmission orders of the second interferometer are further apart than those of the first FPI. The relation of the mirror spacing of the first FPI d_1 and the distance of the mirrors d_2 in the second interferometer is given in the following equation for a shift of the stage Δz.

$$\mathrm{d}_2 = (\mathrm{d}_1 + \Delta \mathrm{z}) \cos(\alpha). \tag{82}$$

A similar change appears in the transmission orders of the second Fabry-Pérot interferometer. When the first interferometer changes its transmission order from $p \rightarrow p + 1$ after a shift of $\Delta z = \frac{\lambda}{2}$, the transmission orders q of the second FPI vary in the following way:

$$\mathrm{d}_2 = \mathrm{q}\frac{\lambda}{2} + \frac{\lambda}{2}\cos(\alpha) = \frac{\lambda}{2}(\mathrm{q} + \cos(\alpha)) \neq \frac{\lambda}{2}(\mathrm{q} + 1). \tag{83}$$

This relation does not fulfill the condition for maximum transmission of the next peak in the second interferometer. Only the main order gets transmitted through both interferometers, whereas the second orders are suppressed due to the repeated passing through the mirrors.

3.2.5. Measurements of YIG nanostructures

In this thesis, the used YIG waveguide has a thickness of 44 nm and is grown on top of a Gadolinium Gallium Garnet (GGG) substrate by liquid phase epitaxy. A gold coplanar waveguide antenna was placed onto the YIG nanostructure. Spin waves were excited by applying radiofrequency continuous wave currents or short pulses through the antenna to the waveguide. Furthermore, a large magnetic bias field is applied in-plane, but perpendicular to the propagation direction of the spin waves. The value of the external magnetic field $\mu_0 H_{\mathrm{ext}} = 270\ \mathrm{mT}$ is chosen to ensure a completely transversely magnetized state of the medium. The laser of the BLS setup is then focused through the substrate, which is transparent to the laser, onto the sample using a compensating microscope objective to get information on the spin-wave propagation in a nanostructured YIG waveguide.

4. Theoretical investigations of internal magnetic field and spin wave dispersion of YIG nanostructures

The properties of YIG have been researched extensively since the middle of the 20th century. However, this included mostly fundamental research on the topic of magnetization dynamics in a material and propagation of spin waves as well as studies on structures at or above micrometer size which were applied in microwave technology [10]. Nowadays, the fabrication of nanostructures is essential to the progress in technology, which requires substantial understanding of the fundamental properties as well as a description of the magnetization dynamics in nanometer sized YIG. This chapter of the thesis investigates the propagation of spin waves in a nano-structured YIG waveguide, where spin waves are propagating in-plane of, but perpendicular to the externally applied magnetic field. The numerical simulations in this thesis were performed using the mentioned micromagnetic simulations program MuMax3, using the Landau-Lifshitz-Gilbert formalism to describe the magnetization dynamics.

The first part of this chapter focuses on the distribution of the internal magnetic field of the waveguide, depending on the width thereof. Three different waveguides are investigated to show the effects of varying widths on the distribution of the magnetic field inside the material. Furthermore, the effective magnetic field is described along a cross section in direction of the width. A comparison of the magnetic field of the differently sized waveguides shows the changing behavior when the width is reduced.

In the following chapter, the dispersion curves of the waveguides with different widths are discussed with the help of micromagnetic simulations. Spin waves are simulated in a homogeneous YIG material with an externally applied magnetic field as well as an antenna placed on top of the waveguide, which generates an additional Oersted field to excite the surrounding media in such a way that spin-wave propagation is possible.

Thereafter, the preexisting theory is used to show the analytics of the different behaviors for magnetostatic surface spin waves: the dispersion curve, the group velocity versus the wave number, as well as the lifetime and propagation length plotted against the wavenumber of the Damon-Eshbach spin waves in a YIG material. The mentioned properties were analyzed at different effective magnetic field values along the width of the waveguide to show the changes of spin-wave propagation.

As a conclusion, the existing analytical calculations are compared to the numerical simulations in the last subchapter. It shall prove that the preexisting analytical theories are not sufficient to calculate the dispersion curves of nano-structured YIG.

4.1. Internal field distribution of waveguides with different sizes

As the shape of the used YIG waveguide is rectangular, the sample is subject to shape anisotropy. This forces the internal magnetic field of the used material to be inhomogeneous, especially at the edges of the waveguide due to demagnetizing effects. The first part of the results obtained in this thesis via micromagnetic simulation deals with this inhomogeneity and shows the change along the width of the waveguide.

Using the MuMax³ program to simulate micromagnetic materials, a simple waveguide with square cross section can be created. The size of the cuboidal cells in the structure are defined for calculation via the Finite Difference Method, which this program uses. Moreover, the material parameters are set for different regions. This micromagnetic simulation assumes a single homogeneous waveguide for simplicity reasons. The dimensions of the simulated nanoscale waveguide are given by a length of 20 µm, a thickness of 44 nm and a width of 44 nm. The parameters of the material used in this simulation were extracted from former experiments using this waveguide and are the saturation magnetization $M_{\mathrm{sat}} = 1.45 \cdot 10^5 \ \frac{\mathrm{A}}{\mathrm{m}}$, the exchange stiffness, also known as the exchange constant, $A_{\mathrm{ex}} = 4.5 \cdot 10^{-12} \ \frac{\mathrm{J}}{\mathrm{m}}$ and the dimensionless Gilbert damping constant $\alpha = 2 \cdot 10^{-4}$. Moreover, the damping constant in this numerical simulation is scripted to increase exponentially to the ends of the waveguide. This ensures that at the end of the simulated waveguide nothing gets reflected and alters the result due to a non-infinite length of the waveguide. These material parameters are the same as the parameters of the YIG waveguide used in the BLS experiment later.

At the start of the simulation a random magnetization is assigned to the cells in the waveguide. An external magnetic field is applied in such a way that it is perpendicular to the propagation direction of the waveguide such that the transmission of Damon-Eshbach waves is possible in this set-up. This external field is introduced with a constant value of $B_{\mathrm{ext,y}} = 0.27\ \mathrm{T}$, while having no values in the other directions. Afterwards, the dynamical components of the magnetization vector of the structure are brought back to the calculated ground state. The program automatically calculates the effective magnetic field inside the waveguide which is a result to the application of the external magnetic field and the demagnetization. The ground

state of the magnetization is saved again after letting the simulation, in which the single cells are affected by the external magnetic field, run for a small given time. All waveguides were simulated with the same thickness and length, but with different widths.

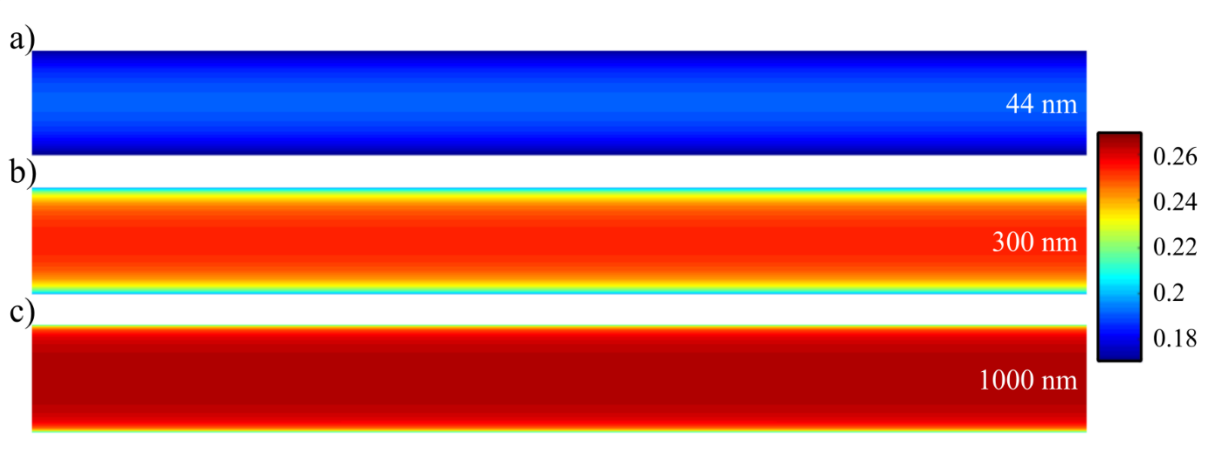

Figure 11: **Internal magnetic field**. These images show the simulated magnetic field inside the YIG material with different widths but the same length and thickness: a) 44 nm, b) 300 nm and c) 1000 nm. The scale indicates the strength of the magnetic field, given in Tesla, with a color code. Red shows a higher internal magnetic field and for different blue shades the magnetic field is smaller. Each maximum of the magnetic field of the different waveguides lies at the center of the waveguide's width. a) The 44 nm wide waveguide shows a smaller internal magnetic field than the other simulated structures over the whole width of the material. The magnetic field is subjected to a small, non-drastic change along the width of the waveguide. b) The magnetic field inside a waveguide of 300 nm width reaches a higher value than the smaller waveguide. c) The edges of a waveguide with 1000 nm width are subject to dramatic changes of internal magnetic field, whereas a majority inside the waveguide has a constant value.

The simulations for the different waveguide widths of 44 nm, 300 nm and 1000 nm all showed changes of the internal magnetic field at the edges of the waveguide. Figure 11 shows the internal magnetic fields of the waveguides from nanometer to micrometer widths, whereas Figure 12 shows the smallest nanostructured waveguide in a different intensity scale to better display the decrease of the internal magnetic field at the edges of the waveguide. Depending on the width of the waveguide, the change of the magnetic field inside the material was more drastic including a higher value at the center of the waveguide as well as a larger part in the middle where the magnetic field stays constant. However, a similar uniform magnetic field can be observed over most of the line along the width of the waveguide for the wider structures.

Even for the small waveguide there is a small part with no change in strength of the magnetic field. In the center of the structure, the magnetic field stays constant along the direction of the propagation of the spin waves in the assumption of a homogeneous YIG material. Therefore, the arising effects are solely dependent on the demagnetization.

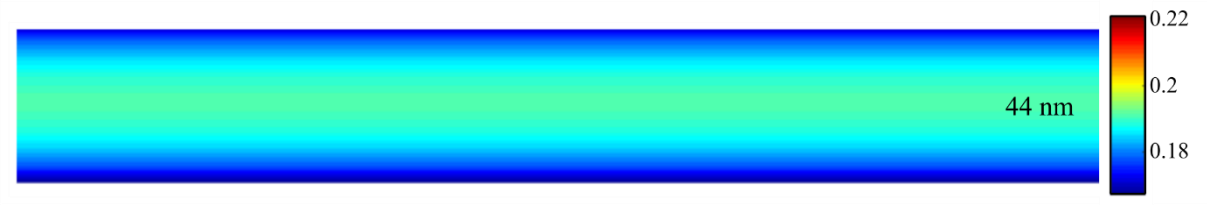

Figure 12: **Internal magnetic field of a 44 nm wide waveguide.** The intensity is scaled to better display the non-uniformity across the width of the nanostructured waveguide. The scale indicates the strength of the magnetic field, given in Tesla, with a color code.

At the edges of the waveguides with a larger widths, the change of the internal magnetic field is more pronounced than in the smaller waveguide due to its higher value in the center. Still, the nanostructured waveguide also changes the value of its internal magnetic field along the width. This shows that the more material there is to be magnetized, the more drastic the changes on the edges of the waveguide must be. More magnetization centers in a wider waveguide increase the value of the internal magnetic field up until a point where the magnetic field inside the material cannot increase anymore due to demagnetizing effects of the waveguide.

The extent of the spin dynamics is directly influenced by the material properties, interfacial conditions in a multilayer system of thin films or by the design of the waveguide. The effective magnetic field which directly influences the magnetization dynamics of a material is easily affected by the shape, pattern, and size of the waveguide. Finite-sized non-ellipsoidal magnetic elements therefore possess a non-uniform internal magnetic field which renders the calculation of the spin dynamics non-trivial.

For a more precise calculation of the spin dynamics the effective magnetic field must be known. It is directly dependent on the externally applied magnetic field with its static and time-dependent components on the demagnetizing field due to the form of the waveguide and the resulting stray fields, the exchange interaction, and several different resulting magnetic fields due to anisotropy caused by other deformations or impurities in the structure, as well as other components affecting the magnetization direction in the material. The demagnetizing field, and therefore also the effective magnetic field are spatially non-uniform along the width of the waveguide.

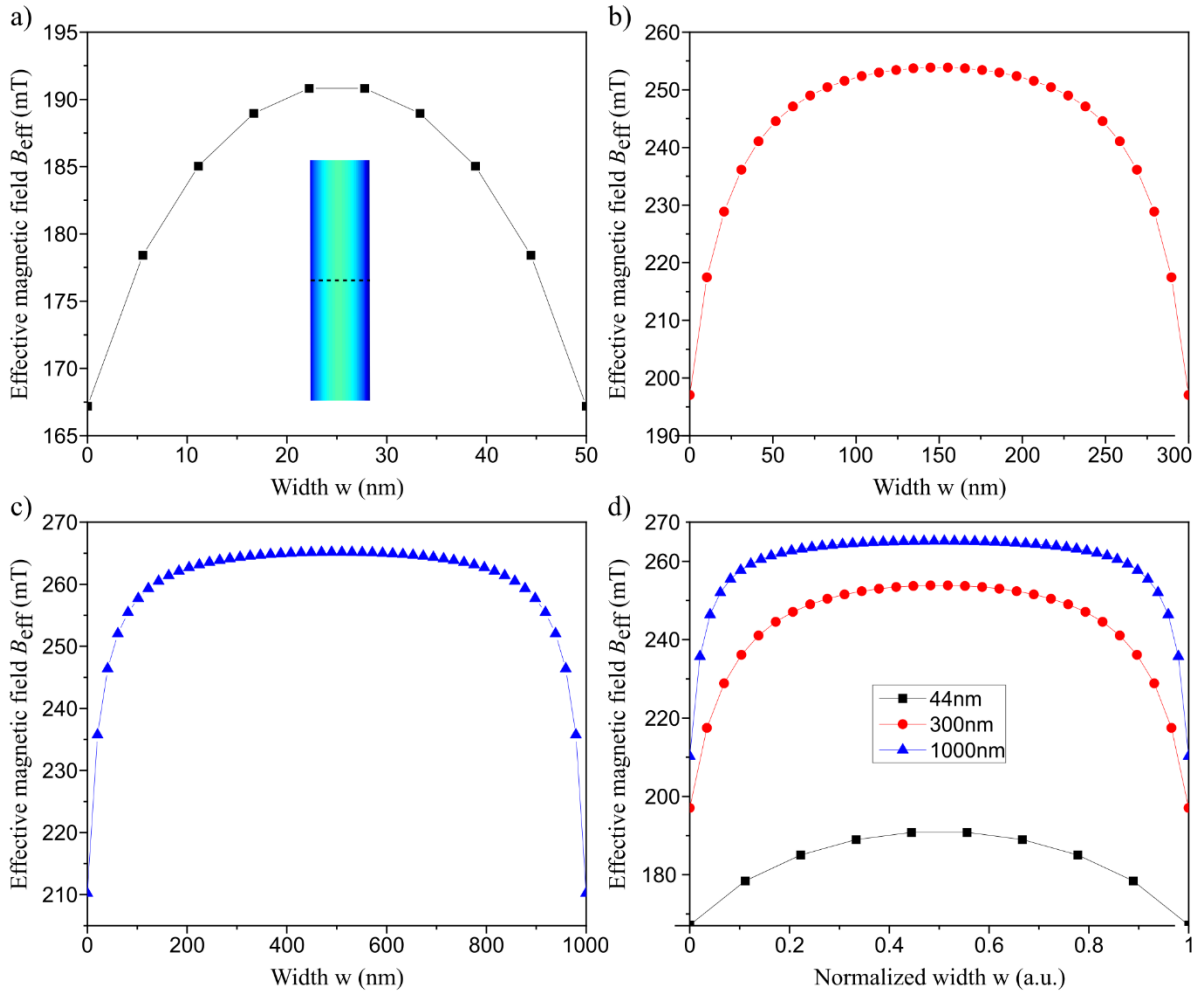

Figure 13: **Cross section of the effective magnetic field.** The different waveguides show different maximum values of the magnetic field along their widths. The x-axes of the first three images show the width of the different simulated structures: a) 44 nm, b) 300 nm and c) 1000 nm. The graphs are shown in different colors to be more recognizable in the assembled image (d). a) The first image illustrates the effective magnetic field of a 44 nm wide waveguide. A picture of the simulated structure inside the plot demonstrates the cross section where the values were extracted from. b) The 300 nm wide waveguide has a strong increase of the effective magnetic field near the edge. Compared to the 44 nm wide waveguide, the internal field of the 300 nm wide waveguide has dramatically increased at both edge and center. c) The plot of the effective magnetic field of the 1000 nm structure indicates a steep incline near the edges. A majority along the width of the waveguide is governed by a nearly constant value. This structure shows the highest strength of the effective magnetic field. d) The last graph shows the effective magnetic field (in units of mT) of all differently sized waveguides together in three distinct colors. Therefore, the widths of the waveguides have been normalized to an arbitrary unit. The plot shows that the smaller waveguide has a smaller magnetic field inside. The larger waveguides have a steeper incline of the effective magnetic field near the edges.

The used simulation program, MuMax³ [39,40], automatically calculates the effective magnetic field of the simulated material from the externally applied magnetic field and the self-induced field of the magnetized body which is calculated with the given material parameters and structure defining constants. The values of the effective magnetic field have been extracted along the width of the waveguide and put into a separate graph to show the cross section of the magnetic field. The effective magnetic field of the waveguide differs in strength, meaning a smaller value for a less wide design of the structure.

Moreover, bigger structures, such as a waveguide with a width of 1000 nm, have a larger part along the width of the material where the value of the effective magnetic field is nearly constant. A 44 nm wide waveguide only has parts along its width where the strength of the effective magnetic field is changing.

In transition between these two different phenomena, waveguides amid the two mentioned sizes, such as a 300 nm thick structure, show signs of both: a constantly changing effective magnetic field and a large part in the center of the waveguide, where the magnetic field is only subject to small changes in its amplitude. The effective magnetic field is highly non-uniform inside the structure. Figure 13 provides a graphic description of the internal magnetic field along the width of the waveguides, as well as a representation of the internal magnetic fields of the different sized waveguides compared to each other.

4.2. Dispersion curves of spin waves in a nano-scaled waveguide

A big part of the micromagnetic simulation in this thesis claims the finding of the dispersion curves of magnetostatic surface spin waves in a nanostructured YIG waveguide, which shows the propagation of wave modes in the Damon-Eshbach geometry. All simulated representations of the dispersion curves in this thesis are given in a frequency versus wave number regime.

Magnetostatic surface spin-wave modes have been extensively studied in the past due to their large amplitude of the spin wave and the relatively large propagation length [54] compared to the other spin-wave propagation modes. Many different Damon-Eshbach spin-wave devices have been developed. The conditions of wave propagation in a magnetic nano-sized structure differs greatly from usual waveguides, but due to the miniaturization in nanoelectronics smaller structures are needed in technology, and therefore also need to be researched. Compared to infinite film waveguides, new effects appear because the spin waves are strongly confined in space [55]. The calculation of the dispersion curve includes the dipole-dipole and exchange interaction, surface anisotropy and different possible sizes of the YIG waveguide. A fast and

accurate calculation thereof is especially important to model magnonic crystals with nanoscale features for future microwave data communication [41]. The micromagnetic simulations performed in this thesis were designed in such a way that reflections due to a non-infinite waveguide were non-existent. Moreover, a waveguide made of ideal YIG material was the base structure, meaning no impurities or defects were considered. Additionally, only the first wave modes were considered in the simulation of the dispersion curve.

The dispersion relation $\omega(k)$ gives an understanding of the characteristics of the propagation of spin waves in different materials. Computational methods can calculate the dispersion relations, which were traditionally obtained using experiments, but are more cost- and time-efficient for the price of approximations. The simplification of the experiment allows a good study of the dispersion relation for fundamental propagating modes. Higher order modes often deviate considerably from the expected curve. The magnetization dynamics of spin waves in a material are given by the Landau-Lifshitz-Gilbert equation [56]. The non-reciprocal behavior of spin waves is a direct effect of the asymmetric distribution of the out-of-plane component of the excitation field of the microstrip antenna [57]. Moreover, this non-reciprocity can be changed in accordance with the external bias magnetic field.

To calculate the spin-wave dispersion curve of a YIG waveguide in Damon-Eshbach geometry, the program starts with defining the material parameters. After defining the regions in the same way as before, the before calculated ground state of the magnetization is loaded into the simulation. Furthermore, an antenna is introduced to the structure. The CPW (coplanar waveguide) antenna is characterized by its half-width a and its half-height b, given by $a = 50\,\mathrm{nm}$ and $b = 25\,\mathrm{nm}$, and its position relating to the already characterized YIG waveguide. In this simulation, the antenna is placed directly on top of the waveguide where it generates an additional magnetic field due to a current running through. The Oersted field is assumed to be only one-dimensional since there is only a dependency on the x-position of the generated antenna field.

The antenna field is then calculated for every cell of the defined waveguide in x-direction. A second loop sets the antenna field for every cell in y-direction. The excitation is shifted to the center of the waveguide by defining the help functions, from the chapter Methodology, with half of the structure's size. In this simulation, the antenna current is set as $I = 1.4 \cdot 10^{-3}$ A. Subsequently, the excitation frequency of the antenna is established to be $f = 20$ GHz and the external magnetic field is added to the generated Oersted field in every cell with a time-modulation in the form of a sinc function.

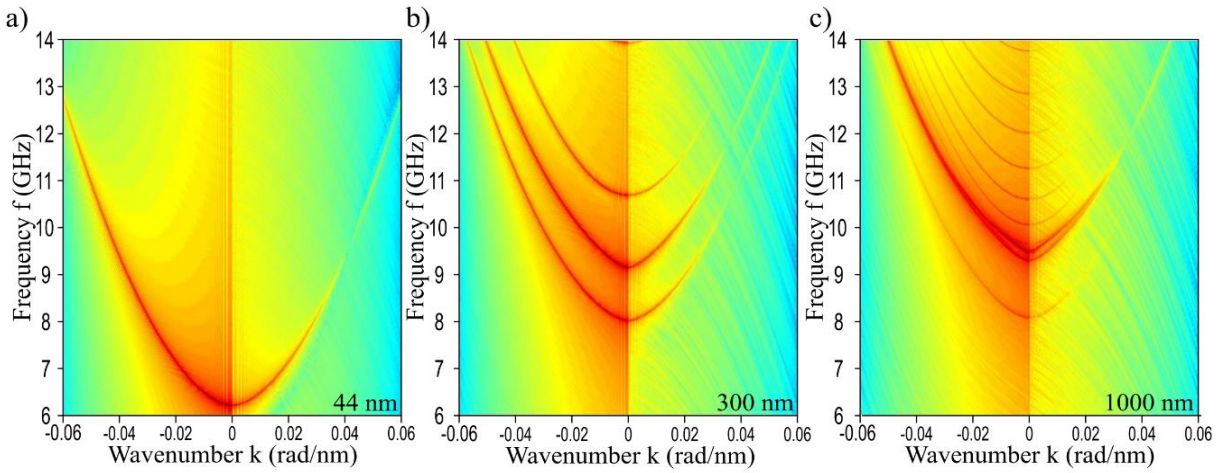

Figure 14: **Dispersion curves of waveguides with different thicknesses.** Three different plots show the dispersion relation of spin waves in Damon-Eshbach geometry in waveguides of different widths: a) 44 nm, b) 300 nm and c) 1000 nm. For a wider waveguide, fundamental propagating modes are shifted closer together in frequency. The color code shows the intensity of the propagating mode: blue with lower and red with higher intensity. For all dispersion relations a higher intensity can be observed in one direction than the other. This intensity difference indicates a non-reciprocity in a certain propagation direction. a) The 44 nm waveguide shows a singular intense propagating mode in the magnetostatic surface spin-wave propagation geometry. b) More modes of the propagating spin wave can be found in the investigated frequency range for a larger waveguide. c) In a waveguide of 1000 nm width many fundamental propagation modes are shifted closer in the studied frequency range.

The state of the magnetization in each cell, as well as the overall external magnetic field and the electric field of the antenna are saved after letting the simulation run for a specified short amount of time. The acquired data is then put through a Fast Fourier Transform program to get a plot of the dispersion curve in the frequency versus wave vector domain from the changing magnetization of the cells over the simulation time.

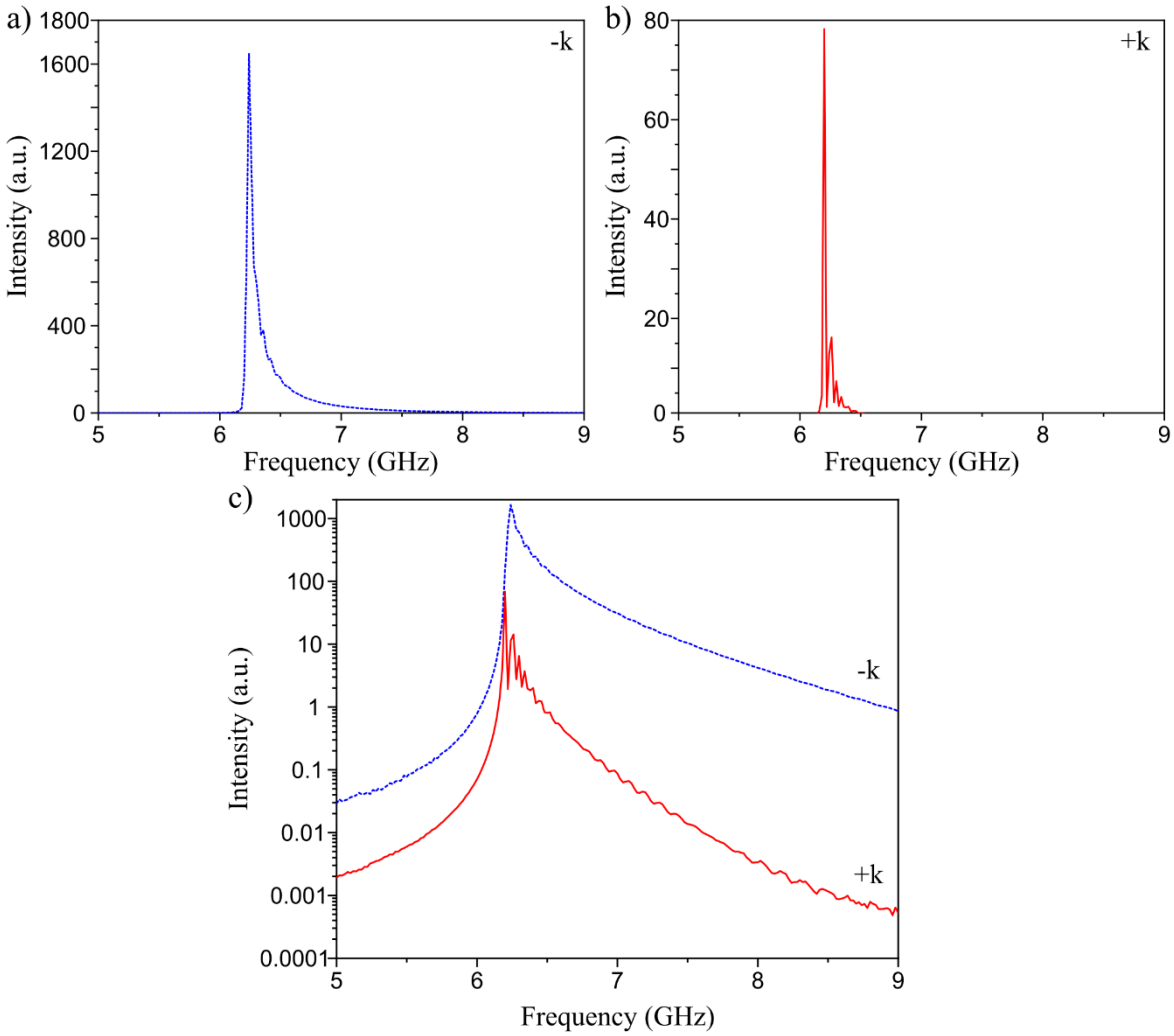

Figure 15: **Non-reciprocity of the dispersion curve of the 44 nm waveguide.** The plots depict the intensity of the simulated dispersion curve with a positive and a negative wavenumber, mirrored on the zero-value of the wavenumber. The intensity of the dispersion is plotted against the frequency of the spin wave a) for a negative wavenumber (5 µm left of the antenna), b) for a positive wavenumber (5 µm right of the antenna), and c) logarithmically for both in one plot for a better understanding of the difference in intensity. This demonstrates a non-reciprocity effect for Damon-Eshbach spin waves in a waveguide with a width of 44 nm.

In figure 14, the dispersion curves of three differently sized waveguides are plotted after a simulation of spin waves in Damon-Eshbach geometry in a YIG material. The intensity of the dispersion is in all three cases higher on the left side of the plot, which means that the material displays non-reciprocal properties, i.e. the intensity of the propagating spin wave depends on the sign of its wavenumber (or the direction travelled from the antenna) $I(k) \neq I(-\mathrm{k})$, where I is the intensity of the spin wave of a certain wavevector k of the propagating spin waves.

Figure 15 better demonstrates the non-reciprocity for a 44 nm waveguide. The plot shows the intensity of the dispersion relation on the left and the right side of the antenna, as well as a combination to show the drastic difference in intensity against the frequency of the spin wave. As can be seen in the plots, the intensity of the propagating spin waves is much higher for a negative wavenumber, which corresponds to the spin waves propagating left of the antenna, compared to spin waves with a positive wavenumber. These plots solidify that magnetostatic surface spin-wave modes show non-reciprocal behavior for spin waves with opposite sign of their wavevector in a nanostructured waveguide.

4.3. Analytical analysis of spin-wave dispersion curves

To calculate phenomena of magnetism at larger than interatomic distances the theory of micromagnetism was developed as a result to the continuum theory of magnetism [37]. In a classical approach the dispersion relation is derived from the spin-wave Heisenberg Hamiltonian, which only considers the spin moment.

To analyze the behavior of the propagation through a nano-structured YIG waveguide classically, the value of the effective magnetic field is needed.

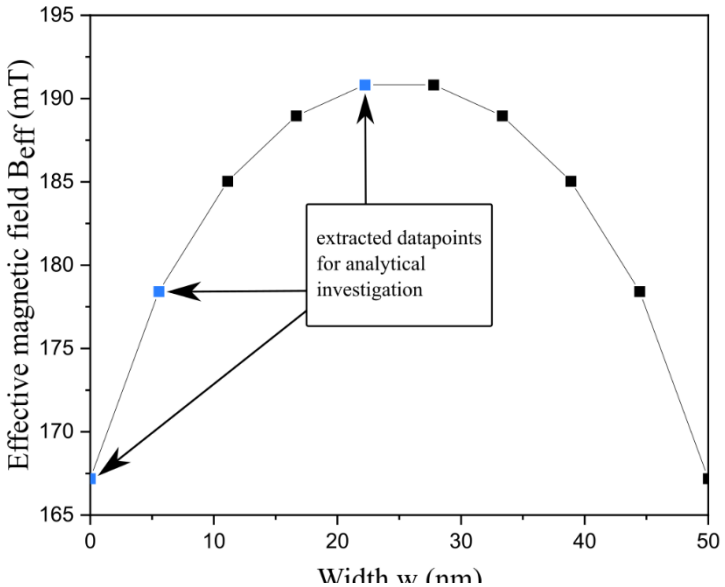

Figure 16: **Extracted data points for analytical investigation.** The three depicted spots (light blue) show the points of interest for the analytical analysis of spin-wave properties in a nano-scaled YIG waveguide. They were chosen as a depiction of the internal effective magnetic field along the width of a 44 nm wide waveguide to show the spin-wave propagation in Damon-Eshbach geometry for different distances to the edge of the waveguide.

Three different points of the internal magnetic field along the width of the simulated nanostructured waveguide have been chosen to compute the dispersion relation in the material with preexisting analyzation methods. The extracted data points of the internal magnetic field in a nanostructured YIG waveguide can be seen in Figure 16. Moreover, the program calculates the group velocity and plots it also against the wavenumber of the Damon-Eshbach spin waves.

The lifetime of the spin waves in this geometry and the propagation length, shown as the possible distance travelled in the medium in micrometer, are plotted additionally against the wavenumber of the spin waves for three different values of the effective magnetic field inside the waveguide.

As can be seen in subsection 4.1, the value of the internal magnetic field is changing permanently along the width of the nano-structured waveguide.

Therefore, the conditions for propagation of the spin waves change for different regions perpendicular to the propagation direction, which results in different dispersion curves for the spin waves depending on the effective magnetic field where dispersion takes place.

In Figure 17, the dispersion relation for three different magnitudes of the internal magnetic field in a YIG waveguide shows the dependence on the location of the spin wave in the material. Although the dispersion relation looks similar for all three points of interest, the group velocity of the spin waves in Damon-Eshbach geometry and the travelled distance in the material near the edge of a 44 nm waveguide differ for wavenumbers close to zero. Figure 17 shows that the difference between spin waves which travel near the edges of the waveguide (a) and b)) and those which propagate in the middle thereof (e) and f)) is significant: Spin waves can propagate when having a higher frequency in the middle of the waveguide, which also results in a higher group velocity, whereas spin waves near the edges have a higher lifetime.

It shall be noted that the theory in this analysis supports waveguides above a width of 500 nm as no analytical formula exists for the nano-structures used in this thesis. Consequently, this thesis shall compare the results of the existing analytical calculations with micromagnetic simulations in the following subchapter.

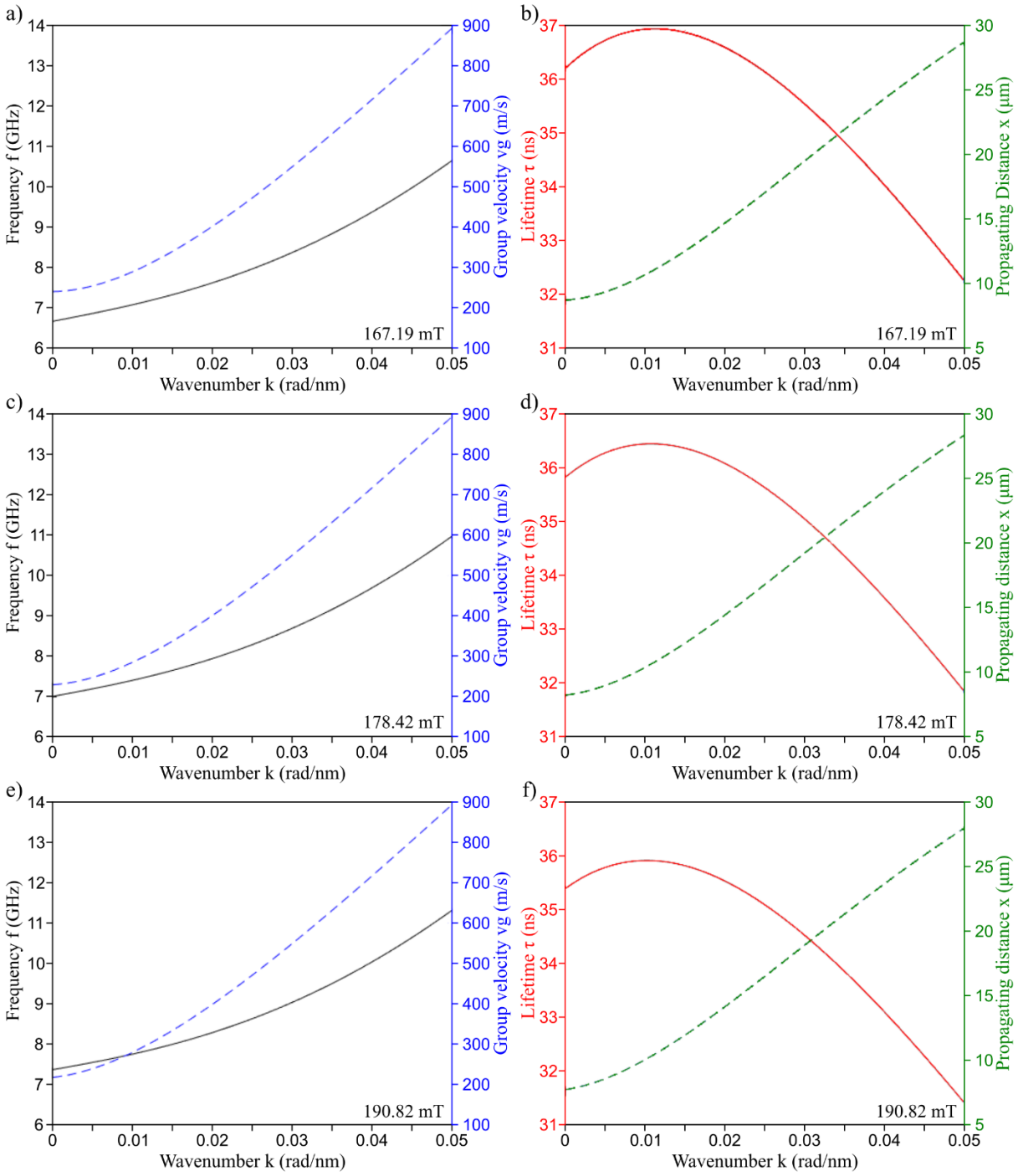

Figure 17: **Classical analysis of dispersion properties.** The different graphs show on the left side the dispersion relation (frequency versus wavenumber, in black) and the dependence of the group velocity (in blue, dashed) on the wavenumber and on the right side the expected lifetime (in red) and propagation length (in green, dashed) of the spin waves in Damon-Eshbach geometry in a nanostructured YIG material for three different points of interest of the internal magnetic field a)and b) 167.19 mT, c) and d) 178.42 mT and e) and f) 190.82 mT) as shown in Figure 16. The graphs show varying behaviors for the listed properties depending on the effective magnetic field inside the waveguide

4.4. Comparison of analytical results with numerical simulations results

Analytical ways to calculate the dispersion relations of Damon-Eshbach spin waves in a waveguide smaller than 500 nm do not exist. This chapter compares the approximations of the previous chapter to the simulations to show not only differences in the value of the frequency, but also in the curve of the depicted graph. As the used waveguide in this thesis is far below the µm range, a comparison of the previously calculated dispersion curve with the dispersion in the micromagnetic simulation of spin waves in Damon-Eshbach geometry depicts the deviation of the analytical results and the simulated results for nanostructures.

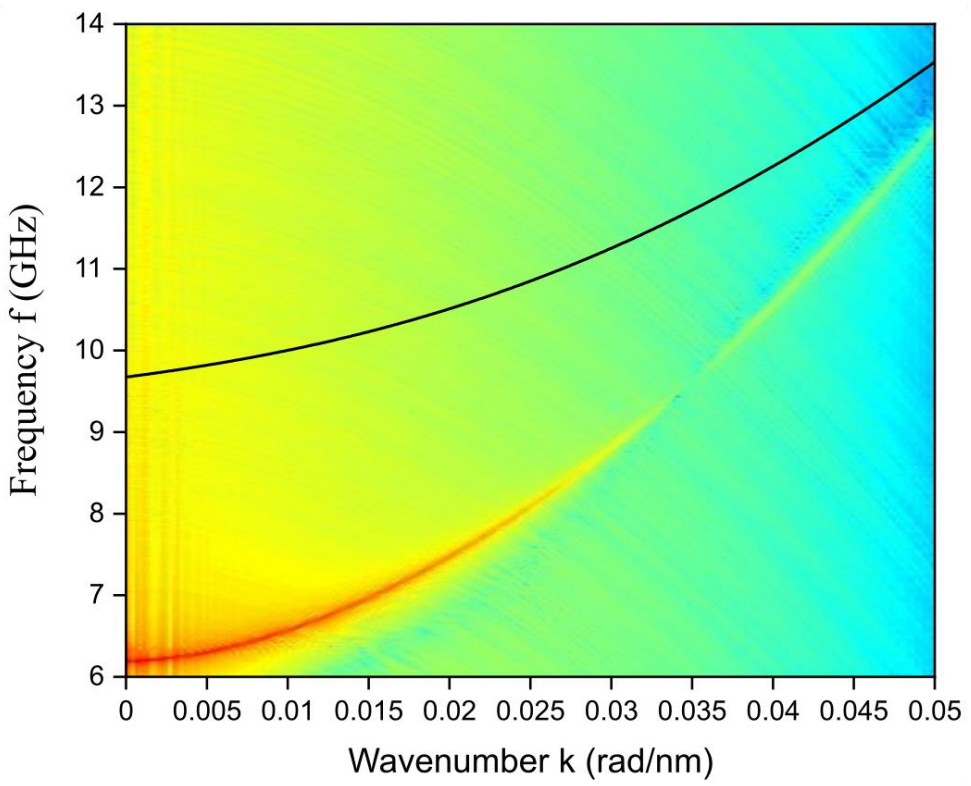

Figure 18: **Comparison of the simulated dispersion curve and the results of the analytical calculation.** The figure shows the frequency (in GHz) of spin waves in a YIG waveguide where a magnetic field is applied in plane of, but perpendicular to the propagation direction. The simulated dispersion curve is displayed in color, with red having a high intensity of the propagating mode (blue being a low intensity), whereas the analytical calculation is shown in a black line on top. The parameters used for the analytical calculations are the saturation magnetization $M_{sat} = 1.45 \cdot 10^5 \frac{A}{m}$, the exchange constant, $A_{ex} = 4.5 \cdot 10^{-12} \frac{J}{m}$ and the Gilbert damping constant $\alpha = 2 \cdot 10^{-4}$. The micromagnetic simulations used the same parameters for a size of the mesh cells of 10 nm × 10 nm × 44 nm. Both results were obtained when using an external applied magnetic field of 200 mT.

Figure 18 shows the discrepancy of both calculation methods for nanostructures. The calculated dispersion curve from the simulation of propagating spin waves as well as the analytical calculation show parabolic behavior. However, a rather large energy difference of a few GHz lies between both results at a low spin-wave wavenumber. At higher wavenumbers, the energy difference seems to become smaller as the analytical solution does not increase as much as the simulated result in a nanostructured waveguide. This rather large discrepancy in the energy of Damon-Eshbach spin waves shows that a further understanding of the spin-wave propagation in nanostructured waveguides is needed to improve the analytical calculations thereof.

5. Experimental studies of spin-wave propagation in nano-scaled waveguides in Damon-Eshbach geometry

In the following chapter a BLS (Brillouin Light Scattering) microscope is used to probe the magnetization dynamics in a nanostructured YIG waveguide via an inelastic scattering process of photons with the fundamental excitations of a solid, meaning that energy is conserved in this setup. The investigated material in this thesis is an Yttrium-Iron-Garnet waveguide in which the propagating spin waves have been examined in Damon-Eshbach geometry. A μBLS pushes the fundamental limit of classical optics in regards of spatial resolution and therefore can sufficiently examine thin magnetic films of 100 nm size and below, such as the YIG waveguide used in this thesis. The group velocity of spin waves travelling perpendicular to the direction of the applied external field is higher than for a backward volume spin-wave geometry in a microstructure. Little is known about the dispersion of magnetostatic surface spin waves in a YIG nanostructure due to the complex internal magnetic field of the waveguide. This chapter gives proof for the existence and propagation of spin waves in Damon-Eshbach geometry in a nanostructured YIG sample.

The YIG waveguide was installed in the μBLS in such a way that the externally applied magnetic field was perpendicular to and in-plane of the propagation direction of the spin waves. After aligning the laser beam perfectly onto the sample and the detector, the measurements were done with the help of the thaTEC:OS program [58] which connects all needed programs for simplification and automatization of the measurement: The magnetic field, the current running through the antenna, a stabilization program for the camera and the detector can all be regulated by the program. Moreover, the company also offers a program for visualization of the recorded data in the measurement. The results in this chapter were obtained by using the DataInspector of thaTEC:OS and further analysis in Origin. The measurements were performed on a 1000 nm wide and a 44 nm wide waveguide.

This chapter focuses on the results obtained by the BLS microscope. A 1000 nm wide waveguide is studied to allow a comparison under the same conditions for micrometer sized YIG waveguides which were already examined by former scientists for the past decades.

The spin-wave propagation characteristics in a nanostructured waveguide were studied under two separate conditions - with continuous wave (CW) and pulsed excitation - which build the following two subchapters.

The last part of this chapter investigates the decay of the spin wave in Damon-Eshbach geometry under continuous excitation in a nano-scaled YIG waveguide. In doing so, the non-reciprocity of spin waves in Damon-Eshbach geometry is studied. Furthermore, this chapter gives an estimation about the decay length in a nanostructured YIG waveguide.

5.1. Spin-wave spectrum in a micro-structured (1000 nm wide) waveguide

This part of the thesis aims to show the difference for nano-scaled YIG waveguides and the magnetostatic surface spin-wave propagation therein. Therefore, this chapter offers a measurement for the 1000 nm wide waveguide in the style of the already discussed experiments of continuous excitation. The microstructured waveguide can be seen in Figure 19 as a grey line across the sample structure. The external magnetic field surrounding the sample has a value of nearly 270 mT, and the mirror spacing inside the Fabry-Pérot interferometers was set to 7 mm. The spin waves in the 1 µm wide YIG waveguide were excited by the a microwave signal generator with a microwave signal power of -10 dBm.

The spectrum counts show a peak in intensity (in Figure 20) at a much higher microwave frequency of the applied signal. The fundamental mode of a micrometer sized waveguide needs a high frequency of the applied microwave input signal to appear. Furthermore, the BLS frequency is higher for the first appearance of the mode. However, a drag of the fundamental mode is evident in Figure 21. Higher magnon-scattering processes may be the reason for the smearing of the mode.

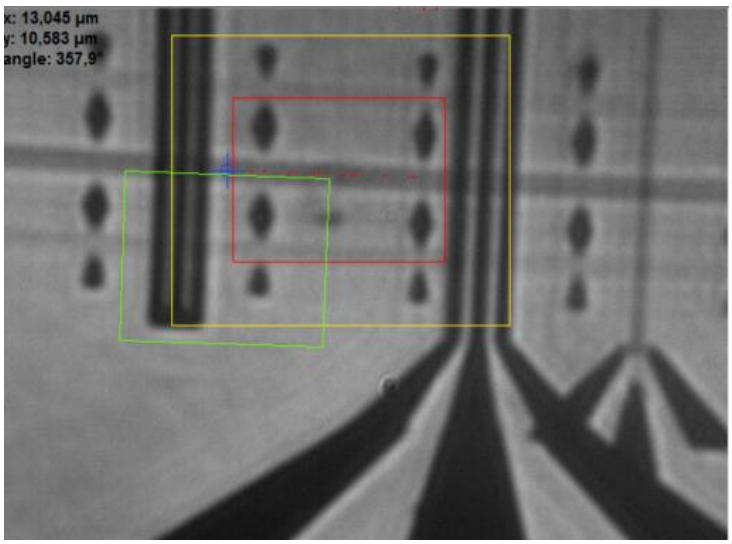

Figure 19: **Scanning position.** The image shows a 1 µm wide waveguide surrounded by diamond shapes. A blue crosshair shows the point where the BLS laser hits the sample. A red rectangle defines stabilization; a yellow one leaves room for retraction. The antenna is shown as thick dark lines perpendicular to the light grey waveguide.

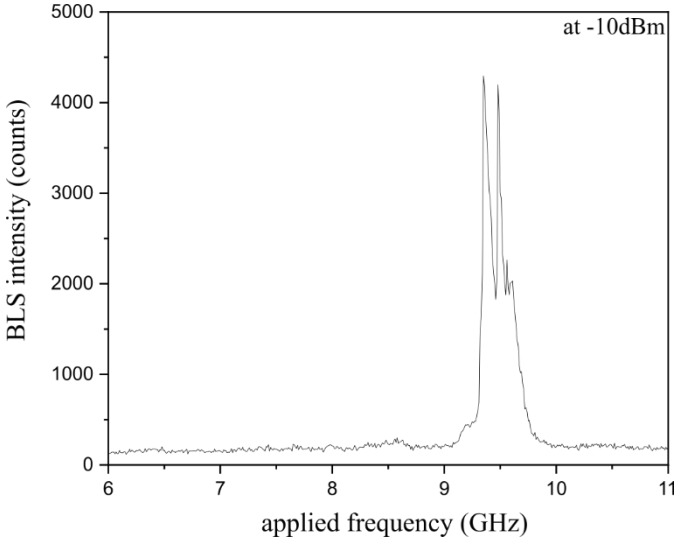

Figure 20: **BLS intensity dependent on the frequency of the applied signal.** A high accumulation of the inelastically scattered photons can be observed at a higher frequency of the applied microwave signal than in a YIG nanostructure.

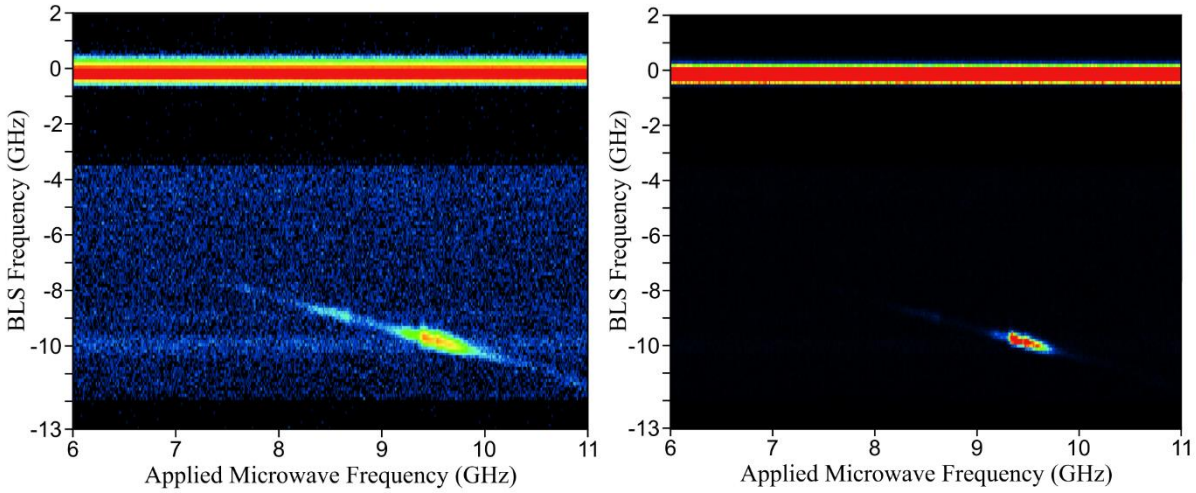

Figure 21: **Applied frequency versus BLS frequency.** Both images show the intensity of the BLS frequency depending on the frequency of the applied microwave signal (in GHz). The left image shows a logarithmic scaling of the spectrum counts. A red color displays a higher intensity than a blue or black shading in the plot.

5.2. Spin-wave spectra of nano-structured (44 nm wide) YIG waveguide

The different forms of excitation – continuous wave or pulsed – can form different dynamic magnetic fields which affect the spin wave in different ways. It also allows the linear and non-linear dispersion properties of the waveguide to be studied [17]. This chapter aims to show the different spectra obtained by continuous and pulsed excitation of the spin waves in Damon-Eshbach geometry in a nano-scaled YIG film with a width of 44 nm.

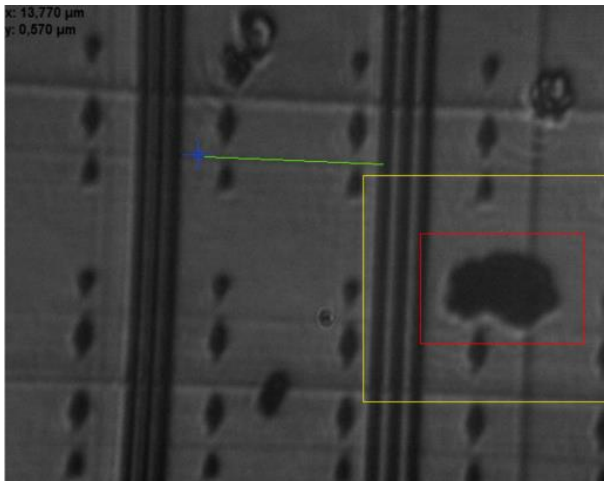

Figure 22: **Scan position.** This image of the Microscopy Module shows the chosen scanning position at the blue cross. The red rectangle defines a distinct shape to stabilize the frame; the yellow rectangle defines a room for maneuver. Markers in the shape of diamonds surround the waveguides. Three dark lines state the location of the antenna, which is located perpendicular to the waveguide.

The nanostructured YIG waveguide is installed in the BLS microscope in such a way that the propagation of magnetostatic surface spin waves is possible after possible needed alignments of the BLS setup. Using a line-scan, which scans the reflections of the laser beam and the light of the camera on (at best) two edges of a high contrast structure (such as indentations or contaminations), these reflections are recorded and, if needed, the sample is shifted to have the reflections at the same recorded position. The sample including the antenna and the waveguide can be seen in Figure 22. With the microscope, the beam of the investigating laser is then focused onto a spot on the waveguide near the antenna, approximately 1 µm away. A distinct shape on the sample is used for stabilization thereof during the measurement using the autofocus function of the camera and a corresponding shift of the piezo-elements on the translation stage. A microwave signal generator is put into contact and the current is set for the antenna. Furthermore, a mirror spacing of the Fabry-Pérot interferometers is set. For this experiment, this distance of the mirrors is set to be $d = 10\,\mathrm{mm}$. This can be changed during the measurement, if needed. Moreover, the magnetic field needs to be switched on during measurements.

The Tandem Fabry-Pérot data acquisition software version 5 (TFPDAS5) program (Figure 23) is used to check the signals in reflection and transmission mode. The display shows a plot of the BLS-spectrum, plotting the BLS-frequency against the number of photon-counts in the detector.

While aligning the etalon mirrors, the screen of this program should show two dips in reflection mode. These dips signal an alignment of the interferometer mirrors when both dips are overlapping and maximized. The signal should show only one transmission peak in transmission mode. After allowing the program to turn on the active stabilization routine, the system will automatically optimize and stabilize the interferometer using the Finesse Optimizer (FO), a Drift Stabilizer and a Dynamic Dither for a maximal signal in transmission. The FO signal gives the area under the reference peak as a measure for parallel mirrors and how synchronal both etalons are. The Drift Stabilizer keeps the reference signal centered at 0 GHz, which corresponds to the frequency of the photons with the wavelength of the laser. Negative frequencies correspond to the event where magnons are created (Stokes spectrum), whereas photons with positive frequencies show magnon annihilation (Anti-Stokes spectrum) due to photon-magnon interactions. The piezo voltages of the mirror tilt and spacing can be varied by the Dynamic Dither to ensure a stable signal for disturbances of different magnitude [59]. During the measurement, an accumulation of photons in a range different to the reference peak can be observed. Prior to the measurement, the different Scan Parameters need to be set.

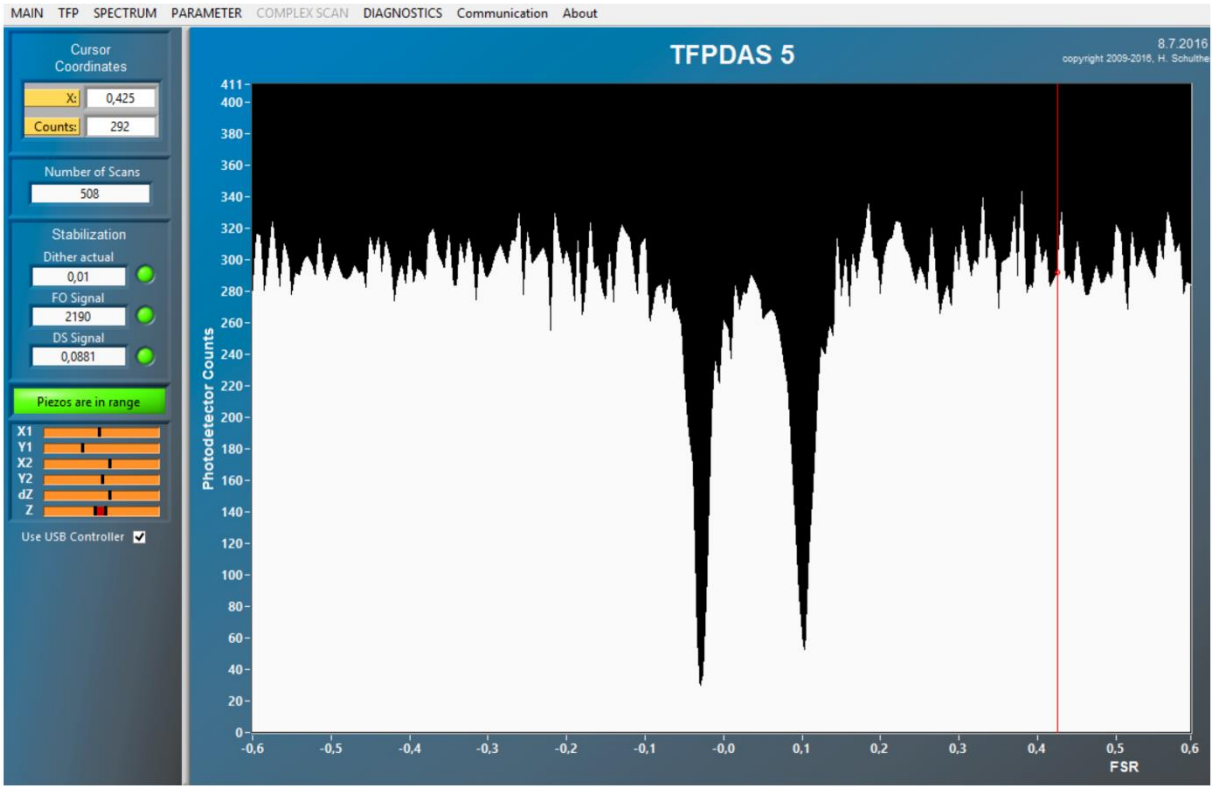

Figure 23: **Screenshot of the TFPDAS5 window.** The screen shows an exemplary signal in reflection mode before perfect adjustment of the etalons in the TFP-interferometer. Retrieved from [60].

The number of scans can be set to 0 for an infinite scanning period, while a minimal measurement should have at least 12 scans to cycle through each stabilization parameters (the piezo-voltages of the piezo-electric actuators controlling the mirror tilt and the mirror spacing interferometers) twice.

An increasing number of scans improves the sensitivity of the measurement (meaning the signal-to-noise ratio) by accumulating the signal of the arriving photons. A region of interest (ROI) defines a frequency range where inelastically scattered light is expected. Before the start of the measurement, the program for the measurement needs to be written in the thaTEC:OS software. A nice signal in the spectrum window, which is staying at the 0 GHz position, is a good start for a stable measurement.

5.2.1. Spectrum obtained with a continuous wave excitation

The continuous excitation of Damon Eshbach spin waves in a YIG waveguide is done by a microwave signal generator (Agilent E8257D), connected to the antenna on top of the material. The power of the generated signal can be adjusted for a single measurement; and a scaling of the power during the measurement can be done via an implementation in the thaTEC:OS program. Different powers of the signal generator give different intensities of the measured BLS-intensity, where a higher power leads to a higher intensity.

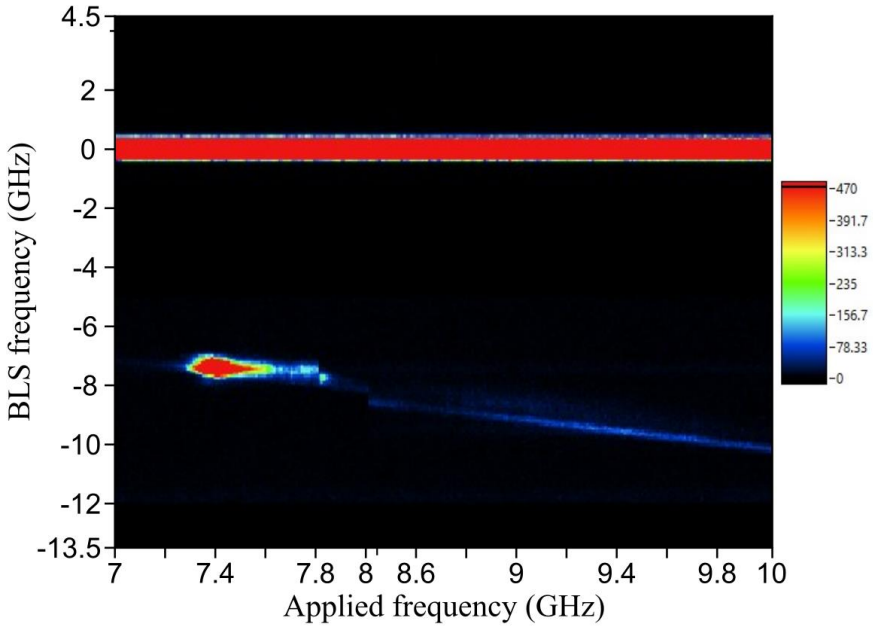

Figure 24: **Microwave frequency versus BLS frequency.** The plot shows the generated signal with a 15 dBm microwave frequency against the BLS frequency with non- logarithmic spectrum counts for a measurement in the µ-BLS. The scale indicates the intensity of the measured frequencies in a color code.

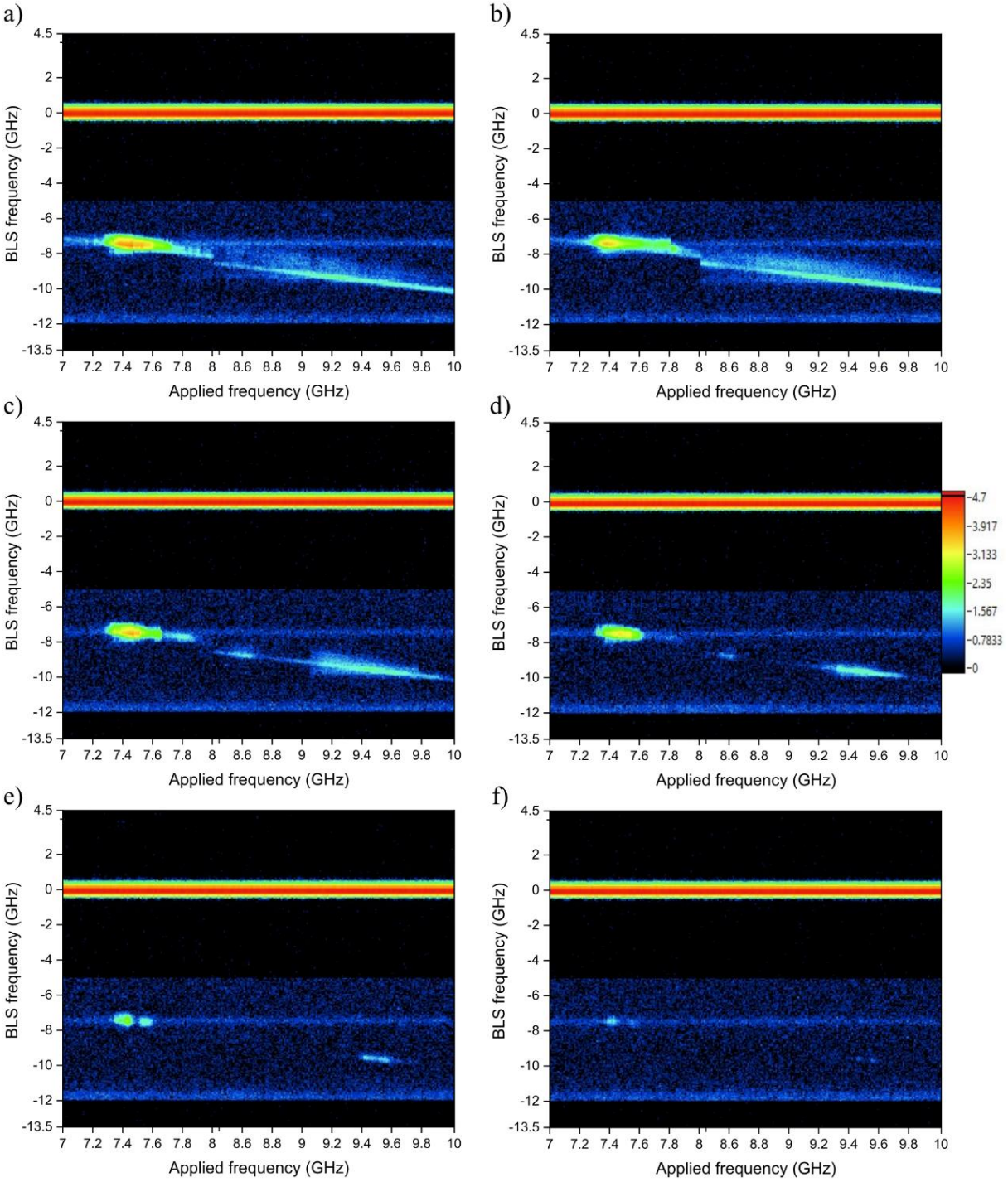

Figure 25: **Applied microwave frequency versus BLS frequency.** The applied signal frequency from the Agilent signal generator is plotted against the measured frequency of the BLS for different configurations of the power setting: a) 25 dBm, b) 15 dBm, c) 5 dBm, d) - 5 dBm, e) -15 dBm and f) -25 dBm. The colors give the spectrum counts of the measurement in a logarithmic scale for a maximum value of 4.7.

In Figure 25, a high intensity strip at 0 GHz can be seen which shows the frequency of the reference beam. The high intensity spots on the left side of the plots shows the fundamental mode. The linear intensity strip around a BLS frequency of 7.5 GHz shows the thermal mode.

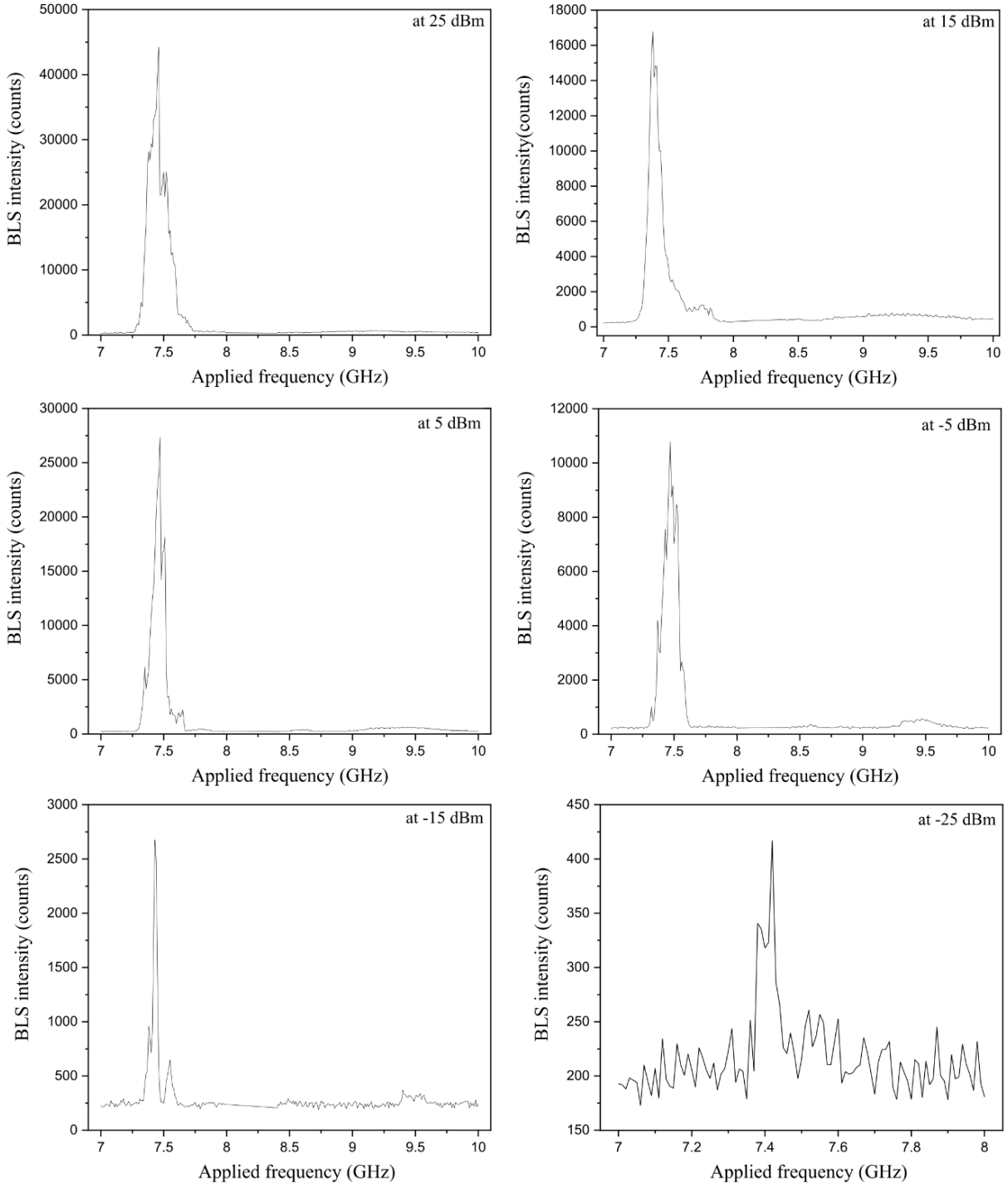

Figure 26: **BLS intensity as a function of the applied microwave frequency for a) 25 dBm, b) 15 dBm, c) 5 dBm, d) -5 dBm, e) -15 dBm and f) -25 dBm.** The externally applied magnetic field surrounding the sample has an intensity of $H = 270\ mT$.

Data processed using Origin [61].

The drag of the intensity of fundamental mode could suggest a possible 4-magnon scattering process, which drags the mode over the whole frequency range. The jump in the plot is due to jumping frequency values of a second region of interest.

Directly retrieved from the measurement (Figure 24 and Figure 25), the first results show the frequency of the BLS versus the applied microwave frequency of the signal generator. The power dependent-sweeps were performed using the Brillouin-Light-Scattering microscope. The generated signals in the continuous excitation measurement were sent through the system within a range of -25 dBm to +25 dBm (where 1 dBm stands for a decibel with reference to one Milliwatt).

Figure 25 and Figure 26 show the performed measurements in plots for different applied continuous signal power. As stated before, a higher power of the signal leads to a higher intensity in spectrum counts for the different modes, which can easily be seen in the intensity of the modes in Figure 26.

The fundamental mode can be seen in all different plots, which states the existence is not depending on the power of the applied signal, merely the intensity thereof is conditional on the generated power.

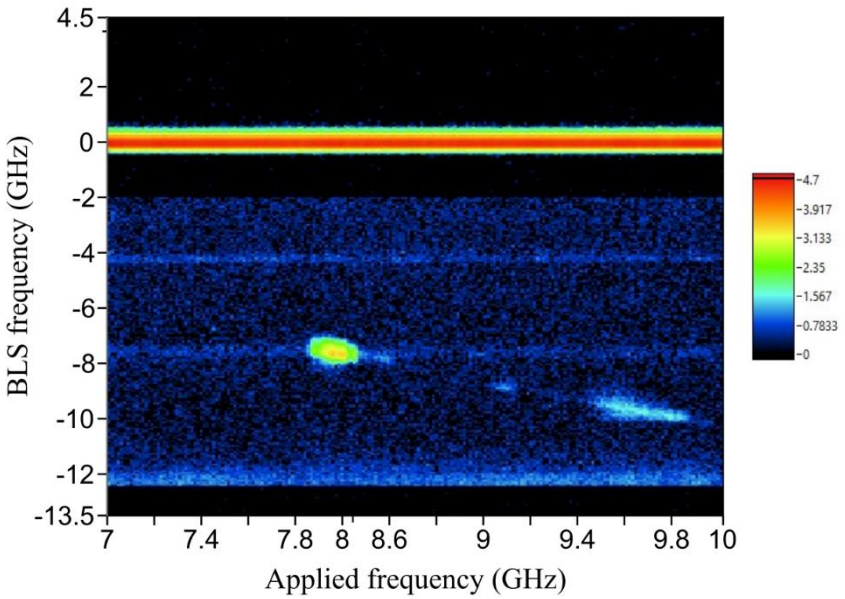

Figure 27: **BLS frequency as a function of the applied microwave frequency with 0 dBm.** The figure shows the additional laser mode at a frequency of 4 GHz, the thermal mode near the 8 GHz frequency as well as the fundamental modes (bright spot) with the spectrum counts displayed by different colors. The scale depicts the intensity of the measured frequency difference via a color code.

In Figure 25 and Figure 27, it can be seen that the fundamental mode is smeared across the frequency range due to a possible 4-magnon scattering process at higher powers of the generated microwave signal. Possible thickness modes can be eliminated as these would be located at a much higher frequency range for the existing settings of the measurement. The thermal mode can be observed as a straight line near the 8 GHz frequency. At the lower part of the recorded spectrum counts, near the 12 GHz frequency, the next transmission mode can be seen. The laser mode can be observed and is shown as a linear intensity strip at a frequency of 4 GHz.

The plots in Figure 26 show the BLS intensity as a function of the applied microwave frequency depending on the power of the generated signal. Each plot shows a maximum of the propagating Damon-Eshbach spin waves for an applied frequency of about 7.4 GHz, with a secondary peak following for higher applied frequencies. The last plot, for the lowest power, shows a drastic decrease in the counted photons for all frequency ranges.

5.2.2. Spectrum obtained with pulsed excitation

Pulsed excitation is achieved by connecting a Miteq pin switch to the signal generator to get a more distinct signal in a non-linear excitation system.

A Keysight 81150A generator supplies the pulsed signals to the system with a pulse duration of 30 ns and a delay of 280 ns in between the pulses, which was automatically performed with the help of a script that has been put into the thaTEC:OS software.

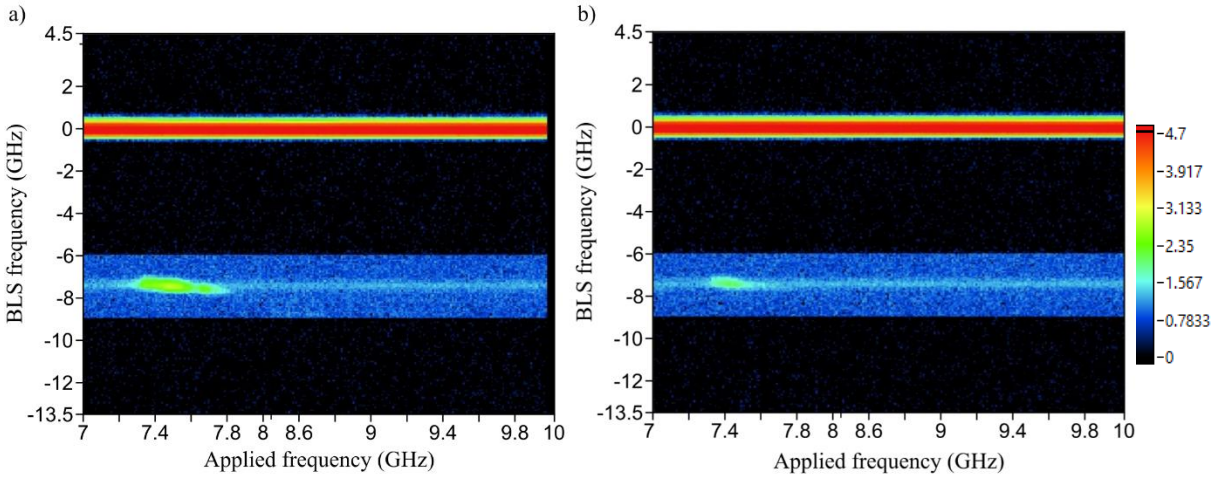

Figure 28: **Applied microwave frequency versus the BLS frequency.** The plot shows the spectrum counts for different applied frequency signals with a short excitation pulse for a) 10 dBm and b) 0 dBm power. The x-axis displays the number of steps in the range of 7.8 GHz to 8,4 GHz in 10 MHz steps. The colors indicate the intensity of the measured signals.

The microwave input pulses allow a short excitation spin waves to study the behavior of spin waves in Damon-Eshbach geometry under small non-linearities in this thesis.

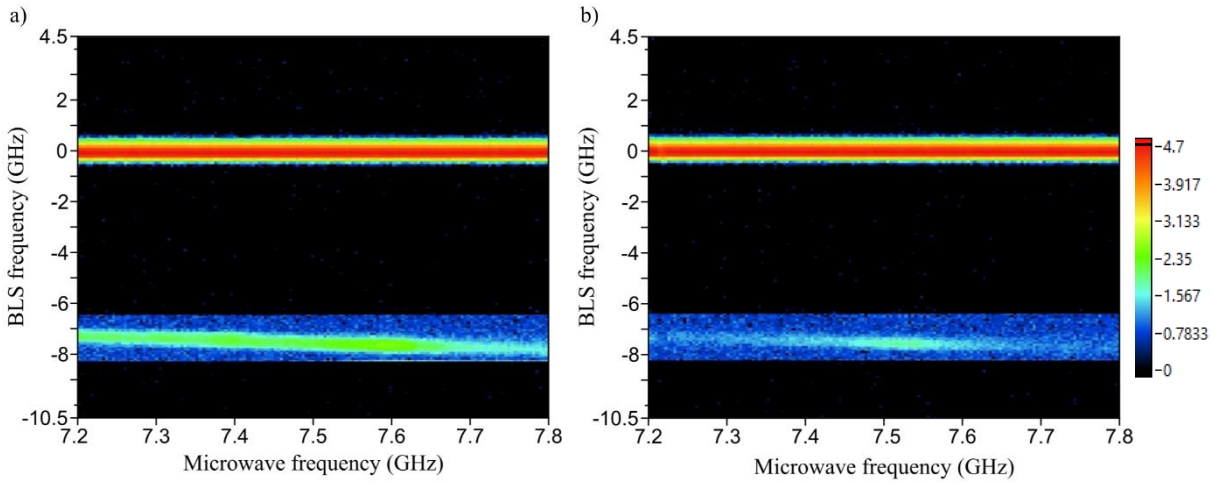

Figure 29: **Applied microwave frequency versus BLS frequency.** The plot shows the spectrum counts for a) +5 dBm and b) -5 dBm power frequency signals.

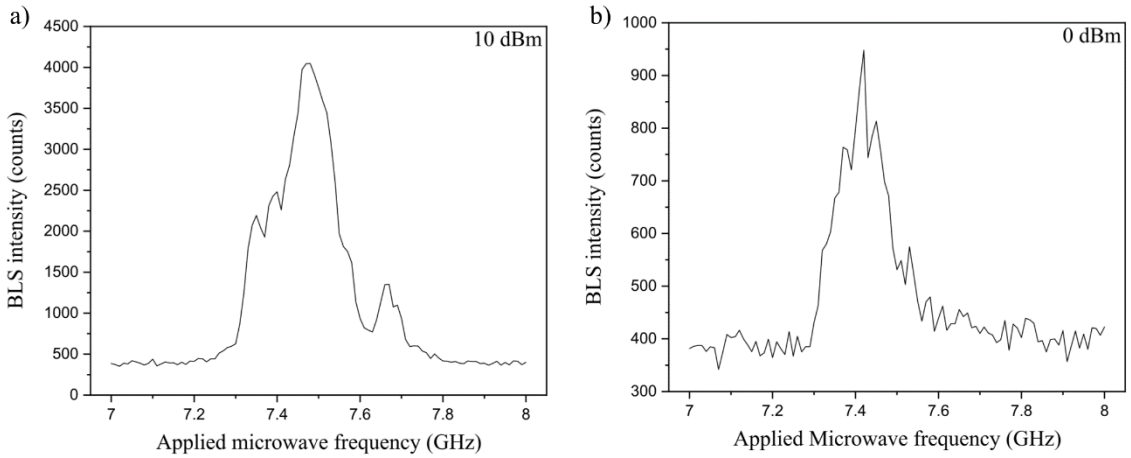

Figure 30: **BLS intensity as a function of the applied frequency.** The accumulated counts over 96 scans are shown as a function of the applied frequency signal with a power of a) 10 dBm and b) 0 dBm in steps of 10 MHz.

Due to problems in the BLS setup, the measurements of the pulsed spectrum were harder to perform and could only be done with a high power of the generated frequency signal. However, the measurements shown in Figure 28 and Figure 30 show the relation of high power applied microwave frequency signals and the BLS frequency and intensity of the spectrum counts.

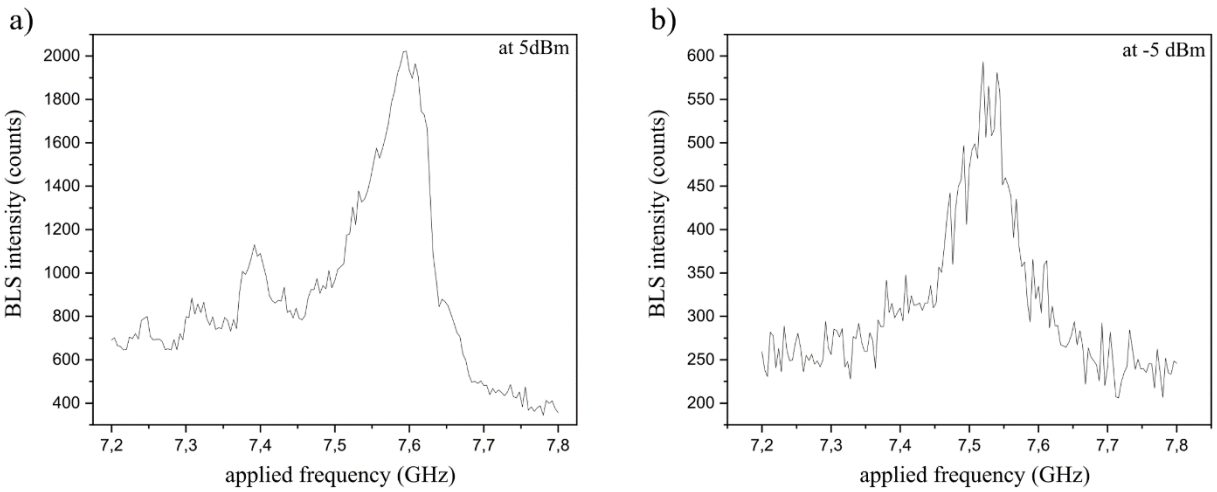

Figure 31: **BLS intensity as a function of the frequency of the applied signal generator.** The counts were accumulated and plotted against the applied signal with a power of a) 5dBm and b) -5 dBm in steps of 4 MHz.

Figure 29 and Figure 31 show a reduction in the number of the photon counts for a decreasing power of the applied microwave frequency signals. Moreover, the peak of the distribution is shifted for signals with different powers. This could stem from the worsening state of the BLS, but it could also originate from the non-linearities introduced through the pulsed excitation. The measurements for signal powers below -5 dBm had problems relating to the noise signals. A further investigation after a new alignment of the BLS setup was not possible due to lack of time. However, the existing research at higher powers as well as the aforementioned experiments using a continuous excitation led to believe that the trend of lower intensity would continue for signals with lower power. Furthermore, the trend of the shifting peak of the accumulated counts for the fundamental mode near 7.5 GHz the BLS intensity plot would continue, provided this indication was not created by the BLS setup. The finding of just one fundamental propagating mode supports the single-mode dispersion of the micromagnetic simulations.

5.3. Measurements of spin-wave decay length in a nano-structured (44 nm wide) YIG waveguide

As stated in the theoretical background, magnetostatic surface spin waves are not distributed periodically through the film thickness. This chapter shows that the intensity decay of spin waves in Damon-Eshbach geometry in nano-scaled YIG waveguides behaves in an exponentially decaying way. Moreover, the decay length shall be investigated with two magnetic fields which have opposite sign in the nanostructure. Figure 32 shows the scanned path along the nanostructured YIG waveguide.

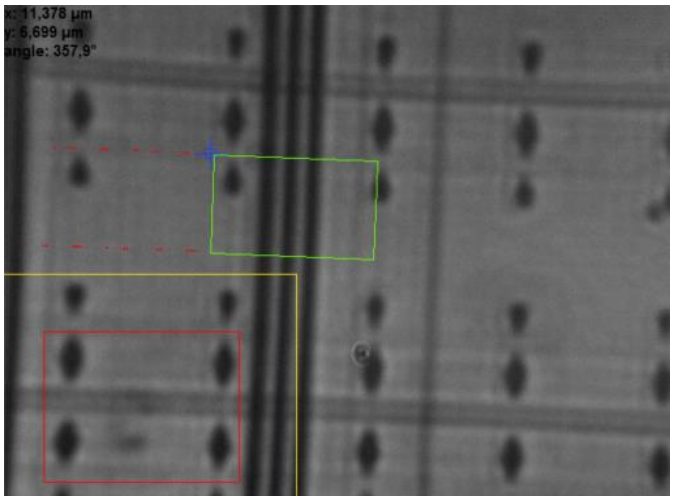

Figure 32: **Scanned path.** The upper red dotted line shows the chosen path along the YIG waveguide. The relation of the blue crosshair to the initial scanning point has moved to the point of the last measurement position (after 50 steps) due to the piezo-elements shifting the sample table.

The values of applied frequency at which the decay measurements were performed were chosen due to them being interesting points in the experiments for continuous wave at -5 dBm (see chapter 5.2.1), where either a higher peak or a local minimum is visible in the BLS frequency graph as a function of the frequency of the applied microwave input signal. The µBLS allows a spatial scanning along a predefined direction using the Microscopy Module to mark the pathway. The sample is then moved due to the piezo-elements on the translation stage during the experiment by an automatic movement according to the written thaTEC:OS program. The results of this measurement are given as plots of the BLS frequency against the position of the laser moving along the waveguide.

Figure 33 and Figure 34 show the intensity of the spin wave for different frequencies of applied input signals as a dependence on the distance to the antenna which continuously excites the waveguide, as well as for different directions of the external magnetic field. The amount of the counted photons decreases drastically with an increasing distance to the antenna in both cases.

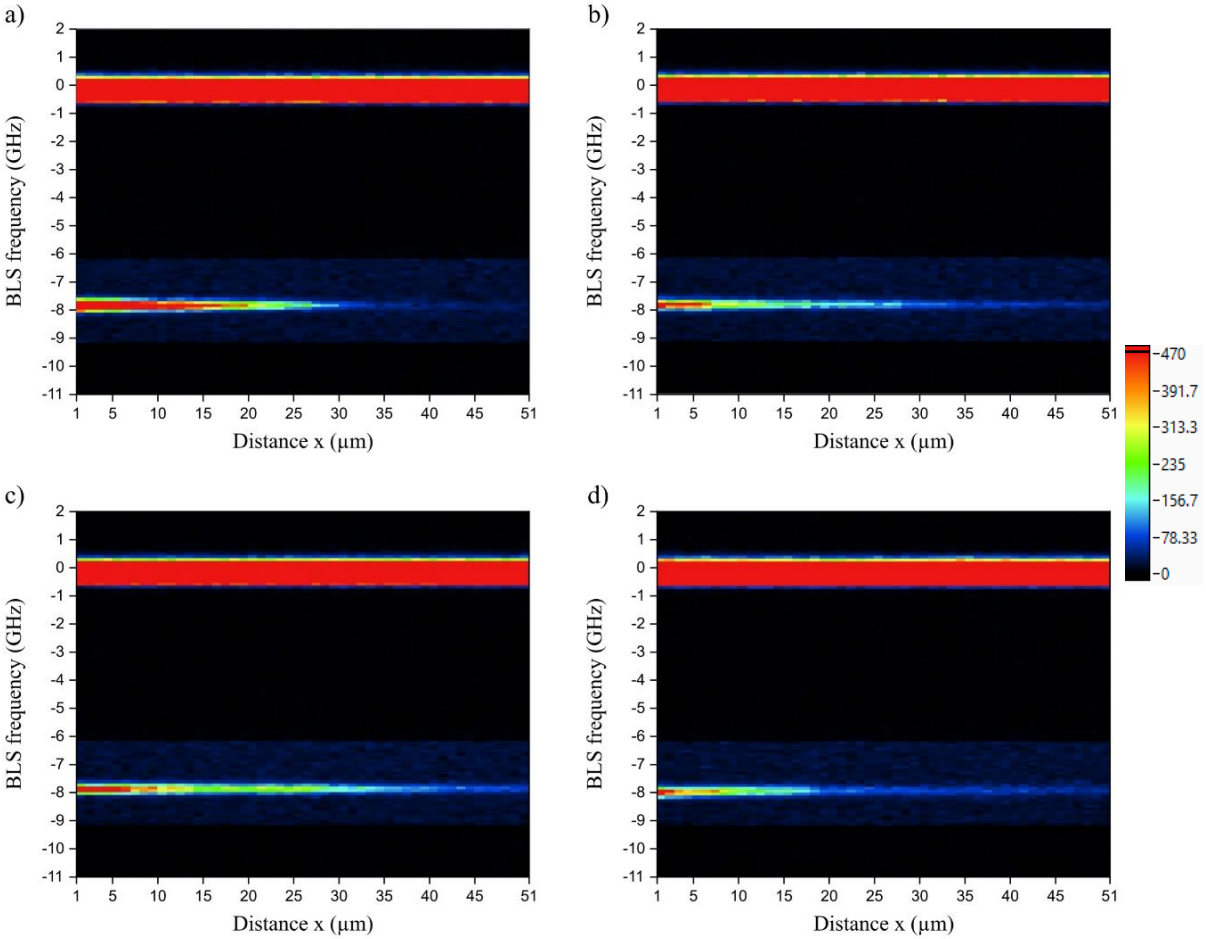

Figure 33: **BLS frequency as a function of the scan position.** The detected photons for each frequency are counted and displayed in a color intensity scale depending on the distance to the antenna for different microwave input signal frequencies (a) 7.414 GHz, b)7.428 GHz, c) 7.468 GHZ and d) 7.572 GHz) for an external magnetic field of 270 mT.

Different applied frequency signals correspond to a differently high BLS intensity in a measurement of continuous wave excitation, i.e. the plots in Figure 33 a) and c) correspond to the high peaks in the -5 dBm result in subchapter 5.2.1, whereas b) and d) show points with a smaller BLS intensity.

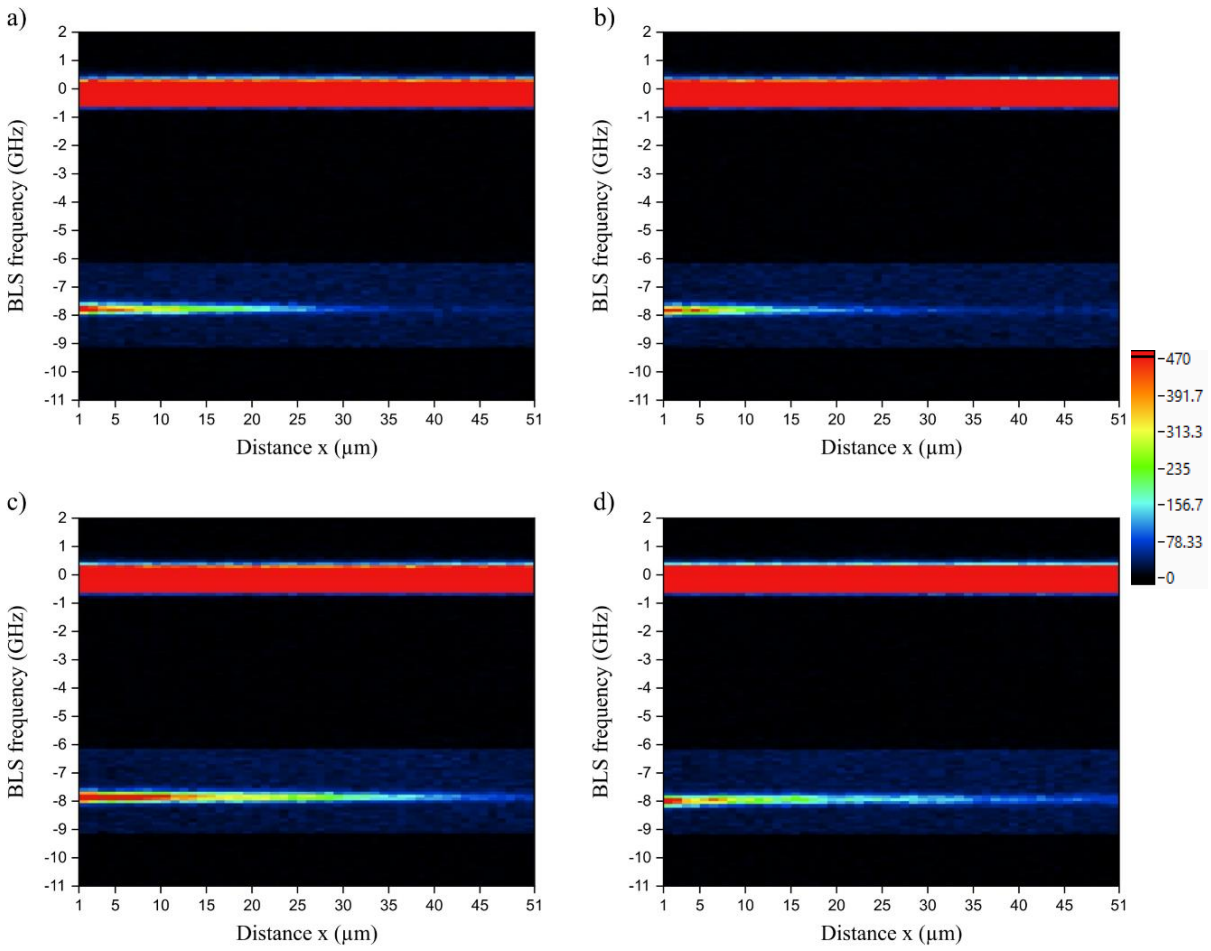

*Figure 34:***BLS frequency versus scanning position.** The counted photons are displayed by color for increasing amount. The distance from the antenna on the x-axis in steps taken for different applied microwave input signal frequencies (a) 7.408 GHz, b) 7.456 GHz, c)7.504 GHz and d) 7.592 GHz) is plotted for an external magnetic field of -270 mT.

Measurements for the same applied frequency signal at external magnetic field application of opposite signs show that in the setup with a positive magnetic field (Figure 35 b)) the spin wave has a higher initial BLS intensity but decreases faster. The discrepancy between the photon count with positive magnetic field and the BLS intensity of the setup with the opposite applied magnetic field show signs of non-reciprocity for a reversal.

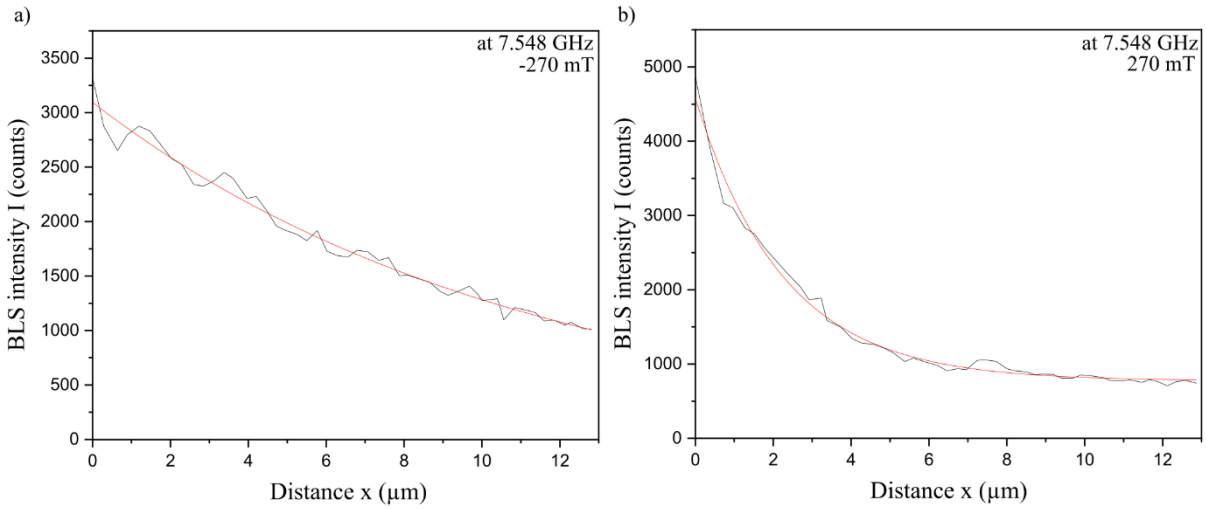

Figure 35: **BLS intensity plotted against distance from the antenna for different applied external magnetic field** a) **-270 mT and** b) **+270 mT.** The detected intensity of the spin wave for an applied frequency signal of 7.548 GHz decreases exponentially for a distance from the antenna given in µm as shown for two externally applied magnetic fields with opposite signs. An additional exponentially decaying fit (shown in red) is plotted to determine the intensity decay length of the magnetostatic surface spin wave in the nanostructured YIG waveguide.

Figure 35 a) and b) additionally include an exponentially decaying fit function to determine the decay length l_d of the magnetostatic surface spin waves in a 44 nm wide YIG waveguide according to an exponential decay function of the intensity:

$$\mathrm{I(t)} = \mathrm{I_0} + \mathrm{I_1} \cdot \mathrm{e}^{-\frac{2x}{l_d}}. \tag{84}$$

The above function estimates the distance from the antenna where the spin-wave intensity drops to $1/e$ of the initial intensity I_0. The intensity decay length of magnetostatic surface spin waves in the 44 nm wide YIG waveguide for an externally applied magnetic field of 270 mT (shown in Figure 35b) is estimated using the exponentially decaying intensity fit function to be $l_{\mathrm{d},+} = 4.52\ \mu\mathrm{m}$. However, the spin-wave intensity reaches even farther for an applied magnetic field with an opposite sign $l_{\mathrm{d},-} = 22.10\ \mu\mathrm{m}$ which is estimated using the fit function (in red) in Figure 35 a). This proves the assumption right that Damon-Eshbach spin waves do propagate in nanostructured YIG waveguides. Plus, these spin waves can travel for long distances inside these waveguides. Further investigations of free path and nonreciprocal phenomena in YG nano-conduits were recently published in Ref. [2].

6. Conclusion and Outlook

The aim of this thesis was to give an understanding of the propagation of Damon-Eshbach spin waves in a nanostructured YIG waveguide. As the miniaturization for future technologies involving spin transport is a relatively new research field, little research has been done on the spin-wave dynamics in nanostructures and even less to study spin waves in a Yttrium-Iron-Garnet (YIG) waveguide, although this material has promising features, such as an extremely low damping factor as well as magnetic properties which can be controlled easily for fundamental study on spin-wave behavior and for future implementation in information technology [62]. A nanostructured waveguide with a width of 44 nm was investigated to show the spin-wave dispersion characteristics with the help of micromagnetic simulations as well as experimentally by using a µBLS microscope during the course of this thesis.

The results of the micromagnetic simulations in this thesis show that the internal magnetic field in a nanostructured YIG waveguide is constantly changing along the thickness of the material compared to a waveguide with a thickness in micrometer range where the internal magnetic field along a large part of the profile is non-changing. However, such a waveguide with a width in the nanometer range has a much lower internal magnetic field compared to a wider waveguide when applying the same external magnetic bias field and microwave signals through an antenna. This is due to the large influences of the demagnetization as a result of the restricted size of the waveguide. An intermediate width shows that the effects of the demagnetization do not suddenly appear, but continuously change the value as well as the decrease near the edges of the waveguide: A wider waveguide shows a stark decrease of the magnitude of the internal magnetic field very close to the sides of the waveguide, whereas the internal magnetic field inside a nanometer structure constantly changes with a less steep decrease near the edges. Additionally, the dispersion curves were calculated for waveguides with three different thicknesses starting from a nanostructured one, showing that its waveguide has a smaller number of fundamental modes possible due to the smaller thickness, whereas a 1 µm thick waveguide shows a lot more fundamental spin-wave modes in the same frequency range. A single-mode dispersion relationship is found for a waveguide with a width of 44 nm in contrast to wider waveguides. For further analysis, preexisting analytics have been used to show different dispersion properties of Damon-Eshbach spin waves in a nanostructured YIG waveguide. However, as these analytics were modeled for microstructures, some differences in the behavior of the dispersion curve can be found when comparing the results to the numerically simulated dispersion curve. A large difference in the possible spin-wave propagation frequency

of a few GHz is found between the numerically simulated and analytically calculated dispersion curves. It is suggested that a further understanding of the spin-wave propagation and dispersion is needed to model new analytical calculations of the spin-wave behavior in nanostructures which depict the same results as the numerical simulation in a nanostructured waveguide.

The experimental results in this thesis were obtained using the µBLS microscope which uses the interaction of light and magnons to depict the frequency change of the inelastically scattered photons. This investigation tool was built in such a way that spin waves inside of nanostructures could be investigated. An experimental depiction of the continuous wave excitation spin-wave spectrum of a micrometer sized YIG waveguide is demonstrated to compare the spin waves in microstructures to those in nanostructures. The experimental results of the micrometer YIG waveguide shows the fundamental modes of Damon-Eshbach spin waves at high applied frequency signals. Spin-wave spectra in a 44 nm wide YIG waveguide were obtained by exciting the magnons in the waveguide with a continuous wave excitation as well as a pulsed excitation. The experimental studies of the spin-wave propagation in a nanostructured YIG waveguide in Damon-Eshbach geometry showed a difference in the frequency of the first appearance of the fundamental modes, where a higher applied microwave signal was needed for the wider waveguide. The spin-wave spectra of the nanostructure indicated a clear dependence of the BLS intensity on the power of the applied microwave signal with which the material was excited. Depictions of the BLS frequency, meaning the frequency difference of the photons in the initial laser beam and the inelastically scattered photons, depending on the applied microwave frequency demonstrated high intensity spots of the fundamental mode of the Damon-Eshbach spin waves in a nanostructured YIG waveguide. Applying a higher power of the microwave signal leads to a smearing of the fundamental spin-wave mode across the whole depicted frequency range. This could suggest a possible 4-magnon scattering process. A further investigation of the intensity decay of Damon-Eshbach spin waves in a nanostructure concluded that these waves do propagate quite far through the material. The decay measurement of the nanostructured YIG waveguide with a continuous wave excitation approved the expected exponential intensity decay of the Damon-Eshbach spin waves even in smaller than micrometer - sized structures. An estimation of the largest decay length of 22.10 µm is estimated for a fitting of the spin-wave BLS intensity in magnetostatic surface spin-wave geometry [2].

The non-reciprocity and especially the observed long decay length of Damon-Eshbach spin waves in a nanostructured YIG waveguide can be implemented in future applications in spin-wave devices to transport information over long distances. Finding an accurate solution for

analytical calculations of the dispersion curve as well as other interesting spin-wave characteristics would greatly enhance the investigation of properties before an actual production of magnonic crystals with nanoscale features which could be used for future data communication or other technologies. An investigation of another spin-wave geometry in a YIG waveguide as well as different impacts on the internal magnetic field of a nanostructured Yttrium-Iron-Garnet and other factors which could change the propagation dynamics of spin waves would be interesting, especially as this material will be used frequently in future information technology due to its many exciting features.

List of References

[1] Heinz, B., Brächer, T., Schneider, M. et al. "*Propagation of Spin-Wave Packets in Individual Nanosized Yttrium Iron Garnet Magnonic Conduits*". Nano Letters. 20.6: 4220-4227. doi: 10.1021/acs.nanolett.0c00657. (2020).

[2] Heinz, B., Wang, Q., Schneider, M. et al. "*Long-range spin wave propagation in transversely magnetized nano-scaled conduits*". Applied Physics Letters. 118: 132406. doi: 10.1063/5.0045570. (2021).

[3] Barman, A., Sinha, J. "*Spin Dynamics and Damping in Ferromagnetic Thin Films and Nanostructures*". Springer International Publishing. doi: 10.1007/978-3-319-66296-1. (2018).

[4] Wang, Q. "*Linear and Nonlinear Spin Waves in Nanoscale Magnonic Structures for Data Processing*". PhD Dissertation. Technical University Kaiserslautern. (2019).

[5] Prabhakar, A., Stancil, D. "*Spin waves – Theory and applications*". New York: Springer. doi: 10.1007/978-0-387-77865-5. (2009).

[6] Mahmoud, A., Ciubotaru, F. et al. "*Introduction to Spin-Wave Computing*". Journal of Applied Physics. 128.161101. doi: 10.1063/5.0019328. (2020).

[7] Vogt, K., Fradin, F. et al. "*Realization of a spin-wave multiplexer*". Nature Communications. 5.1: 3727. doi: 10.1038/ncomms4727. (2014).

[8] Fowler, M. *"Historical Beginnings of Theories of electricity and Magnetism*". Retrieved online from: http://galileoandeinstein.physics.virginia.edu/more_stuff/E&M_Hist.html.

[9] Chikazumi, S., Graham, C. "*Physics of Ferromagnetism*". Oxford, England: Clarendon Press. ISBN: 0198517769. (1997).

[10] Heinz, B. "*Herstellung und Untersuchung der Magnetisierungsdynamik in einzelnen Yttrium-Eisen-Granat Mikrostrukturen*". Master thesis. Technical University Kaiserslautern. (2016).

[11] Blügel, S., Hillebrands, B. '*5. Magnetismus*'. in "*Festkörper*". Edited by Kassing, R. Walter De Gruyter Inc. ISBN: 3110174855. (2005).

[12] Gilbert, T. "*A Phenomenological Theory of Damping in Ferromagnetic Materials*". IEEE Transactions on Magnetics. 40.6: 3443-3449. doi: 10.1109/TMAG.2004.836740. (2004).

[13] Gerlach, W., Stern, O. "*Der experimentelle Nachweis der Richtungsquantelung im Magnetfeld*". Zeitschrift für Physik. 9:349–352. doi: 10.1007/BF01326983. (1922).

[14] Turro, N. (1978). "*Modern molecular photochemistry*". Menlo Park, Calif: Benjamin/Cummings Pub. Co. doi: 10.1002/prac.19803220426. (2004).

[15] Obry, B. "*Design der Spinwellenpropagation durch eine magnetische Strukturierung ein- und zweidimensionaler Systeme*". PhD Dissertation, Technical University Kaiserslautern. (2013).

[16] Cullity, B., Graham, C. "*Introduction to Magnetic Materials (2nd edition)*". Wiley-IEEE Press. ISBN: 0471477419. (2008).

[17] Serga, A., Chumak, A., Hillebrands, B. "*YIG magnonics*". Journal of Physics D: Applied Physics, IOP Publishing Ltd. 43.264002. doi: 10.1088/0022-3727/43/26/264002. (2010).

[18] Kittel, C. "*Ferromagnetism*". Il Nuovo Cimento. 6, 895–922. doi: 10.1007/BF02834703. (1957).

[19] Osborn, J. "*Demagnetizing Factors of the General Ellipsoid*". Physical Review Journal. 67: 351-357. doi: 10.1103/PhysRev.67.351. (1945).

[20] Wysin, G. "*Demagnetization Fields*". notes. Retrieved from: https://www.phys.ksu.edu/personal/wysin.

[21] Kumar, N., Prabhakar, A. "*Spin-Wave Dispersion in Striped Magnonic Waveguide*". IEEE Transactions on Magnetics. 49.3: 1024-1028. doi: 10.1109/TMAG.2012.2228173. (2013).

[22] Gurevich, A., Melkov, G. "*Magnetization oscillations and waves*". CRC Press. ISBN: 978-0849394607. (1996).

[23] Demokritov, S., Slavin, A. "*Magnonics – From Fundamentals to Applications*". Springer-Verlag Berlin Heidelberg. Topics in Applied Physics. doi: 10.1007/978-3-642-30247-3. (2013).

[24] Kittel, C. "*Ferromagnetic resonance*". Physical Review Journal. 73:155. doi: 10.1103/PhysRev.73.155. (1948).

[25] Rezende, S. "*Fundamentals of Magnonics*". Cham, Springer International. doi: 10.1007/978-3-030-41317-0. (2020).

[26] Chumak, A., Schultheiss, H. "*Magnonics: spin waves connecting charges, spins and photons*". Journal of Physics D: Applied Physics. 50.300201. doi: 10.1088/1361-6463/aa7715. (2017).

[27] Barman, A., Haldar, A. "*Time-Domain Study of Magnetization Dynamics in Magnetic Thin Films and Micro- and Nanostructures*". Solid State Physics. 65:1-108. doi: 10.1016/B978-0-12-800175-2.00001-7. (2014).

[28] Herring, C., Kittel, C. "*On the Theory of Spin Waves in Ferromagnetic Media*". Physical Review Journals. 88.1435. doi: 10.1103/PhysRev.88.1435.3. (1952).

[29] Soohoo, R. "*General Spin-Wave Dispersion Relations*". Physical Review Journals. 120.6: 1978–1982. doi: 10.1103/PhysRev.120.1978. (1960).

[30] Kalinikos, B., Slavin, A. "*Theory of dipole-exchange spin-wave spectrum for ferromagnetic films with mixed boundary conditions*". Journal of Physics C: Solid State Physics. 19:7013. doi: 10.1088/0022-3719/19/35/014. (1986).

[31] Kwon, J., Mukherjee, S., Deorani, P. et al. "*Characterization of Magnetostatic Surface Spin Waves in Magnetic Thin Films: Evaluation for Microelectronic Applications*". Applied Physics. A, Materials Science & Processing. 111.2: 369-378. doi: 10.1007/s00339-012-7542-x. (2013).

[32] Eshbach, J., Damon, R. "*Surface Magnetostatic Modes and Surface Spin Waves*". Physical Review Journals. 118.5: 1208–1210. doi: 10.1103/PhysRev.118.1208. (1960).

[33] Wessles, P., Vogel,A. "*Direct observation of isolated Damon-Eshbach and backward volume spin-wave packets in ferromagnetic microstripes*". Scientific Reports. 6:22117. doi: 10.1038/srep22117. (2016).

[34] Collet, M., De Milly, X., D'Allivy Kelly, O. et al. "*Generation of Coherent Spin-wave Modes in Yttrium Iron Garnet Microdiscs by Spin–orbit Torque*". Nature Communications. 7.1: 10377. doi: 10.1038/ncomms10377. (2016).

[35] Zagriadski, S., Choi, S. "*Excitation and Reception of Electromagnetic, Magnetostatic and Spin Waves in Ferrite Films*". Journal of Electromagnetic Waves and Applications. 15.12: 1699-1700. doi: 10.1163/156939301X00229. (2001).

[36] Hurben, M., Patton, C. "*Theory of Two Magnon Scattering Microwave Relaxation and Ferromagnetic Resonance Linewidth in Magnetic Thin Films*". Journal of Applied Physics: 83.8: 4344-4365. doi: 10.1063/1.367194. (1998).

[37] Kumar, D., Adeyeye A. O. "*Techniques in micromagnetic simulation and analysis*". Journal of Physics D: Applied Physics. 50: 343001. doi: 10.1088/1361-6463/aa7c04. (2017).

[38] Asadzadeh, M. "*An Introduction to the Finite Element Method for Differential Equations*". Wiley. ISBN: 978-1-119-67164-0. (2020).

[39] Vansteenkiste, A. "*Mumax³ - GPU accelerated micromagnetism*". [Online]. https://mumax.github.io/

[40] Vansteenkiste, A., Leliaert, J., Dvornik, M. et al. "*The design and verification of MuMax³*". AIP Advances. 4: 107133. doi: 10.1063/1.4899186. (2014).

[41] Kumar, D., Dimitriyev, O., Ponraj, S., Barman, A. "*Numerical calculation of spin-wave dispersions in magnetic nanostructures*". Journal of Physics D: Applied Physics. 45.1: 015001. doi: 10.1088/0022-3727/45/1/015001. (2012).

[42] Brächer, T. "*Parallel parametric amplification of spin waves in micro-structures*". PhD Dissertation. Technical University Kaiserslautern. (2015).

[43] Palombo, F., Fioretto, D. "*Brillouin Light Scattering: Applications in Biomedical Sciences*". Chemical Reviews. 119.13:7833-7847. doi: 10.1021/acs.chemrev.9b00019. (2019).

[44] Demokritov, S., Tsymbal, E. "*Light scattering from spin waves in thin films and layered systems*". Journal of Physics: Condensed Matter. 6.36: 7145. doi: 10.1088/0953-8984/6/36/002. (1994).

[45] Ciubutaro, F. "*Spin-wave excitation by nano-sized antennas*". PhD Dissertation. Technical University Kaiserslautern. (2012).

[46] Cottam, M. G., Slavin, A.N. "*Theory for Brillouin Light Scattering from Dipole-Exchange Surface Spin Waves in Ferromagnetic Films*". IEEE Transactions on Magnetics. 27.6: 5489-5491. doi: 10.1109/20.278880. (1991).

[47] Demokritov, S., Demidov, V. "*Micro-Brillouin Light Scattering Spectroscopy of Magnetic Nanostructures*". IEEE Transactions on Magnetics. 44.1: 6-12. doi: 10.1109/TMAG.2007.910227. (2008).

[48] Meyer, T. "*Untersuchungen zur plasmonenunterstützten Signalverstärkung bei der Brillouin-Lichtstreumikroskopie".* Master thesis. Technical University Kaiserslautern. (2012).

[49] Sebastian, T., Schultheiss, K., Obry, B., Hillebrands, B., Schultheiss, H. "*Micro-focused Brillouin light scattering: imaging spin waves at the nanoscale*". Frontiers in Physics. 3:35. doi: 10.3389/fphy.2015.00035. (2015).

[50] Vaughan, J. M. "*The Fabry-Perot Interferometer : History, Theory, Practice and Applications*". CRC Press. ISBN: 0852741383. (1989).

[51] Schultheiß, K. "*Spinwellentransport in zweidimensionalen Mikrostrukturen*". PhD Dissertation. Technical University Kaiserslautern (2013).

[52] Demtröder, W. "*Experimentalphysik 2: Elektrizität und Optik*". Springer Berlin Heidelberg. ISBN : 978-3-642-29943-8. (2013).

[53] Mock, R., Hillebrands, B., Sandercock, R. "*Construction and performance of a Brillouin scattering set-up using a triple-pass tandem Fabry-Pérot interferometer*".

Journal of Physics E: Scientific Instruments. 20.6: 656. doi: 10.1088/0022-3735/20/6/017. (1987).

[54] Shibata, K., Kasahara, K., Nakayama, K. et al. "*Dependence of Non-reciprocity in Spin Wave Excitation on Antenna Configuration*". Journal of Applied Physics. 124.24: 243901. doi: 10.1063/1.5068722. (2018).

[55] Grigoryeva, N., Popov, D., Kalinikos, B. "*Some peculiarities of spin-wave propagation in magnonic waveguides*". European Physical Journal Web of Conferences. 40: 12004. doi: 10.1051/epjconf/20134012004. (2013).

[56] Venkat, G., Kumar, D., Franchin, M. et al. "*Proposal for a Standard Micromagnetic Problem: Spin-Wave Dispersion in a Magnonic Waveguide*". IEEE Transactions on Magnetics. 49.1: 524-529. doi: 10.1109/TMAG.2012.2206820. (2013).

[57] Jamali, M., Kwon, J., Seo, S., Lee, K., Yang, H. "*Spin-Wave Nonreciprocity for Logic Device Applications*". Scientific Reports. 3.1: 3160. doi: 10.1038/srep03160. (2013).

[58] thaTEC:OS program. Retrieved from: https://thatec-innovation.com.

[59] thaTEC Innovation. "*thaTEC: TFPDAS5 manual*". Retrieved from: https://thatec-innovation.com/support/downloads.

[60] thaTEC Innovation. "*Installation notes DAQ hardware for thaTEC:TFPDAS5*". Retrieved from: https://thatec-innovation.com/support/downloads.

[61] Origin(Pro), "Version 2020". OriginLab Corporation, Northampton, MA, USA.

[62] Damon, R., van der Vaart, H. "*Dispersion of spin waves and magnetoelastic waves in YIG*". Proceeding of the IEEE. 53.4: 348-354. doi: 10.1109/PROC.1965.3747. (1965).

Glossary

In the following register the used acronyms are listed alphabetically:

µBLS	Brillouin Light Scattering microscope
BLS	Brillouin Light Scattering
BVMSW	backward volume magnetostatic spin wave
CCD	charged coupled device camera
CPW	coplanar waveguide
FDM	finite difference method
FEM	finite element method
FMR	ferromagnetic resonance
FPI	Fabry-Pérot interferometer
FSR	free spectral range
FVMSW	forward volume magnetostatic spin wave
FWHM	full width half magnitude
GGG	Gadolinium-Gallium-Garnet
LLG	Landau-Lifschitz-Gilbert equation
MSSW	magnetostatic surface spin wave
NA	numerical aperture
PSSW	perpendicular standing wave
SOC	spin-orbit coupling
TFP	Tandem Fabry-Pérot
TR-MOKE	time-resolved magneto-optical Kerr-effect
YIG	Yttrium-Iron-Garnet

Acknowledgements

During my work on this thesis, I met many wonderful people who helped me to put my thesis all together. They were very kind and supportive during the course of this work. Even if I missed mentioning anybody, be sure I am grateful for your assistance along the course of this thesis.

In particular, I would like to express my special thanks to Univ.-Prof. Dr. Andrii Chumak for supervising this thesis. He offered me this opportunity to expand my scientific knowledge in the nanomagnonics research field and gain new interpersonal experiences when sending me to Kaiserslautern, Germany, for the experimental parts of my thesis. I am really glad I took his courses during my master's where I was impressed by his motivation and dedication to his field and his friendly nature.

Another round of applause goes to Dr. Qi Wang who eagerly helped me with the micromagnetic simulations, and Björn Heinz who showed me how to properly use the μBLS microscope and all programs associated with finding my results. Both were very friendly when I joined the group and gladly showed me the right way when I had difficulties concerning my studies.

During the trip to Kaiserslautern, I got to know Dr. Khrystyna Levchenko. She always had an open ear, kind words and a helping hand to encourage me throughout my whole research. Thank you.

I also want to express my gratitude towards all the people in the Nanomagnetism Group at the University of Vienna who are all very friendly and helpful, as well as the AG Magnetismus group in Kaiserslautern for welcoming Dr. Khrystyna Levchenko and me. They warmly included us in social activities and made the stay eventful and full of new interesting moments.

To conclude my list of people I appreciate dearly, I just want to say "Thank you!" to my family and friends without whom I wouldn't have progressed so far. Their loving words always encouraged me to get out of my comfort zone and be the best version of myself.